博士論文

論文題目　　フェノール樹脂の構造と物性に関する散乱実験と

　　　　　　シミュレーションによる研究

　　　　　　(Structure–Property Relationships in Crosslinked Phenolic Resins

　　　　　　Investigated by Scattering Experiments and Computer Simulation)

氏　　名　　首藤　靖幸

Structure–Property Relationships in Crosslinked Phenolic Resins

Investigated by Scattering Experiments and Computer Simulation

Yasuyuki Shudo

A dissertation submitted for the degree of Doctor of Philosophy

Department of Advanced Materials Science

Graduate School of Frontier Sciences

The University of Tokyo

2018

Contents

6

Chapter 1

General Introduction

1.1 Introduction

Phenolic resins are the first commercial synthetic polymers invented by Dr. L. H. Baekeland in 1907, and are widely used thermosetting plastics in a wide range of industries, such as the aerospace, automotive, and semiconductor industries [1–3], due to their high mechanical strength, thermal stability, and insulating and solvent resistance properties that derive from their highly crosslinked structures.
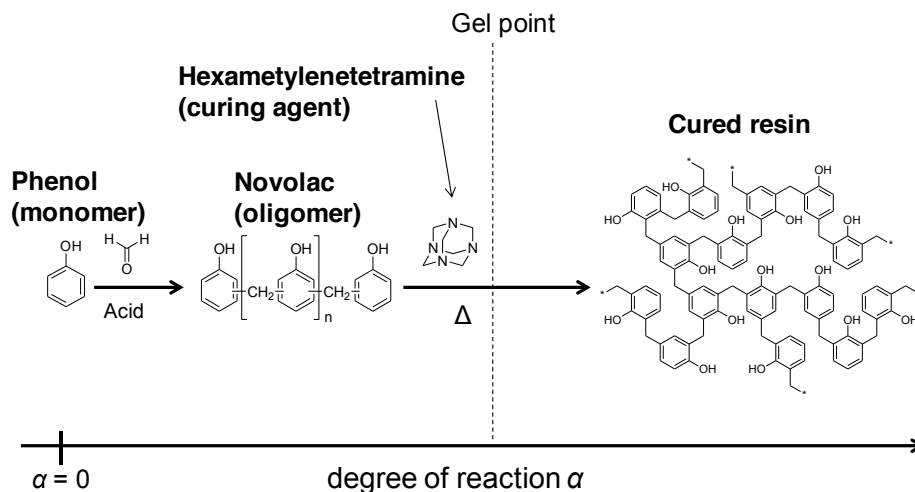
Figure 1.1   Schematic illustrations of the molecular structure of phenolic resins used in typical industrial applications. The degree of reaction α is defined as the fraction of reacted *ortho-* and *para-* positions that are adjacent to the hydroxyl groups of the phenolic rings.

Typical phenolic resins are obtained via condensation polymerization of phenol and formaldehyde. Phenol is considered a three-functional molecule due to the three reactive carbon atoms at two *ortho-* (*o-*) positions and one *para-* (*p-*) position adjacent to hydroxyl groups on a phenolic ring. Therefore, the reaction product of phenol and formaldehyde has a branched structure and forms a highly crosslinked network structure. For general industrial use,

7

crosslinked phenolic resins are prepared by curing a novolac-type phenolic resin oligomer with hexamethylenetetramine (HMTA) as the curing agent (Figure 1.1). Novolac resins can be obtained via polycondensation of phenol and formaldehyde in the presence of an acid catalyst, such as oxalic acid. Novolac resins are further heat treated in the presence of HMTA to obtain cured phenolic resins.

The structure, gelation mechanism, and properties of crosslinked polymer networks have attracted a great deal of attention [4–6]. Generally, the crosslinked structure and inhomogeneity in cured thermosetting resins are recognized as key to controlling the material properties of thermosetting resins [7,8], as well as polymer networks of gels and rubbers [9,10]. Several phenolic resin network models have been proposed, including structural defects [11,12] and microgel structures [13]. Considerable effort has been devoted to fractographic observation using scanning and transmission electron microscopy (SEM and TEM, respectively) [14–16] and X-ray scattering [17–19]. However, to date, there is no strong evidence for inhomogeneous crosslinking in crosslinked phenolic resins. To characterize the chemical structures and understand the phenolic resin reaction behaviors, many investigations have been performed using experimental analyzes, such as liquid- [20–23] and solid-state nuclear magnetic resonance (NMR) spectroscopy [24–26], proton pulse NMR spectroscopy [27], infrared absorption spectroscopy [28] and thermal analyzes [29–33]. Statistical techniques have also been developed and applied to phenolic resins prior to gelation using theoretical [34–37] and kinetic models [38]. However, most of these analyzes have been limited to soluble resins, and crosslinked structures are still poorly understood.

Of the abovementioned methods, X-ray and neutron scatterings have proven to be powerful techniques for elucidating the crosslink inhomogeneity of polymer gel networks [9,10,39]. These techniques reveal a material's nanometer-scale structural details by exploiting the electron and atomic nuclei density fluctuations, which scatter X-rays and neutrons, respectively. The use of both techniques can provide complementary structural information due to the differences in scattering phenomena. In most studies of polymer gels, these scattering methods utilize the swelling features of the gel because swelling enhances local fluctuations in the crosslink density, which results in a large scattering contrast. However, applying this solvent-swelling technique to fully cured thermosetting resins with high-crosslink-density is difficult; therefore, few studies have used their crosslink inhomogeneity using these scattering methods to address crosslink inhomogeneity compared to the number of studies on inhomogeneity using SEM and TEM.

8

Izumi et al. focused on understanding the inhomogeneity of phenolic resins through NMR and scattering analyzes of the oligomerization process at the pre-gelation stage [40,41], the gelation process near the gel point [42,43], and the fully cured resins [44]. The gel point is defined as the point at which an insoluble fraction in a suitable solvent is first detected. In the oligomerization process (well below the gel point), the polymers exhibit a self-similar structure with respect to molecular weight distribution, and no indication of inhomogeneity is observed. Conversely, inhomogeneity appears near the gel point under gelation mechanisms that depend on the amount of crosslinker. (i) When there is a stoichiometrically insufficient amount of the crosslinker, inhomogeneous domains with a loosely crosslinked network appear at the initial stage of gelation, and intradomain reactions in the inhomogeneous domain become dominant with as the degree of crosslinking in the domain increases. (ii) When there is a stoichiometric amount of the crosslinker, inhomogeneous domains with a tightly crosslinked network appear at the initial stage of gelation, and the interdomain reactions between the inhomogeneous domains become dominant as the size of the domain increases. However, crosslink inhomogeneity has not been observed for fully cured phenolic resins prepared with different amounts of the HMTA curing agent.

Molecular simulations are powerful tools for investigating relationships between structures and properties of thermosetting resins because such simulations can obtain structural information that cannot be found by chemical analysis due to the difficulties associated with insolubility and infusibility. Computational approaches to thermosetting resins have been limited to a small molecular model prior to gelation due to the hardware and algorithm limitations that existed until the early 2000s [45,46]. Conversely, since the pioneering work of Yarovsky and Evans [47], many methodologies for constructing models of crosslinked structures and their application to existing materials, particularly epoxy resins, have been reported [48–51]. To construct a crosslinking network, typically involves a pseudo-reaction between unreacted functional groups on molecules in a simulation box. Here a pseudo-reaction is a simplified recombination process that emulates a real chemical reaction, in which a change in electronic structure is not considered with respect to strict *ab initio* calculations due to the computational costs. For molecular modeling of a crosslinked network, coarse-graining of atomic structures [50] and reverse mapping techniques [51] have also been applied using a pseudo-reaction to consider longer dynamics or reduce computational costs.

Izumi et al. previously demonstrated a crosslinking procedure for phenolic resins and

predicted their thermal and mechanical properties using atomistic MD simulation with pseudo-crosslinking [52]. In that study, a crosslinked structure of phenolic resin was constructed from amorphous structures of linear novolac chains consisting of nine phenolic rings and all *ortho–ortho'* methylene linkages by pseudo-crosslinking between unreacted *ortho* and *para* carbons on phenolic rings. In addition, a computational condition was established to characterize thermal and mechanical properties, such as the density, glass transition temperature, Poisson ratio, and tensile modulus. Here, Izumi at al. adopted a DREIDING force field [53] and partial charges estimated from B3LYP/6-31G(d,p) calculations as parameters for the phenolic resins.

These methodologies are effective to understand the structure–property relationships, however, they involve two problems that need to be addressed. The first problem is poor quantitative values for the physical properties of the constructed network structure, i.e., estimated values of the density and tensile modulus were lower than the experimental values. The reason for these discrepancies is assumed to be inadequate DREIDING force field parameters and applied partial charges based on the B3LYP with 6-31G(d) basis sets for the phenolic resins, which resulted in weak nonbonding attractive interactions. The second problem is the possibility of inadequacies in the constructed structure. In their previous study, the molecular configuration of the precursor was not considered; however, whereas many experimental studies have shown molecular weight distribution (MWD) dependencies [3,32,54–56] and the *ortho/para* ratio in the methylene linkage [1,2,31] on the curing behavior and the thermal and mechanical properties of cured resins. Therefore, such diversity in molecular configurations should be considered in order to understand the relationships between structures and material properties in crosslinked resins. Monk *et al*. investigated the mechanical and thermal properties of a crosslinked network from linear novolac resins consisting of nine phenolic rings and all *ortho–para'* and *ortho–ortho'* methylene linkages using a procedure similar to the methods proposed by Izumi et al [57,58]. Monk et al. investigated the dependencies of the density and mechanical properties of network structures on crosslinking reaction conditions with an all-atom OPLS force field [58] and found that these values were strongly influenced by the initial configuration prior to the reaction. However, the final densities of highly crosslinked structures tended to be lower than the experimental values. These results suggest that this crosslinking approach from linear novolac chains is not suitable to obtain a realistic crosslinked structure. To check this assumption, detailed structural analysis and verification of the crosslinked network are required. Verification of a constructed structure is a common but important problem in computer simulation. Most reports concerning crosslinked

10

thermosetting resins have discussed the validity of generated structures from the perspective of material properties, such as density, glass transition temperature, and elastic constants [48]; however, such a comparison is not sufficient to guarantee the accuracy of a crosslinked structure.

1.2 Outline of this Dissertation

Considering the above research background, I intended to investigate the structure–property relationships in crosslinked phenolic resins by using scattering analysis and atomistic MD simulation. First, structural analysis using a scattering method is performed. Here, I focus on the structural inhomogeneity during the curing process of novolac-type phenolic resin and HMTA. Then, MD simulation is performed for the structure–property analysis. Mechanical properties and solvent resistance (solvent penetration into cured resin) were considered in relation to MD simulation. An outline of this dissertation is provided in the following.

In Chapter 2, the theoretical background of scattering analysis, which was indispensable for understanding the structure and dynamics in phenolic resins, is provided. Mathematical expressions for static- and dynamic structure factors are derived using Fourier transformation for the time and space of a time-dependent density function defined from atomistic configurations and scattering length. In the MD simulation we can also obtain the scattering length distribution function from the particle trajectory. Based on these expressions, we conclude that the results of MD simulation and scattering experiment can be mutually understood relative to the scattering function.

In Chapter 3, the curing behavior of a novolac resin cured with HMTA, as well as the influence of an excess amount of HMTA on the curing reaction, is investigated by dynamic light scattering and gel permeation chromatography. A two-roll mixing mill process was applied to control the curing reaction degree. The dependence of the number of mixing times on the weight-average molecular weight (M_w) and hydrodynamic radius (R_h) of novolac resin differed significantly with the amount of HMTA. A larger quantity of HMTA resulted in faster growth and larger R_h and M_w values. The relationship between M_w and R_h for novolac resin in THF indicates two different polymer-growth mechanisms irrespective of the excess amount of HMTA (i.e., power-law and subsequent deviation corresponding to the chain extension and intermolecular reactions between larger molecules, respectively). These results suggest that structural differences governing the mechanical properties of phenolic resins are initiated in the pre-gel stage, followed by noticeable differences in the mechanical properties during the

subsequent curing process.

In Chapter 4, crosslink inhomogeneity of phenolic resins at the initial stage of curing (110–130 °C) is investigated via structural analysis of network structure evolution using ^{1}H-pulse NMR spectroscopy and complementary small- and wide-angle X-ray and neutron scattering. The solvent-swelling technique was applied for all measurements to enhance the local fluctuations in the crosslink density. The network structure of phenolic resins prepared via curing a novolac-type phenolic resin oligomer with HMTA as a curing agent comprises three different structural domains owing to crosslink inhomogeneity; i.e., a high-crosslink-density domain, an interface region between the high- and low-crosslink-density domains, and a low-crosslink-density domain. Intradomain reactions inside the high- and low-crosslink-density domains were dominant during the initial curing process and resulted in no significant change in the spatial location and size of these domains. The percolation of the high-crosslink-density domains occurred at the beginning of the curing process. The high-crosslink-density domains of the phenolic resins cured with a stoichiometrically sufficient amount of the crosslinker exhibited a tightly crosslinked, well-developed network structure from the beginning of the curing process. Conversely, phenolic resins cured with a stoichiometrically insufficient amount of the crosslinker exhibited a loosely crosslinked network structure, whose degree of crosslinking increased as curing proceeded. The minor intradomain reaction at the interface of the high-crosslink-density domains manifested as a significant decrease in the size of the low-crosslink-density domain in the solvent-swollen state.

In Chapter 5, a network structure of crosslinked phenolic resins is constructed and characterized using large-scale atomistic molecular dynamics simulation with a pseudo-reaction algorithm. The atomic configuration of the reaction products was controlled by the reaction probabilities and initial molecular structures. The crosslinked structure obtained from phenols as initial molecules agreed well with experimental results in terms of the branching structure of the phenolic units and the methylene linkages, molecular weight distributions, densities, and scattering functions at various reaction conversions. The calculated structure factor for phenolic resins indicated inhomogeneous crosslinking, which increased as the reaction proceeded after gelation. Voronoi tessellation analysis of the change in the occupation volume of the phenolic units after crosslinking indicated that the initial molecular configuration influenced the resulting crosslinked structure. The experimental molecular weight distribution prior to gelation and the scattering function were well reproduced by a large-scale simulation with 232,000 atoms.

12

In Chapter 6, to understand the structure–mechanical property relationships from an atomistic perspective, an atomistic MD simulation was performed for crosslinked phenolic resins, in order. The tensile modulus was characterized from the linear elastic region of the stress–strain curves under uniaxial tensile deformation. Analysis of the relationships between the moduli and interatomic interactions indicated that *bond* interaction, especially bond orientation for the elongation axis, dominantly affects the tensile modulus in a range of strain $0 \leq \varepsilon \leq 0.05$, while stress-concentration in specific domains and long-range interactions including hydrogen bonding do not.

In Chapter 7, the dynamics of methanol confined in highly crosslinked phenolic resins is investigated using incoherent quasielastic neutron scattering (QENS) and atomistic MD simulations. The QENS analysis for a deuterated phenolic resin and deuterated and non-deuterated methanol indicated the presence of resin dynamics induced by methanol invasion and confined diffusion of the methanol molecules. QENS results suggested that methanol, in the confined resin network space, had a diffusion coefficient of 1.6×10^{-6} cm^2/s, which is one order of magnitude smaller than the bulk value (2.3×10^{-5} cm^2/s). The MD trajectories also showed that methanol diffusion was limited by the resin network, which is consistent with QENS results in terms of the diffusion coefficient and diffusion-like behavior.

References

1. L. H. Baekeland, Method of making insoluble products of phenol and formaldehyde., U.S. Patent 942699, 1907.
2. A. Gardziella, L. A. Pilato, and A. Knop, *Phenolic Resins: Chemistry, Applications, Standardization, Safety and Ecology*, second ed., Springer: Berlin, 2000.
3. *Phenolic Resins: A Century of Progress*, L. Pilato, Ed., Springer: Berlin, 2010.
4. P. J. Flory, *Principles of Polymer Chemistry*, Cornell University Press: Ithaca, 1953.
5. P. -G. de Gennes, *Scaling Concepts in Polymer Physics*, Cornell University Press: Ithaca, 1979.
6. M. Rubinstein, and R. H. Colby, *Polymer Physics*, Oxford University Press: New York, 2003.
7. J. -P. Pascault, H. Sautereau, J. Verdu, and R. J. J. Williams, *Thermosetting Polymers*, Marcel Dekker: New York, 2002.
8. K. Dušek, J. Pleštil, F. Lednický, and S. Luňák, *Polymer*, 1978, **19**, 393–397.

9. M. Shibayama, *Macromol. Chem. Phys.*, 1998, **199**, 1–30.

10. M. Shibayama, *Bull. Chem. Soc. Jpn.*, 2002, **75**, 641–659.

11. J. H. de Boer, *Trans. Faraday Soc.*, 1936, **32**, 10–37.

12. R. Houwink, *Trans. Faraday Soc.*, 1936, **32**, 122–131.

13. S. C. Misra, J. A. Manson, and L. H. Sperling, In *Epoxy Resins Chemistry*, R. S. Bauer, Ed., Am. Chem. Soc.: Washington, D.C., Vol. 114, pp.157, 1979.

14. J. Mijović, and J. A. Koutsky, *Polymer*, 1979, **20**, 1095–1107.

15. R. A. Spurr, E. H. Erath, H. Myers, and D. C. Pease, *Ind. Eng. Chem.*, 1957, **49**, 1839–1842.

16. E. H. Erath, and R. A. Spurr, *J. Polym. Sci.* 1959, **35**, 391–399.

17. R. A. Spurr, E. H. Erath, and H. Myers, *Ind. Eng. Chem.*, 1957, **49**, 1838–1839.

18. E. H. Erath, and R. A. Spurr, *J. Polym. Sci.*, 1958, **28**, 233–234.

19. E. H. Erath, *J. Polym. Sci. Part C*, 1963, **3**, 65–76.

20. S. Sojka, R. Wolfe, E. A. J. Dietz, and B. Dannels, *Macromolecules*, 1979, **12**, 11–14.

21. T. Yamagishi, M. Nomoto, S. Ito, S. Ishida, and Y. Nakamoto, *Polym. Bull.*, 1994, **32**, 501–507.

22. T. Yamagishi, M. Nomoto, S. Yamashita, T. Yamazaki, Y. Nakamoto, and S. Ishida, *Macromol. Chem. Phys.*, 1998, **199**, 423–428.

23. N. Nomoto, T. Yamagishi, and Y. Nakamoto, *J. Network Polym., Jpn.*, 2006, **27**, 210–217.

24. X. Zhang, and D. H. Solomon, *Polymer*, 1998, **39**, 405–412.

25. B. Ottenbourgs, P. Adriaensens, R. Carleer, D. Vanderzande, and J. Gelan, *Polymer*, 1998, **39**, 5293–5300.

26. K. Hirano, and M. Asami, *React. Funct. Polym.*, 2013, **73**, 256–269.

27. M. Nomoto, Y. Fujikawa, T. Komoto, and T. Yamanobe, *J. Mol. Struct.*, 2010, **976**, 419–426.

28. G. Carotenuto, and L. Nicolais, *J. Appl. Polym. Sci.*, 1999, **74**, 2703–2715.

29. E. S. de Medeiros, A. M. Agnelli, K. Joseph, and L. H. de Carvalho, *J. Appl. Polym. Sci.*, 2003, **90**, 1678–1682.

30. J. C. Domínguez, M. V Alonso, M. Oliet, E. Rojo, and F. Rodríguez, *Thermochim. Acta*, 2010, **498**, 39–44.

31. D. Zhou, D. Liu, H. Wang, Y. Lian, and Y. Luo, *Polym. Plast. Technol. Eng.*, 2011, **50**, 983–989.

32. J. Wan, S. Wang, C. Li, D. Zhou, J. Chen, Z. Liu, L. Yu, H. Fan, and B. -G. Li, *Thermochim. Acta*, 2012, **530**, 32–41.

33. S. Markovic, B. Dunjic, A. Zlatanic, and J. Djonlagic, *J. Appl. Polym. Sci.*, 2000, **81**, 1902–1913.

34. W. H. Stockmayer, *J. Chem. Phys.*, 1943, **11**, 45–55.

35. M. F. Drumm, and J. R. Leblanc, In *Step Growth Polymerizations*, D. H. Solomon, Ed., Marcel Decker: New York, p. 157–276, 1972.

36. T. Nakao, F. Tanaka, and S. Kohjiya, *Macromolecules*, 2002, **35**, 5649–5656.

37. T. Nakao, F. Tanaka, and S. Kohjiya, *Macromolecules*, 2006, **39**, 6643–6652.

38. M. I. Aranguren, J. Borrajo, and R. J. J. Williams, *Ind. Eng. Chem. Prod. Res. Dev.*,1984, **23**, 370–374.

39. K. Dušek, *Angew. Makromol. Chem.*, 1996, **240**, 1–15.

40. A. Izumi, T. Takeuchi, T. Nakao, and M. Shibayama, *Polymer*, 2011, **52**, 4355–4361.

41. A. Izumi, T. Nakao, and M. Shibayama, *J. Polym. Sci. Part A Polym. Chem.*, 2011, **49**, 4941–4947.

42. A. Izumi, T. Nakao, and M. Shibayama, *Soft Matter*, 2013, **9**, 4188–4197.

43. A. Izumi, T. Nakao, and M. Shibayama, *Polymer*, 2015, **59**, 226–233.

44. A. Izumi, T. Nakao, H. Iwase, and M. Shibayama, *Soft Matter*, 2012, **8**, 8438–8445.

45. B. L. Schürmann, and L. Vogel, *J. Mater. Sci.*, 1996, **31**, 3435–3440.

46. A. R. Pawloski, J. A. Torres, P. F. Nealey, and J. J. de Pablo, *J. Vac. Sci. Technol. B Microelectron. Nanom. Struct.*, 1999, **17**, 3371–3378.

47. I. Yarovsky, and E. Evans, *Polymer*, 2002, **43**, 963–969.

48. C. Li, and A. Strachan, *J. Polym. Sci. Part B Polym. Phys.*, 2014, **53**, 103–122.

49. H. Liu, M. Li, Z. -Y. Lu, Z. -G. Zhang, C. -C. Sun, and T. Cui, *Macromolecules*, 2011, **44**, 8650–8660.

50. G. Kacar, E. A. J. F. Peters, and G. de With, *Soft Matter*, 2013, **9**, 5785–5793.

51. P. V. Komarov, Y. -T. Chiu, S. -M. Chen, and P. G. Khalatur, *Macromolecules*, 2007, **40**, 8104–8113.

52. A. Izumi, T. Nakao, and M. Shibayama, *Soft Matter*, 2012, **8**, 5283–5292.

53. S. L. Mayo, B. D. Olafson, and W. A. Goddard III, *J. Phys. Chem.*, 1990, **94**, 8897–8909.

54. K. Dušek, and M. Dušková-Smrčková, *Macromol. React. Eng.*, 2012, **6**, 426–445.

55. K. Dušek, M. Dušková-Smrčková, J. Huybrechts, and A. Ďuračková, *Macromolecules*, 2013, **46**, 2767–2784.

56. H. Kishi, T. Naitou, S. Matsuda, A. Murakami, Y. Muraji, and Y. Nakagawa, *J. Polym. Sci. Part B Polym. Phys.*, 2007, **45**, 1425–1434.

57. J. D. Monk, J. B. Haskins, C. W. Bauschlicher, and J. W. Lawson, *Polymer*, 2015, **62**, 39–49.

58. J. D. Monk, E. W. Bucholz, T. Boghozian, S. Deshpande, J. Schieber, C. W. Bauschlicher, and J. W. Lawson, *Macromolecules*, 2015, **48**, 7670–7680.

59. W. L. Jorgensen, and T. B. Nguyen, *J. Comput. Chem.*, 1993, **14**, 195–205.

Chapter 2

Atomistic Configurations, Dynamics and Scattering Function

2.1 Introduction

In this chapter, a basic description of the scattering function is given. In statistical mechanics, the structure and dynamics of matter are understood through a time-dependent pair correlation function and its Fourier transformation, i.e., the structure factor [1–4]. Elastic and inelastic components in the scattering function correspond to the structure and dynamics, respectively.

In scattering experiments, the magnitude of scattering vector $\mathbf{q}$ is defined as follows:

$$q = |\mathbf{q}| = \frac{4\pi}{\lambda} \sin \theta, \tag{2.1}$$

where λ is the wavelength of the incident wave, and θ is a one-half of the scattering angle 2θ. The scattering vector $\mathbf{q}$ is expressed as follows:

$$\mathbf{q} = \mathbf{k}_1 - \mathbf{k}_0, \tag{2.2}$$

where $\mathbf{k}_0$ and $\mathbf{k}_1$ are the wave vectors of incident and scattered waves, respectively. Due to interference caused by interaction between the incident wave and atoms, the observed scattered wave gives a q-dependent intensity profile reflecting atomistic compositions, characteristic length, and periodic structure in the matter.

First, the scattering length density function of particles is defined as follows:

$$\rho(\mathbf{r},t) = \sum_j f_j \cdot \delta\left(\mathbf{r} - \mathbf{r}_j(t)\right), \tag{2.3}$$

where $\mathbf{r}_j(t)$ and f_j are the position at time t and the scattering length of scatterer j, respectively. In X-ray scattering, f is the atomic form factor and shows q-dependency. In nuclear neutron scattering, f is generally represented by b indicating the amplitude of neutron-nuclear interaction. b is independent of q and exhibits a different scattering amplitude depending on the isotopic species. For a time-independent case, scattering amplitude $A(\mathbf{q})$ is defined by Fourier transformation of $\rho(\mathbf{r})$ in space as follows:

$$A(\mathbf{q}) = \int \rho(\mathbf{r})e^{-i\mathbf{q}\cdot\mathbf{r}}d\mathbf{r} = \sum_j f_j e^{-i\mathbf{q}\cdot\mathbf{r}_j}. \tag{2.4}$$

Here, $A(\mathbf{q})$ corresponds to the amplitude of the scattering X-ray or neutron. The scattering intensity in scattering experiments, i.e., the differential cross section, is proportional to $|A(\mathbf{q})|^2$. In the following, starting from these equations, we derive scattering intensity in elastic and inelastic scattering, as well as the relationship with static and dynamic structural factors.

2.2 Static Structure Factor

Elastic scattering using X-rays or neutrons provides statistical information about the electron or nuclei distribution in a material at a given moment, respectively. Here, elastic scattering is a process in which energy and momentum do not change before and after scattering. It is assumed that structure information is not dependent within the observation time of scattering experiments. In small- and wide-angle scattering experiments using X-rays (SAXS and WAXS) or neutrons (SANS and WANS), the q-dependency of the scattered intensity profile $I(\mathbf{q})$ is counted by a detector. As described previously, scattering intensity $I(\mathbf{q})$ is proportional to the square of the absolute value of the scattering amplitude $F(\mathbf{q})$.

$$I(\mathbf{q}) = |A(\mathbf{q})|^2 = \left|\int \rho(\mathbf{r})e^{-i\mathbf{q}\cdot\mathbf{r}}d\mathbf{r}\right|^2$$

$$= \left|\sum_j^N f_j e^{-i\mathbf{q}\cdot\mathbf{r}_j}\right|^2 = \sum_j^N \sum_k^N f_j f_k e^{-i\mathbf{q}\cdot(\mathbf{r}_j-\mathbf{r}_k)} \tag{2.5}$$

$$= \sum_j^N f_j^2 + \sum_j^N \sum_{k\neq j}^N f_j f_k e^{-i\mathbf{q}\cdot(\mathbf{r}_j-\mathbf{r}_k)}.$$

Here, the double sum of indices j and k are divided into two terms for $k = j$ and $k \neq j$. Note that the terms in Equation (2.5) are ensemble averaged. We rewrite this equation of the sum of the particle number (j or k) as the sum of the atomic species (α or β):

$$I(\mathbf{q}) = \sum_\alpha N_\alpha [f_\alpha]^2 + \sum_\alpha N_\alpha f_\alpha \sum_\beta f_\beta \int_V n_{\alpha\beta}(\mathbf{r})e^{-i\mathbf{q}\cdot\mathbf{r}}d\mathbf{r}, \tag{2.6}$$

where $n_{\alpha\beta}(\mathbf{r})$ is the number density of the particle of atomic species β at position $\mathbf{r}$ as seen from the particle of atomic species α. Therefore, in the limit of r at infinity, $n_{\alpha\beta}(\mathbf{r})$ converges the particle number density of β (N_β/V). For convenience, the pair distribution function $g_{\alpha\beta}(\mathbf{r})$ is defined as $n_{\alpha\beta}(\mathbf{r})$ divided by N_β/V. By this substitution, Equation (2.6) is given as follows:

$$I(\mathbf{q}) = \sum_\alpha N_\alpha (f_\alpha)^2 + \frac{1}{V} \sum_\alpha N_\alpha f_\alpha \sum_\beta N_\beta f_\beta \int_V [g_{\alpha\beta}(\mathbf{r}) - 1] e^{-i\mathbf{q}\cdot\mathbf{r}} d\mathbf{r}$$

$$+ \frac{1}{V} \sum_\alpha N_\alpha f_\alpha \sum_\beta N_\beta f_\beta \, \delta(\mathbf{q}) \tag{2.7}$$

$$= N \sum_\alpha c_\alpha (f_\alpha)^2 + \rho N \sum_\alpha \sum_\beta c_\alpha c_\beta f_\alpha f_\beta \int [g_{\alpha\beta}(\mathbf{r}) - 1] e^{-i\mathbf{q}\cdot\mathbf{r}} d\mathbf{r},$$

where c_α (c_β) represents the concentration of atomic species α (β). Here we define the partial structure factor $S_{\alpha\beta}(\mathbf{q})$ proposed by Faber and Ziman [5] as follows:

$$S_{\alpha\beta}(\mathbf{q}) = 1 + \rho \int [g_{\alpha\beta}(\mathbf{r}) - 1] e^{-i\mathbf{q}\cdot\mathbf{r}} d\mathbf{r}. \tag{2.8}$$

Then, Equation (2.7) is written as follows:

$$I(\mathbf{q}) = N \sum_\alpha c_\alpha [f_\alpha(\mathbf{q})]^2 + N \sum_\alpha \sum_\beta c_\alpha c_\beta f_\alpha f_\beta [S_{\alpha\beta}(\mathbf{q}) - 1]. \tag{2.9}$$

If a structure has no anisotropy, Equation (2.8) can be written as follows:

$$S_{\alpha\beta}(q) = 1 + \rho \int_0^\infty [g_{\alpha\beta}(\mathbf{r}) - 1] \frac{\sin qr}{qr} 4\pi r^2 dr. \tag{2.10}$$

Finally, the total structure factor is given by weighting the X-ray atomic form factor $f(q)$ as follows:

$$S(q) = \frac{\sum_\alpha \sum_\beta c_\alpha c_\alpha f_\alpha(q) f_\beta(q) S_{\alpha\beta}(q)}{\sum_\alpha \sum_\beta c_\alpha c_\alpha f_\alpha(q) f_\beta(q)}. \tag{2.11}$$

As a result, the scattering intensity is reduced to the following equation:

$$I(q) = N \sum_\alpha c_\alpha (f_\alpha)^2 + N[S(q) - 1]. \tag{2.12}$$

Equation (2.12) shows the relations between experimentally obtained scattering intensity and the structure factor.

2.3 Dynamic Structure Factor

In neutron scattering by a cold neutron, energy transfer may occur from the sample to the neutron because the energy in the cold neutron is of the same order as the kinetic energy of atoms and molecules. Conversely, the scattering intensity profiles provide information about the molecular dynamics in the scatterer, such as diffusion and fast relaxation. He, we focus on the scattering process by a neutron involving energy transfer, i.e., inelastic scattering.

The momentum of neutron $\mathbf{p}$ is described as $\mathbf{p} = \hbar\mathbf{k}$, where $\hbar = (\hbar\,/\,2\pi)$ is Dirac constant, and $\mathbf{k}$ is the wave vector of the neutron. The magnitude of momentum $p = \hbar k$ is related to the energy as follows:

$$E = \frac{p^2}{2m} = \frac{\hbar^2 k^2}{2m} = \hbar\omega, \tag{2.13}$$

where ω is the angular frequency. Now, we consider the scattering of the neutron by the sample. The momentum transfer from the sample to the neutron on scattering is given as follows:

$$\Delta\mathbf{p} = \hbar\mathbf{k}_1 - \hbar\mathbf{k}_0 = \hbar(\mathbf{k}_1 - \mathbf{k}_0) = \hbar\mathbf{q}, \tag{2.14}$$

where $\mathbf{k}_0$ and $\mathbf{k}_1$ are the momentum of incident and scattered neutrons, respectively. Similarly, the energy transfer on scattering is described as follows:

$$\Delta E = E_1 - E_0 = \frac{\hbar^2}{2m}(k_1^2 - k_0^2) = \hbar(\omega_1 - \omega_0) = \hbar\omega, \tag{2.15}$$

where $\omega = \omega_1 - \omega_0$ indicates change in the angular frequency. In inelastic and quasielastic neutron scattering, the scattering intensity is recorded as a function of both the scattering angle Ω and the magnitude of energy transfer $\hbar\omega$.

The double differential cross section in neutron scattering is related to the structure and the dynamics of the nuclei.

$$\frac{\partial^2\sigma}{\partial\Omega\partial\omega} = \frac{k_1}{k_0}\frac{1}{2\pi}\int \left\langle \left(\sum_j b_j e^{-i\mathbf{q}\cdot\mathbf{r}_j(t)}\right)\left(\sum_k b_k e^{-i\mathbf{q}\cdot\mathbf{r}_k(0)}\right)^{\dagger} \right\rangle e^{i\omega t}\mathrm{d}t. \tag{2.16}$$

Here, we define the intermediate scattering function $F(\mathbf{q}, t)$ as follows:

$$F(\mathbf{q}, t) = \frac{1}{N}\sum_j\sum_k \left\langle e^{-i\mathbf{q}\cdot\mathbf{r}_j(t)} \cdot e^{i\mathbf{q}\cdot\mathbf{r}_k(0)} \right\rangle. \tag{2.17}$$

Now, we introduce the van Hove function to indicate a time-dependent pair correlation function defined as follows:

$$G(\mathbf{r}, t) = \frac{1}{N}\sum_j\sum_k \left\langle \delta\left(\mathbf{r} - \left(\mathbf{r}_j(t) - \mathbf{r}_k(0)\right)\right) \right\rangle$$

$$= \frac{1}{N}\int \left\langle \rho(\mathbf{r} + \mathbf{r}', t)\rho(\mathbf{r}, 0) \right\rangle \mathrm{d}\mathbf{r}'. \tag{2.18}$$

$G(\mathbf{r}, t)$ is also represented by the inverse Fourier transform of $F(\mathbf{q}, t)$ in space as follows:

$$G(\mathbf{r}, t) = \frac{1}{N}\sum_j\sum_k \frac{1}{(2\pi)^3}\int \left\langle e^{-i\mathbf{q}\cdot\mathbf{r}_j(t)} \cdot e^{i\mathbf{q}\cdot\mathbf{r}_k(0)} \right\rangle e^{i\mathbf{q}\cdot\mathbf{r}}\mathrm{d}\mathbf{q}. \tag{2.19}$$

Equation (2.17) is simply represented as follows:

$$F(\mathbf{q}, t) = \int G(\mathbf{r}, t) e^{-i\mathbf{q} \cdot \mathbf{r}} d\mathbf{r}. \tag{2.20}$$

The double differential cross section can be also written as follows:

$$
\begin{aligned}
\frac{\partial^2 \sigma}{\partial \Omega \partial \omega} &= \frac{k_1}{k_0} \frac{1}{2\pi} \sum_j \sum_k \langle b_j b_k \rangle \int \langle e^{-i\mathbf{q} \cdot \mathbf{r}_j(t)} \cdot e^{-i\mathbf{q} \cdot \mathbf{r}_k(0)} \rangle e^{i\omega t} dt \\
&= \frac{k_1}{k_0} \frac{N}{2\pi} \sum_j \sum_k \langle b_j b_k \rangle \int \langle e^{-i\mathbf{q} \cdot \mathbf{r}_j(t)} \cdot e^{-i\mathbf{q} \cdot \mathbf{r}_k(0)} \rangle e^{i\omega t} dt \\
&= \frac{k_1}{k_0} \frac{N}{2\pi} b^2 \int F(\mathbf{q}, t) e^{i\omega t} dt \\
&= \frac{k_1}{k_0} \frac{N}{2\pi} b^2 \iint G(\mathbf{r}, t) e^{-i\mathbf{q} \cdot \mathbf{r}} e^{i\omega t} d\mathbf{r} dt \\
&= \frac{k_1}{k_0} N b^2 \frac{1}{2\pi} S(\mathbf{q}, \omega).
\end{aligned}
\tag{2.21}
$$

$S(\mathbf{q}, \omega)$ is the dynamic structure factor defined as the Fourier transform of $G(\mathbf{r},t)$ in space and time as follows:

$$S(\mathbf{q}, \omega) = \frac{1}{2\pi} \int F(\mathbf{q}, t) e^{-i\omega t} dt = \frac{1}{2\pi} \iint G(\mathbf{r}, t) e^{-i\mathbf{q} \cdot \mathbf{r}} e^{i\omega t} d\mathbf{r} dt. \tag{2.22}$$

Here, the absolute square of scattering amplitude in Equation (2.16) is expanded as follows.

$$
\begin{aligned}
\left\langle \left(\sum_j b_j e^{-i\mathbf{q} \cdot \mathbf{r}_j(t)} \right) \left(\sum_k b_k e^{-i\mathbf{q} \cdot \mathbf{r}_k(0)} \right)^\dagger \right\rangle &= \sum_j \sum_k \langle b_j e^{-i\mathbf{q} \cdot \mathbf{r}_j(t)} \cdot b_k e^{i\mathbf{q} \cdot \mathbf{r}_k(0)} \rangle \\
&= \sum_j \langle b_j e^{-i\mathbf{q} \cdot \mathbf{r}_j(t)} \cdot b_j e^{i\mathbf{q} \cdot \mathbf{r}_j(0)} \rangle + \sum_j \sum_{k \neq j} \langle b_j e^{-i\mathbf{q} \cdot \mathbf{r}_j(t)} \cdot b_k e^{i\mathbf{q} \cdot \mathbf{r}_k(0)} \rangle \\
&= \sum_j \left(\langle b_j^2 \rangle - \langle b_j \rangle^2 \right) \langle e^{-i\mathbf{q} \cdot \mathbf{r}_j(t)} \cdot e^{i\mathbf{q} \cdot \mathbf{r}_j(0)} \rangle + \sum_{j,k} \left(\langle b_j \rangle \langle b_k \rangle \right) \langle e^{-i\mathbf{q} \cdot \mathbf{r}_j(t)} \cdot e^{i\mathbf{q} \cdot \mathbf{r}_k(0)} \rangle \\
&= (\langle b^2 \rangle - \langle b \rangle^2) \sum_j \langle e^{-i\mathbf{q} \cdot \mathbf{r}_j(t)} \cdot e^{i\mathbf{q} \cdot \mathbf{r}_j(0)} \rangle + \langle b \rangle^2 \sum_{j,k} \langle e^{-i\mathbf{q} \cdot \mathbf{r}_j(t)} \cdot e^{i\mathbf{q} \cdot \mathbf{r}_k(0)} \rangle \\
&= \frac{\sigma_{\text{inc}}}{4\pi} \sum_j \langle e^{-i\mathbf{q} \cdot \mathbf{r}_j(t)} \cdot e^{i\mathbf{q} \cdot \mathbf{r}_j(0)} \rangle + \frac{\sigma_{\text{coh}}}{4\pi} \sum_{j,k} \langle e^{-i\mathbf{q} \cdot \mathbf{r}_j(t)} \cdot e^{i\mathbf{q} \cdot \mathbf{r}_k(0)} \rangle.
\end{aligned}
\tag{2.23}
$$

Here, σ_{inc} and σ_{coh} are the incoherent and coherent cross sections, respectively, given as follows:

$$
\begin{aligned}
\sigma_{\text{inc}} &= 4\pi(\langle b^2 \rangle - \langle b \rangle^2), \\
\sigma_{\text{coh}} &= 4\pi \langle b^2 \rangle.
\end{aligned}
\tag{2.24}
$$

Using Equation (2.23), $G(\mathbf{r},t)$ can be represented as follows:

$$G(\mathbf{r}, t) = G_s(\mathbf{r}, t) + G_d(\mathbf{r}, t),$$

$$G_{\mathrm{s}}(\mathbf{r}, t) = \frac{\sigma_{\mathrm{inc}}}{4\pi N} \frac{1}{(2\pi)^3} \sum_j \int \langle e^{-i\mathbf{q} \cdot \mathbf{r}_j(t)} \cdot e^{i\mathbf{q} \cdot \mathbf{r}_j(0)} \rangle e^{i\mathbf{q} \cdot \mathbf{r}} \mathrm{d}\mathbf{q},$$

$$G_{\mathrm{d}}(\mathbf{r}, t) = \frac{\sigma_{\mathrm{coh}}}{4\pi N} \frac{1}{(2\pi)^3} \sum_{j,k} \int \langle e^{-i\mathbf{q} \cdot \mathbf{r}_j(t)} \cdot e^{i\mathbf{q} \cdot \mathbf{r}_j(0)} \rangle e^{i\mathbf{q} \cdot \mathbf{r}} \mathrm{d}\mathbf{q},$$

(2.25)

where subscripts "s" and "d" indicate "self" and "distinct," respectively. Similarly, the double differential cross section in Equation (2.21) is represented as follows:

$$\frac{\partial^2 \sigma}{\partial \Omega \partial \omega} = \frac{k_1}{k_0} \left[\frac{\sigma_{\mathrm{inc}}}{4\pi} S_{\mathrm{inc}}(\mathbf{q}, \omega) + \frac{\sigma_{\mathrm{coh}}}{4\pi} S_{\mathrm{coh}}(\mathbf{q}, \omega) \right],$$

$$S_{\mathrm{inc}}(\mathbf{q}, \omega) = \frac{1}{2\pi} \int \sum_j \langle e^{-i\mathbf{q} \cdot \mathbf{r}_j(t)} e^{i\mathbf{q} \cdot \mathbf{r}_j(0)} \rangle e^{i\omega t} \mathrm{d}t,$$

$$S_{\mathrm{coh}}(\mathbf{q}, \omega) = \frac{1}{2\pi} \int \sum_{j,k} \langle e^{-i\mathbf{q} \cdot \mathbf{r}_j(t)} e^{i\mathbf{q} \cdot \mathbf{r}_k(0)} \rangle e^{i\omega t} \mathrm{d}t,$$

(2.26)

where subscripts "inc" and "coh" indicate "incoherent" and "coherent," respectively. The incoherent and coherent dynamic structure factors clearly indicate the self- and collective-dynamics of the scatterer, respectively. Neutron spin echo (NSE) spectroscopy, quasielastic neutron scattering (QENS), and inelastic neutron scattering (INS) are commonly used as experimental methods to obtain the coherent and incoherent parts of the dynamic structure factor. If momentum transfer does not occur ($\omega = 0$), the dynamic structure factor reduces to the static structure factor as described in Equations (2.5–12), which is observed in the SANS/WANS experiments discussed in Chapter 4. Among these methods, incoherent QENS is suitable for detecting the self-motion of polymeric system efficiently by using H/D contrast because the incoherent scattering cross section of ^{1}H is larger than the coherent scattering cross section of ^{1}H and the incoherent scattering cross section of ^{2}H (deuterium).

To prepare for the discussion in Chapter 7, a simple translational diffusion is considered as a simple model of dynamics. The Fickian diffusion equation with spherical symmetry is described as follows:

$$\frac{\partial c(\mathbf{r}, t)}{\partial t} = D\nabla^2 c(\mathbf{r}, t),$$

(2.27)

where D is the diffusion coefficient. $c(\mathbf{r}, t)$ represents the density at position $\mathbf{r}$ and time t. The self-correlation term in van Hove function $G_s(\mathbf{r}, t)$ is nothing but the density; therefore, Equation (2.27) can be written as follows:

$$\frac{\partial G_s(\mathbf{r}, t)}{\partial t} = D\nabla^2 G_s(\mathbf{r}, t). \tag{2.28}$$

By solving this equation under the assumption that the diffusion progresses isotropically, we obtain the following.

$$G_s(\mathbf{r}, t) = \frac{1}{(4\pi D|t|)^{3/2}} \exp\left(-\frac{r^2}{4D|t|}\right) \tag{2.29}$$

Fourier transform of $G_s(\mathbf{r}, t)$ in space gives the following.

$$F_s(\mathbf{q}, t) = \int G_s(\mathbf{r}, t) d\mathbf{r} = e^{-Dq^2|t|} = e^{-|t|/\tau} \tag{2.30}$$

Equation (2.30) means that the self-part of the intermediate scattering function in simple diffusion is represented by a single exponential function with relaxation time $\tau\ (= 1/Dq^2)$. By Fourier transformation in time, the self-part of the dynamic scattering function is obtained as follows:

$$S_{\text{inc}}(\mathbf{q}, \omega) = \int_{-\infty}^{\infty} F_s(\mathbf{q}, t) e^{-i\omega t} dt = \frac{1}{\pi} \frac{Dq^2}{(Dq^2)^2 + \omega^2}. \tag{2.31}$$

This corresponds to a simple Lorentzian function:

$$L(\Gamma, \omega) = \frac{1}{\pi} \frac{\Gamma}{\Gamma^2 + \omega^2} \tag{2.32}$$

where $\Gamma\ (= Dq^2)$ represents a half-width at half-maximum (HWHM). The molecular motion such as diffusion can be investigated by analyzing the q-dependence of Γ in the incoherent scattering profiles.

2.4 Conclusions

In this chapter, static and dynamic structure factors were derived by Fourier transformation of a probability density function in time and space, which is essential to understand the structure and dynamics of matter in elastic and inelastic scattering experiments. These derivations also indicate that atomistic trajectories including coordinates and momentum obtained from an atomistic MD simulation, can reproduce static and dynamic structure factors. In conclusion, the results of MD simulation can be compared and verified via scattering profiles.

Note that atomistic trajectories obtained from molecular simulation can generate $S(q)$ or $S(q,\omega)$ via Fourier transformation of the density function for space and time. On the other hand, atomistic coordinates cannot be completely determined from experimental scattering

functions due to the lack of boundary conditions in the inverse problem of determining individual atomic arrangements and atomic species from structure factor functions. Reverse Monte Carlo methods can generate the atomistic coordinates from the structure factor [6]; however, the obtained spatial arrangement only represents a single candidate solution. To solve the inverse problem of structure determination, other structural information could be used as a constraint condition, such as local structures obtained by a spectroscopic technique, such as near-edge X-ray absorption fine structure (NEXAFS), and partial structure factors using a contrast variation method that employs neutron scattering with H/D contrast [7] or anomalous X-ray scattering (resonant scattering) [8].

References

1. R. J. Roe, *Methods of X-ray and neutron scattering in polymer science*, Oxford University Press, New York, 2000.

2. M. Bée, *Quasielastic Neutron Scattering: Principles and Applications in Solid State Chemistry, Biology and Materials Science*, Adam Hilger: Bristol and Philadelphia, 1988.

3. G. R. Strobl, *The Physics of Polymers*, third ed., Springer-Verlag: Berlin, 2007.

4. F. Tanaka, *Polymer Physics: Applications to Molecular Association and Thermoreversible Gelation*, Cambridge University Press: New York, 2011.

5. T. E. Faber, and J. M. Ziman, *Philos. Mag.*, 1965, **11**, 153–173.

6. R. L. McGreevy, and L. Pusztai, *Mol. Simul.*, 1988, **1**, 359–367.

7. S. Miyazaki, H. Endo, T. Karino, K. Haraguchi, and M. Shibayama, *Macromolecules*, 2007, **40**, 4287–4295.

8. Y. Shinohara, H. Seike, H. Kishimoto, Y. Tamenori, and Y. Amemiya, *Polymer*, 2016, **105**, 368–377.

Chapter 3

Dynamic Light Scattering Study of the Curing Mechanisms of Phenolic Resins

3.1 Introduction

The excellent properties of cured phenolic resins are derived from their three-dimensional, crosslinked network structures, as well as their high crosslink densities. To obtain highly cured phenolic resins, an excess amount of HMTA (greater than the stoichiometric ratio) is frequently used for industrial curing of novolac resin [1,2]. Experimentally, the preparation of phenolic resins with an excess amount of HMTA results in an improvement in the mechanical strength and modulus of the cured resins. However, the influence of the excess amounts of HMTA on the resulting crosslinked structure has not been well studied due to challenges associated with analyzing the structures of insoluble and infusible cured phenolic resins.

In this chapter, the evolution of novolac clusters was studied during the curing process in the pre-gel regime and the influence of an excess amount of HMTA on this evolution using dynamic light scattering (DLS) and gel permeation chromatography (GPC) in terms of the hydrodynamic radius (R_h) and the weight-average molecular weight (M_w). An open two-roll mixing mill process was applied to control α by changing the number of roll-mixing times (N). The mechanical properties of the obtained phenolic resins that were prepared using varying amounts of HMTA after roll mixing and compression molding were also evaluated using a flexural test.

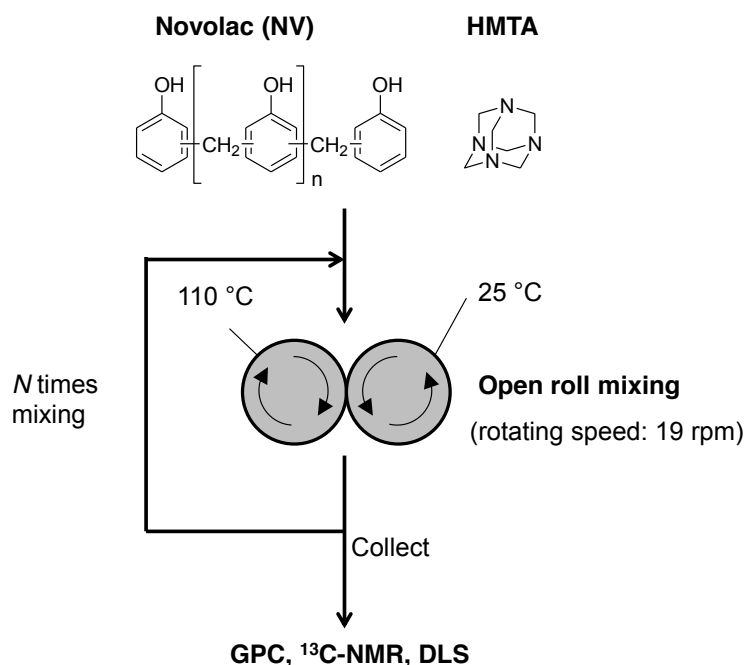## 3.2 Experimental

3.2.1   Materials

A novolac-type phenolic resin oligomer PR-53195 (**NV**) was provided by Sumitomo Bakelite Co., Ltd. (Tokyo, Japan), and HMTA was purchased from Chang Chung Petrochemical Co., Ltd (Taipei, Taiwan). A random-type phenolic resin was synthesized using phenol, 37 wt% aqueous formaldehyde, and oxalic acid. The number-average molecular weight (M_n) and M_w

were determined to be 0.98×10^3 g·mol^{-1} and 2.37×10^3, respectively, using gel permeation chromatography (GPC). THF was purchased from Wako Pure Chemical Industries, Ltd. Methanol-d_4 (99.9 at% D, containing 0.05 vol% tetramethylsilane) was purchased from C/D/N Isotopes, Inc. All of the materials were used as received without further purification. THF was used as the solvent for the GPC and DLS analyses because it is a good solvent for novolac resins.

3.2.2 Sample Preparation

The sample preparation procedures are shown in Figure 3.1. **NVHX-16.7** and **NVHX-15** were 1700/300 and 1700/225 (g/g) mixtures of **NV** and HMTA, respectively, and prepared by mechanical blending using a grinder-type mixer. The initial molar ratios of the methylene groups in the **NV** and HMTA and the phenolic rings in the **NV** ($[CH_2]_0/[PhOH]_0$) were 1.67 and 1.50, respectively, for **NVHX-16.7** and **NVHX-15**, respectively. These ratios were estimated using the M_n of **NV**. $[CH_2]_0/[PhOH]_0 = 1.50$ corresponds to the stoichiometric ratio for **NV**. However, the **NVHX-16.7** system contained an excess amount of HMTA. It is important to note that the ratio is within the range that is typically employed in industry [1,2].

Figure 3.1   Sample preparation using by open two-roll mixing process. Aliquots of the reaction mixture were collected for GPC, ^{13}C-NMR, and DLS analyses.

As shown in Figure 3.1, a two-roll mixing mill process was performed using an open 12-inch two-roll mixing mill (Toyo Sekkei Co., Ltd, Japan), which consists of two horizontally placed hollow metal rolls rotating toward each other at the same speed (i.e., 19 rpm). The surface temperatures of the two rolls were set to 110 and 25 °C and controlled within a range of ±1 °C during the mixing process. The mixing of **NV** and HMTA occurred in the melted state during the initial mixing stage because the melting temperature of **NV** was 80–90 °C. The two-roll mixing mill process was performed above the gel point until a THF-insoluble material was obtained, and the time interval was 40 sec for the subsequent mixing procedure. During the two-roll mixing, small amounts of the reaction mixture were collected at different times and cooled to room temperature. The samples obtained below the gel point were used for GPC, ^{13}C NMR, and DLS analyses. The number of mixing times (N) for each sample is listed in Table 1. THF-insoluble portions were obtained at $N = 130$ for **NVHX-16.7** and $N = 135$ for **NVHX-15**.

3.2.3 GPC Analyses

GPC experiments were performed using a Tosoh HLC-8320 system (Tosoh, Tokyo, Japan) equipped with four poly(styrene-*co*-divinylbenzene) gel columns (TSKgel SuperHZ-H, SuperHZ-H, SuperH2000, SuperH2000) and a Viscotek TDA302 system (Viscotek Corporation, USA) equipped with a differential refractive index (RI) detector. The polymer concentration in each injection solution was 0.20 wt%, and the solutions were filtered through a 0.20 μm filter (Tosoh H-13-2) prior to injection. THF at 40 °C was used as the eluent. The results obtained with the RI detector were used along with a calibration curve generated using 14 polystyrene standards to calculate the M_w and M_n values for the polymers. The peak molecular weights of the polystyrene standards were 8.42×10^6, 5.48×10^6, 2.11×10^6, 7.06×10^5, 4.27×10^5, 1.90×10^5, 9.64×10^4, 3.79×10^4, 1.81×10^4, 1.02×10^4, 5.97×10^3, 2.42×10^3, 1.01×10^3, and 5.00×10^2 g mol^{-1}. The GPC results are listed in Table 3.1.

3.2.4 ^{13}C NMR Analyses

A JEOL JNM-ECA500 FT-NMR spectrometer (JEOL Ltd., Japan) operating at 500 MHz was used for ^{13}C NMR analyses. The ^{13}C NMR spectra were recorded using 10,000 scans at room temperature. A 10 wt% solution in methanol-d_4 was used for each measurement after filtering

through a 0.20 μm filter (Tosoh H-13-2), which was also used for the GPC measurements. The α value was calculated according to a previous reported protocol [3,4] using the signal intensities of the aromatic carbons observed at 110–160 ppm, and the results are listed in Table 1.

3.2.5 DLS

DLS experiments were performed on a static/dynamic compact goniometer DLS/SLS-5000 (ALV, Langen, Germany). A He–Ne laser with a 22 mW emitting polarized light at a wavelength of 632.8 nm was used as the incident beam. DLS measurements were conducted at 25 °C with an acquisition time of 30 s. The scattering angle (θ) was 90°. The polymer concentration was 1.0 vol%, and each polymer solution was filtered through a 0.20 μm filter (Tosoh H-13-2), which was used for GPC analyses. The DLS results were used to calculate the time–intensity correlation function ($g^{(2)}(\tau)$) as a function of the decay time (τ) as follows:

$$g^{(2)}(\tau) = \frac{\langle I(\tau)I(0)\rangle}{\langle I(0)\rangle^2} = 1 + \left|g^{(1)}(\tau)\right|^2, \tag{3.1}$$

where $I(\tau)$ denotes the scattering intensity at time τ, $<...>$ indicates the time average, and $g^{(1)}(\tau)$ represents the scattering electric field–time correlation function, which is described using a Laplace transform of the characteristic decay time distribution function ($G(\Gamma)$) and is given by:

$$g^{(1)}(\tau) = \int_0^\infty G(\Gamma)e^{-\Gamma\tau}d\Gamma, \tag{3.2}$$

where Γ is the characteristic decay rate [5]. In the present study, the constrained regularization program CONTIN [6], which is supplied with the correlator, was used to calculate $G(\Gamma)$ from $g^{(2)}(\tau)$. For dilute polymer solutions, Γ is related to the translational diffusion coefficient (D), which is given as follows:

$$\Gamma = Dq^2, \tag{3.3}$$

where q denotes the magnitude of the scattering vector (**q**), which is defined by:

$$q = |\mathbf{q}| = \frac{4\pi n_0}{\lambda}\sin\frac{\theta}{2}, \tag{3.4}$$

where n_0 and λ denote the refractive index of the solvent and the wavelength of light in vacuum, respectively. Then, R_h of the polymer in the dilute solution is obtained using the Stokes–Einstein equation:

$$R_h = \frac{k_{\mathrm{B}}T}{6\pi\eta D},$$ (3.5)

where k_{B}, T, and η are the Boltzmann constant, the absolute temperature, and the solvent viscosity, respectively. The η and n_0 values for THF at 25 °C are 0.456 mPa s [7] and 1.404 [8], respectively.

3.2.6   Flexural Test

The mechanical properties of the phenolic resin were evaluated using an autograph AG-X 5kN (Shimadzu Corp., Japan). The flexural tests were performed according to the 178:2010 ISO standard. The **NVHX-16.7** and **NVHX-15** specimens for the flexural test were prepared by compression molding using a compression molding machine (Shinto Metal Industries Corp, Japan). Granulated **NVHX-16.7** and **NVHX-15** were placed in a molding die and molded at 175 °C for 3 min under a pressure of 10 MPa, followed by curing at 180 °C for 6 h under atmospheric pressure. The approximate size of the test pieces was 10 mm × 4 mm × 80 mm. The **NVHX-16.7** and **NVHX-15** samples used for molding were obtained after two-roll mixing at $N = 125$ and $N = 130$, respectively. The three-point flexural test was performed three times to determine the flexural modulus and strength of each sample at 25 °C and atmospheric pressure. The obtained average and standard deviation are provided in Table 2.

3.3 Results and Discussion

3.3.1   Molecular Weight

Figure 3.2 shows the GPC chromatograms for **NVHX-16.7** after various mixing times, and the curves are normalized with respect to the total chromatogram area. The peaks located at retention times of 21.5, 20.3, 19.7, and 19.2 min correspond to the unreacted phenol monomer, dimer, trimer, and tetramer, respectively. The intensities of these signals did not change significantly during the roll-mixing process. However, as the reaction proceeded, the intensities of the signals corresponding to 5,000–10,000 and 1,000–5,000 g mol^{-1} increased at 15–16 min and decreased at 16–17 min, respectively. This behavior was also observed for **NVHX-15**. These results indicate that intermolecular reactions between larger molecules with molecular weights of 1,000 to 5,000 g mol^{-1} become dominant as the gel point is reached, and only a few low-molecular-weight components, such as the monomer, dimer, and trimer, participated in

29

the reactions. This behavior is in agreement with the gelation mechanism previously proposed for phenolic resins by Yamagishi et al. based on Monte Carlo simulations of phenol-formaldehyde polycondensation reactions [9,10]. It is important to note that the mechanism of the curing reaction of **NV** with HMTA as the curing agent is different from that in the phenol-formaldehyde polycondensation reaction. However, this agreement indicates the general gelation behavior of phenolic resins. For further confirmation of this assumption, MD simulations, including simulations of the crosslinking reaction [11,12], are considered to be important. Statistical approaches that analyze the gelation kinetics, such as the cascade theory [13,14], are also promising tools because they can be used to estimate molecular weight distributions with high precision.
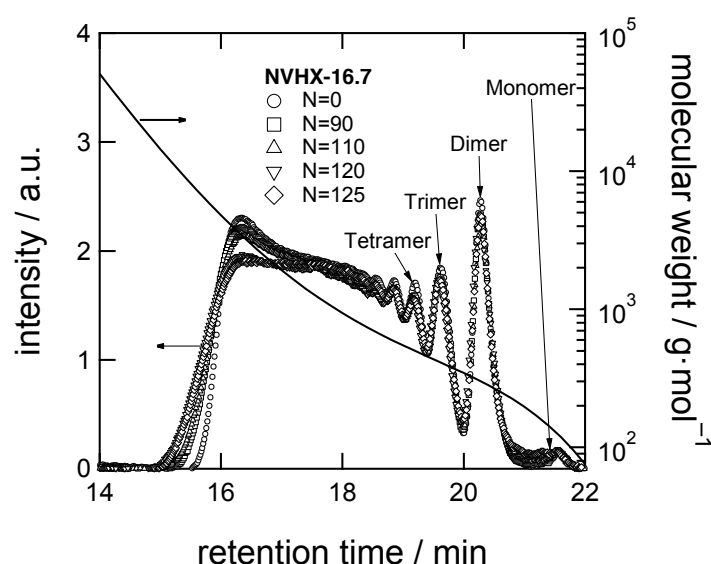

Figure 3.2　Gel permeation chromatograms of **NVHX-16.7** measured in THF at 40 °C. The solid line represents the calibration curve based on polystyrene standards.

Table 3.1 lists the α, M_w, and M_n values for **NVHX-16.7** and **NVHX-15** after the two-roll mixing mill process. Gelation occurred at $N = 130$ and 135 for **NVHX-16.7** and **NVHX-15**, respectively, and was defined as the moment when the THF-insoluble material was obtained. Figure 3.3 shows the M_w values for **NVHX-16.7** and **NVHX-15** as a function of N. Initially, the M_w values gradually increased with N and then sharply increased. In addition, the M_w values for **NVHX-16.7** were larger than those of **NVHX-15**. These results indicate that in the chemical reaction between the **NV** and HMTA, the amount of HMTA is rate limiting. This behavior involves a multistage reaction of HMTA, which consists of the decomposition

of HMTA into an intermediate structure followed by a subsequent methylene linkage reaction [1]. Therefore, as a curing agent, HMTA has an effective functionality that is lower than the ideal value until the methylene linkage reaction occurs. The reaction of **NV** and HMTA proceeds more rapidly when a greater quantity of HMTA was used for **NVHX-16.7** and **NVHX-15**.

Table 3.1 Sample IDs and ^{13}C-NMR and GPC results.

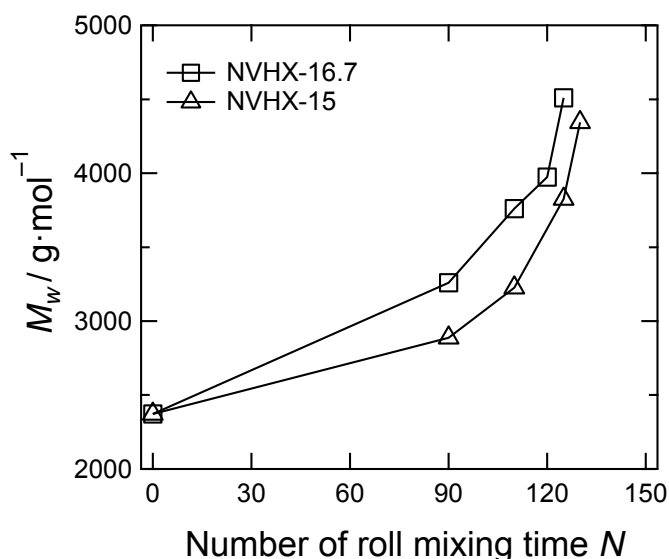| Sample ID	N	α	M_n / 10^3 g mol^{-1}	M_w / 10^3 g mol^{-1}
NVHX-16.7	0	0.589	0.980	2.37
	90	0.590	1.21	3.26
	110	0.591	1.61	3.76
	120	0.624	1.74	3.97
	125	0.630	2.70	4.51
NVHX-15	0	0.589	0.980	2.37
	90	0.590	1.16	2.89
	110	0.593	1.82	3.23
	125	0.618	2.30	3.83
	130	0.628	3.02	4.34

Figure 3.3   Changes in the weight-average molecular weights of **NVHX-16.7** and **NVHX-15** during open two-roll mixing.

The degree of reaction at the gel point (α_c) was estimated to be 0.63 for both resins. As previously mentioned, α is defined as the conversion of reactive sites on phenol based on classical gelation theory in this study. Drumm et al. reported α_c values of 0.763 for an initial formaldehyde/phenol molar ratio ($[CH_2]_0/[PhOH]_0$) of 0.60–0.85 using classical gelation theory and the average molecular weights [15–17]. Yamagishi et al. reported an α_c value of 0.78 for a $[CH_2]_0/[PhOH]_0$ ratio of 1.2 using Monte Carlo simulations for a gelation model [9,10]. Izumi et al. reported α_c values of 0.620, 0.647, and 0.680 for $[CH_2]_0/[PhOH]_0$ ratios of 1.0, 1.2, and 1.5, respectively, using rate equations derived by Aranguren et al. to investigate the reaction kinetics [18,19]. The α_c value of 0.63 obtained from the novolac/HMTA reaction is within the range of these reported values.

3.3.2 DLS

Figure 3.4 shows the changes in the $g^{(2)}(\tau)$ values for **NVHX-16.7** and **NVHX-15** as a function of N. The correlation function shifted toward a longer relaxation time as the reaction proceeded, which indicates an increase in the average molecular size due to the roll-mixing process. The $G(\Gamma)$ distribution functions of R_h in THF are shown in Figure 3.5. The shift in the distribution functions toward larger sizes indicates an increase in the molecular sizes. Interestingly, as the gel point is reached, significant changes in the distributions of both **NVHX-16.7** and **NVHX-15** are observed. Therefore, the order of magnitude of the right tail of the distribution increases from 10^2 ($N = 125$) to 10^4 Å ($N = 130$) during the last five mixing procedures. These results also support the conclusion that reactions between larger molecules become dominant as the gel point is reached.
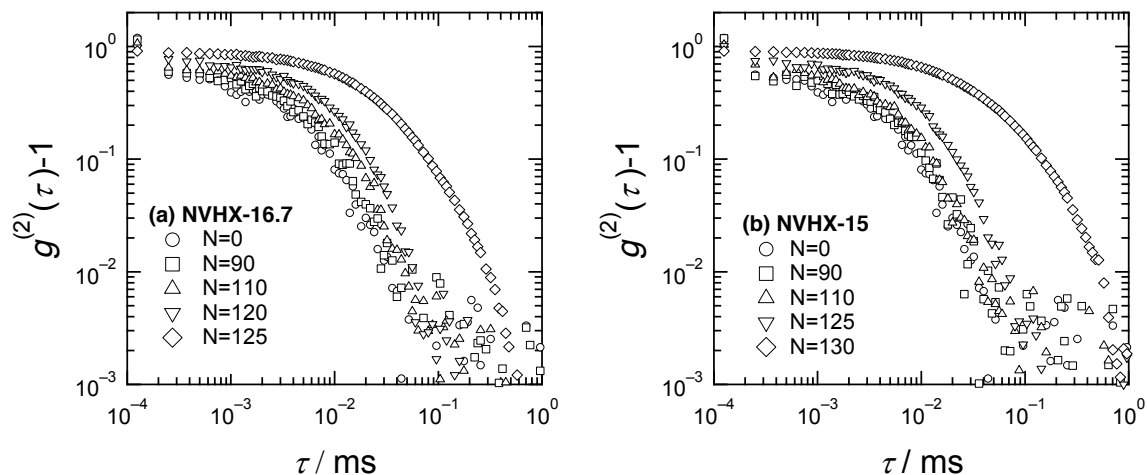
Figure 3.4 Time–intensity correlation functions of (a) **NVHX-16.7** and (b) **NVHX-15** in THF at 25 °C.
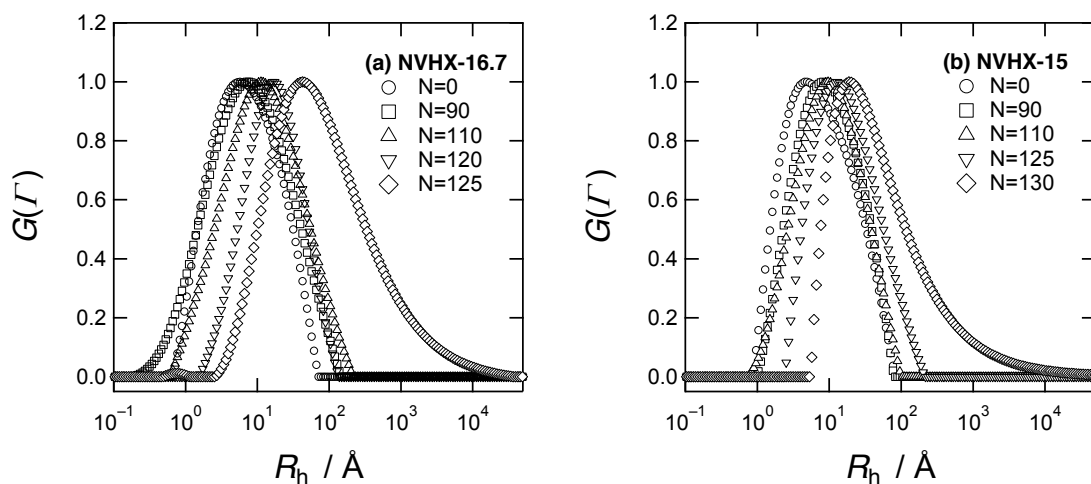

Figure 3.5 Distribution functions for the hydrodynamic radius of (a) **NVHX-16.7** and (b) **NVHX-15** in THF at 25 °C.

Figure 3.6 shows the changes in R_h (determined from Γ at the point of maximum $G(\Gamma)$) for **NVHX-16.7** and **NVHX-15** as a function of N. An increase in R_h was observed for both systems as the roll mixing proceeded even though **NVHX-16.7** grew faster and its molecular weight was greater than that of **NVHX-15**. In addition, a remarkable increase in R_h was observed in the vicinity of the gel point for both **NVHX-16.7** and **NVHX-15**. Therefore, the dependence of R_h on the molecular weight was studied to further investigate this behavior.
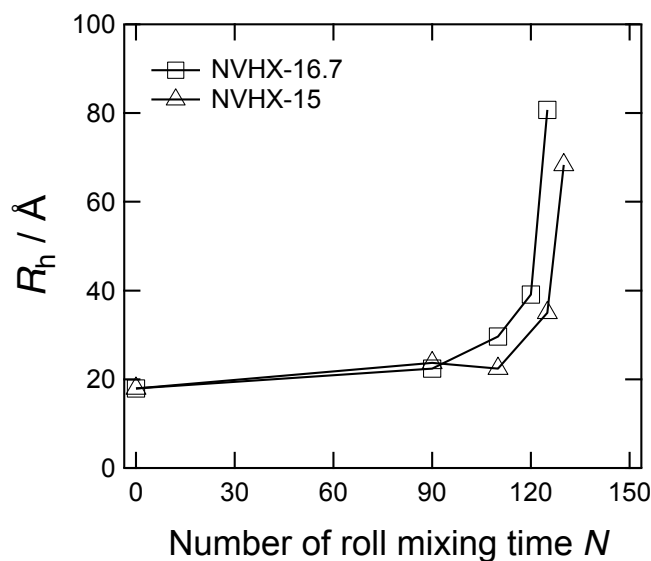
Figure 3.6 Changes in the hydrodynamic radius R_h of (a) **NVHX-16.7** and (b) **NVHX-15** during the open two-roll mixing process.

Figure 3.7 shows a plot of R_h as a function of M_w, where R_h and M_w exhibited a power-law behavior with an exponent value of 0.944 in a M_w range of 2,000 to 3,800 g mol^{-1}, which agrees with the previously reported value of 0.948 for phenolic resins prepared via by phenol-formaldehyde polycondensation [20]. However, a deviation from the power-law relationship was observed in a M_w range above 4,000 g mol^{-1}. This change in the relationship may be due to an overestimation of the R_h values due to the formation of larger molecules as the gel point is reached. As mentioned in ref. 20, the scattering intensity from large molecules should be dominant in the DLS results because the intensity is proportional to the sixth power of the size of the scatterer. In addition, it is difficult to estimate the average value of R_h for polymers with a broad molecular weight distribution, which has been observed for phenolic resins [21].
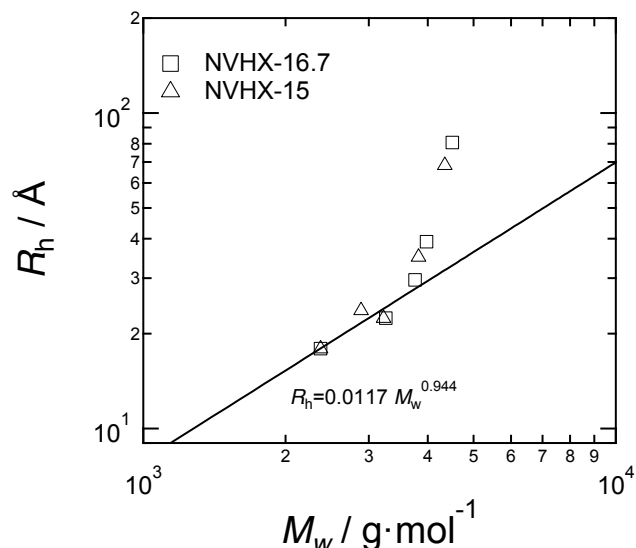
Figure 3.7 Hydrodynamic radius (R_h) as a function of the weight-average molecular weight (M_w). The solid line is the fitted result in a M_w range of 2,000–4,000 g mol^{-1}.

The distinct increase in R_h and the deviation from the power-law relationship as the gel point is reached may also be explained by the previously proposed curing mechanism for **NV** with HMTA, which involved a change in the mechanism during curing [1,22–25]. In particular, Zhang et al. investigated the curing mechanism using ^{13}C and ^{15}N NMR and reported that the decomposition of HMTA resulted in a decrease in the pH of the system. Because **NV** and HMTA are acidic and basic compounds, respectively, the decrease in the pH further accelerated the decomposition of HMTA and the formation of methylene crosslinkers [22]. In addition, hydrogen bond-stabilized benzoxazine and benzylamine were the major initial intermediates generated in the crosslinking reaction, and their decomposition resulted in crosslinking reactions via methylene linkages. A change in the reaction mechanism during the curing process was also reported by de Medeiros et al. based on kinetic analysis using the dynamic Ozawa method and DSC [23]. Therefore, the initial power-law relationship may correspond to chain growth of the **NV** resin along with the formation of intermediates, and the distinct increase in R_h and deviation from the power-law relationship may be due to crosslinking via methylene linkages, following the decomposition of the intermediates. In addition, these results indicate that based on the solution conformation, a large excess amount of HMTA does not affect the curing mechanism of **NV** below the gel point.

The values for the flexural modulus and strength of **NVHX-16.7** and **NVHX-15** after compression molding are shown in Table 3.2. **NVHX-16.7** exhibits a higher modulus and

strength compared with **NVHX-15**. However, there is no significant difference in the R_h–M_w relationship for the two resins. Therefore, the structural differences governing the mechanical properties are determined by the ratio of **NV** to HMTA (Figure 3.3) and formed after the gelation process. This result suggests that the curing mechanism is similar to that of the phenol-formaldehyde gelation systems [18,26]. The different rates observed for the R_h and M_w growth curves as a function of N for the resin systems with different **NV**/HMTA ratios should be expressed as the structural differences in the crosslinked structures after gelation. Because it is difficult to apply DLS analysis in the post-gel regime due to coloration and low transparency, SAXS and SANS analyses are indispensable tools for further structural analysis of the **NV**/HMTA reaction mixtures above the gel point [18,26,27].

Table 3.2 Flexural modulus and strength of molded phenolic resins.

Sample ID	Flexural Modulus / GPa	Flexural Strength / MPa
NVHX-16.7	6.2 ± 0.0	120 ± 20
NVHX-15	5.9 ± 0.0	110 ± 13

It is important to note that this study demonstrated the successful application of the open two-roll mixing mill to control the degree of reaction for the curing of **NV** with HMTA by varying the number of roll-mixing times (N). By controlling the degree of reaction, it was possible to investigate the critical behavior of the **NV**/HMTA system near the gel point.

3.4 Conclusions

The behavior of the novolac resin (**NV**) cured with hexamethylenetetramine (HMTA) in the pre-gel regime and the influence of an excess amount of HMTA on the curing reaction were investigated using DLS. A two-roll mixing mill process was applied to control the degree of reaction. The growth rates for the molecular weight and hydrodynamic radius of **NV** as a function of the number of mixing times were very different and dependent on the amount of HMTA. The plot of the hydrodynamic radius of **NV** in THF as a function of weight-average molecular weight indicated two different growth mechanisms during **NV** curing with HMTA in the pre-gel regime irrespective of the amount of HMTA. An initial power-law relationship with a scaling exponent of 0.94 and a subsequent large deviation from this relationship were observed. As the gel point was reached, intermolecular reactions between larger molecules

became dominant due to crosslinking via methylene linkages, which occurred after the decomposition of the initially formed HMTA decomposition products.

These results suggest that the structural differences governing the mechanical properties of phenolic resins are established in the pre-gel stage followed by noticeable differences in the mechanical properties during the subsequent curing process. To further elucidate the curing mechanism, SAXS and SANS analyses of the gelation process [18,26,27], atomistic MD simulations of crosslinked network structures [11,12], and refinement of the gelation kinetics using statistical approaches, such as the cascade theory [13,14], are promising methods.

References

1. A. Gardziella, L. A. Pilato, and A. Knop, *Phenolic Resins: Chemistry, Applications, Standardization, Safety and Ecology*, second ed., Springer: Berlin, 2000.

2. *Phenolic Resins: A Century of Progress*, L. Pilato, Ed., Springer: Berlin, 2010.

3. S. A. Sojka, R. A. Wolfe, and G. D. Guenther, *Macromolecules*, 1981, **14**, 1539–1543.

4. M. Nomoto, T. Yamagishi, and Y. Nakamoto, *J. Network Polym. Jpn.*, **27**, 210–217 (2006).

5. B. J. Berne, and R. Pecola, *Dynamic Light Scattering With Applications to Chemistry, Biology, and Physics*, Wiley: New York, 1976.

6. S. W. Provencher, *Comput. Phys. Commun.*, 1982, **27**, 213–227.

7. C. L. Yaws, *Handbook of viscosity*, Gulf Professional Publishing: Houston, 1995.

8. C. Wohlfarth, and B. Wohlfarth, *Optical Constants: Subvolume B: Refractive Indices of Organic Liquids.*, M. D. Lechner, Eds., Springer: Berlin, 1996.

9. T. Yamagishi, T. Nakatogawa, M. Ikuji, Y. Nakamoto, and S. Ishida, *Angew. Makromol. Chem.*, 1996, **240**, 181–186.

10. T. Yamagishi, Y. Nakamoto, and S. Ishida, *Kobunshi Kako, Jpn.*, 1999, **34**, 178–183.

11. A. Izumi, T. Nakao, and M. Shibayama, *Soft Matter*, 2012, **8**, 5283–5293.

12. I. Yarovsky, and E. Evans, *Polymer*, 2002, **43**, 963–969.

13. T. Nakao, F. Tanaka, and S. Kohjiya, *Macromolecules*, 2002, **35**, 5649–5656.

14. T. Nakao, F. Tanaka, and S. Kohjiya, *Macromolecules*, 2006, **39**, 6643–6652.

15. M. F. Drumm, and J. R. Leblanc, In *Step Growth Polymerizations*, D. H. Solomon, Ed., Marcel Decker: New York, p. 157–276, 1972.

16. J. Borrajo, M. I. Aranguren, and R. J. J. Williams, *Polymer*, 1982, **23**, 263–266.

17. W. H. Stockmayer, *J. Chem. Phys.*, 1943, **11**, 45–55.

18. A. Izumi, T. Nakao, and M. Shibayama, *Soft Matter*, 2013, **9**, 4188–4197.

19. M. I. Aranguren, J. Borrajo, and R. J. J. Williams, *Ind. Eng. Chem. Prod. Res. Dev.*, 1984, **23**, 370–374.

20. A. Izumi, T. Takeuchi, and M. Shibayama, *Polymer*, 2011, **52**, 4355–4361.

21. M. Shibayama, T. Karino, and S. Okabe, *Polymer*, 2006, **47**, 6446–6456.

22. X. Zhang, M. G. Looney, D. H. Solomon, and A. K. Whittaker, *Polymer*, 1997, **38**, 5835–5848.

23. E. S. de Medeiros, J. A. M. Agnelli, K. Joseph, L. H. de Carvalho, and L. H. C. Mattoso, *J. Appl. Polym. Sci.*, 2003, **90**, 1678–1682.

24. Z. Katovic, and M. Stefanic, *Ind. Eng. Chem. Prod. Res. Dev.*, 1985, **2**, 179–185.

25. M. G. Looney, and D. H. Solomon, *Aust. J. Chem.*, 1995, **48**, 323–331.

26. A. Izumi, T. Nakao, M. Shibayama, *Polymer*, 2015, **59**, 226–233.

27. A. Izumi, T. Nakao H. Iwase, and M. Shibayama, *Soft Matter*, 2012, **8**, 8438–8445.

Chapter 4

Crosslink Inhomogeneity in Phenolic Resins at the Initial Stage of Curing Studied by ^{1}H-pulse NMR Spectroscopy and Complementary SAXS/WAXS and SANS/WANS with a Solvent-Swelling Technique

4.1 Introduction

In this chapter, the author focuses on further elucidation of the cross-link inhomogeneity in phenolic resins at the initial stage of curing process beyond the gel point by investigating the network structure evolution mechanism in a temperature range of 110–130 °C through structural analysis of the HMTA-curing system using ^{1}H-pulse NMR spectroscopy, SAXS/WAXS, and small- and wide-angle neutron scattering (SANS and WANS, respectively) in conjunction with the solvent-swelling technique.

 ^{1}H-pulse NMR spectroscopy can provide information about the dynamics of the molecular mobility of polymer segments in the network structure [1–4]. These dynamics are related to the nuclear spin–spin relaxation behavior, also referred to as transverse relaxation decay, of the attached protons on applying a specific external magnetic field. Using this technique, the relaxation behavior can be studied as a change in macroscopic magnetization of the protons, where a lower molecular mobility corresponds to a shorter the relaxation time and vice versa. In cross-linked polymers, the molecular mobility of the polymer segments strongly depends on their local cross-link density, i.e., the mobility of the polymer segments in a high-cross-link-density domain (HXD) with a small mesh size is lower than that in a low-cross-link-density domain (LXD) with a large mesh size [5]. X-ray and neutron scattering have also proven to be powerful techniques for elucidating the cross-link inhomogeneity of polymer gel networks [6–10]. These scattering techniques reveal nanometer-scale structural details of a material by exploiting scattering length density fluctuations of electron and atomic nuclei therein, which scatter X-rays and neutrons, respectively. The use of both these scattering techniques can provide complementary information about a material because of the differences in the scattering

phenomena. In most studies of polymer gels, the NMR and scattering methods use the swelling features of the gel because swelling enhances the local fluctuations in the cross-link density, resulting in large contrasts in the dynamics and scattering length density; that is, the solvent-swollen polymer gels are more informative than those in the bulk state for NMR and scattering analyses of the cross-link inhomogeneity.

4.2 Experimental

4.2.1 Materials

A novolac-type phenolic resin oligomer (NV) with polystyrene-based weight- and number-average molecular weights of 3400 and 870 g mol^{-1}, respectively, was provided by Sumitomo Bakelite Co., Ltd. (Japan). HMTA was purchased from Chang Chun Petrochemical Co., Ltd. (Taiwan). Methanol (MeOH) and methanol-d_4 (MeOH-d_4) with a 99.8% degree of deuteration were purchased from Wako Pure Chemical Industries, Ltd. (Japan). All materials were used without further purification.

Curing reactions of NV with HMTA were performed using NV/HMTA weight ratios of 1/0.06 (**PR06**) and 1/0.12 (**PR12**), representing curing systems with stoichiometrically insufficient and sufficient amounts of cross-linker, respectively. It should be noted that the equivalent stoichiometric ratio in this curing system is 1/0.138 (wt/wt) based on the number-average molecular weight of NV, assuming NV to be a linear polymer with no branching structure. A mixture of NV/HMTA (50 g) was heated to melting at 100 °C under a pressure of 45 kPa for 5 h in a disk-shaped mold, then the resulting disk-shaped resin was milled and powdered at room temperature. Figure 4.1 shows a differential scanning calorimetry (DSC) thermogram of the powdered **PR12** that was recorded on a DSC-6220 (Seiko Instruments Inc., Japan) at a heating rate of 5 °C min^{-1}. The DSC result shows that the mixture has one broad exothermic region owing to cross-linking reactions, for which the onset temperature is 110 °C and the peak is at 136 °C. Based on the DSC result, curing reactions of **PR06** and **PR12** were performed in the range 110–130 °C to investigate behavior at the initial stage of the curing process. The procedure for the curing reaction was as follows. The powdered sample was heated at 110 °C under 45 kPa for 5 h in the mold. The resulted resin was milled and powdered. A 5-gram sample was then collected for analysis, and the rest of the powder was subjected to further curing. This heating-and-milling procedure was repeated stepwise in +5 °C increments to promote further reaction until 130 °C. Here the reaction time of 5 h was chosen to complete the

40

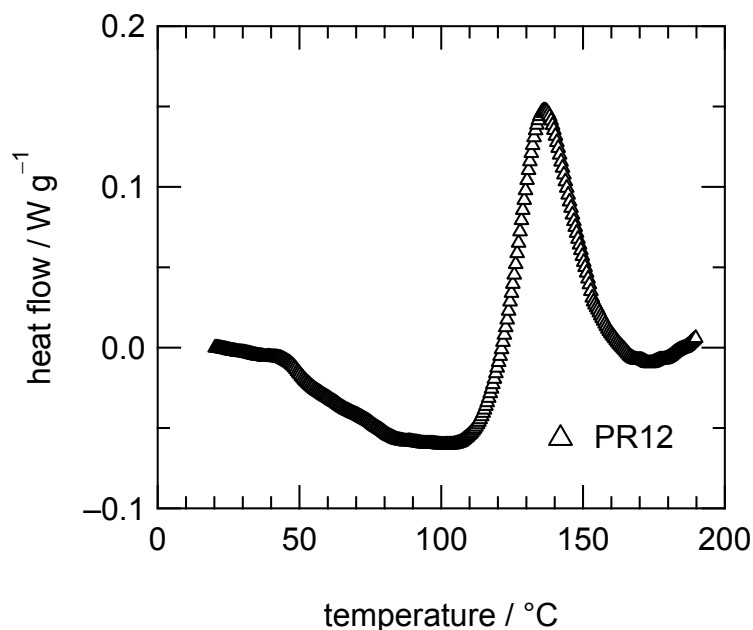reaction at the respective temperature under molding pressure.

Figure 4.1 DSC thermogram of **PR12** prepared at 100 °C.

A 2-gram sample of the powder obtained at each temperature was stirred in a large amount of MeOH to extract the MeOH-soluble components, followed by centrifugation and collection of the MeOH-insoluble gels. This procedure was repeated three times, and the MeOH-insoluble gels were obtained in a fully MeOH-swollen state. It should be noted that there are many good solvents for phenolic resins such as tetrahydrofuran, MeOH, and acetone; however, methanol was chosen in this study because of the better solubility of HMTA.

4.2.2 Gel Fraction

The gel fraction was calculated as the weight ratio of the MeOH-insoluble component of the 2-gram powder sample, which was estimated from the weight of the MeOH-soluble component obtained by drying the combined extracts in vacuum.

4.2.3 Degree of Swelling of the Gel

Degree of swelling of the MeOH-insoluble gel (D_{swell}) was calculated as the volume ratio VV_0^{-1}, where V and V_0 denote the sample volumes before and after drying the fully MeOH-swollen gel, respectively. The sample volumes were estimated from their weights and densities, in

41

which the densities of the MeOH and the phenolic resins were approximated to be 0.79 and 1.25 g mol^{-1}, respectively. The value of D_{swell} was obtained as the average of three measurements.

4.2.4 ^{1}H-pulse NMR spectroscopy

The ^{1}H-pulse NMR experiments were performed using an MQC23 benchtop NMR analyzer (Oxford Instruments plc, United Kingdom) with a 10-mm-diameter probe operated at 23 MHz. The MeOH-d_4-swollen phenolic resins were used as specimens to observe only the NMR signals of protons in the phenolic resins. Glass NMR tubes with a diameter of 10 mm and a wall thickness of 0.6 mm (JEOL RESONANCE Inc., Japan) were used for the sample cells. The spin–spin relaxation decay was recorded at 40 °C using Carr–Purcell–Meiboom–Gill pulse sequences. The pulse width, pulse interval (τ), number of $(180° - 2\tau)$-loops, relaxation delay between subsequent scans, and number of scans were set to 2.0 μs, 50 μs, 4096, 10 s, and 128, respectively.

4.2.5 SAXS and WAXS

SAXS measurements over a q range of 0.02–7 nm^{-1} were performed on a BL03XU beamline, which is known as the Frontier Softmaterial Beamline (FSBL), at SPring-8, Hyogo, Japan [11,12]. Here, q denotes the magnitude of the scattering vector given by $q = (4\pi \lambda^{-1}) \sin (2\theta/2)$, where λ and 2θ denote the wavelength of the incident beam and the scattering angle, respectively. The measurements were performed at a sample-to-detector distance (SDD) of 3.4 m with a λ of 0.15 nm under vacuum using a windowless SAXS setup, and at an SDD of 1.2 m with a λ of 0.10 nm in air. The windowless SAXS setup was applied to achieve a higher signal-to-background scattering ratio by reducing background air scattering. The scattered X-rays were counted by an R-AXIS VII imaging plate detector system (Rigaku Corporation, Japan) with a 3,000 × 3,000 pixel array and a pixel size of 0.1 mm pixel^{-1}. WAXS measurements over a q range of 5.0–20 nm^{-1} were performed on a NANO-Viewer (Rigaku Corporation, Japan) using an X-ray beam with a λ of 0.154 nm from a CuKα spectral line excited at 40 kV and 30 mA. The scattered X-rays were counted by a Pilatus 100K detector system (DECTRIS Ltd., Switzerland) with a 487 × 195 pixel array and a pixel size of 0.172 mm pixel^{-1} at an SDD of 76 mm. Quartz glass capillaries Mark-Tube (Hilgenburg GmbH, Germany) with a diameter of 2 mm and a wall thickness of 0.01 mm were used as sample cells. The open top of the glass

capillary was sealed using the silylated polyurethane adhesive (Konishi Co., Ltd., Japan) in order to place the MeOH-containing capillaries in the vacuum chamber. After correction for dark noise from the R-AXIS detector and defective pixels of the Pilatus detector, the transmittance, and background scattering, the scattering intensity was normalized to an absolute intensity scale with units of cm^{-1} using a 1-mm-thick glassy carbon plate (glassy carbon Type 2, Alfa Aesar, USA) as a secondary standard to combine the SAXS and WAXS data. The absolute scattering intensity function of the glassy carbon plate was determined using a previously calibrated glassy carbon plate [13].

4.2.6   SANS and WANS

SANS and WANS measurements over a q range of 0.08–170 nm^{-1} were performed on the BL15 beamline, which is known as "TAIKAN," installed in the Materials and Life Science Experimental Facility (MLF) of J-PARC, Tokai, Ibaraki, Japan. The MeOH-d_4-swollen phenolic resins were used instead of the MeOH-swollen phenolic resins to increase the coherent neutron scattering contrast between the phenolic resins and the solvent, and to reduce neutron incoherent scattering background noise from the solvent, which result from large differences in the coherent neutron scattering length and the incoherent neutron scattering cross section between ^{1}H and ^{2}H, respectively [14]. Sealable 2-mm-thick rectangular quartz cells (MITORIKA Co., Ltd. (formerly Mitorika Glass Co., Ltd.), Japan) with a width and height of 22 and 45 mm, respectively, and a glass thickness of 1.0 mm were used as sample cells. A 10-mmφ neutron beam with a λ of 0.05–0.78 nm was used for measurement, and scattered neutrons were counted by a time-of-flight method using ^{3}He-position sensitive detectors mounted at four detector banks, i.e., small-, middle-, and high-angle banks, and a backward bank. The obtained two-dimensional scattering data were converted to one-dimensional data using a beamline specific data reduction program, in which the scattering data with a λ of 0.07–0.76 nm was used for the data reduction. The one-dimensional data obtained have a very wide q range of 0.08–170 nm^{-1}; however, the scattering data with $q > 30$ nm^{-1} was not used for further investigation in this study because an additional correction for inelastic neutron scattering is required for data in that range. The details of the instrument, data acquisition, and data reduction procedures are described in the literature [15].

4.3 Results and Discussion

4.3.1 Gel Fraction

To understand the network structure evolution mechanism at the initial stage of the curing process from the macroscopic viewpoint, the MeOH-insoluble gel fraction in the cured phenolic resins and its degree of swelling in MeOH were first investigated. Figure 4.2 shows the change in the gel fraction as a function of curing temperature. The gel fractions of **PR06** and **PR12** exceed 0.6 and 0.7, respectively, at 110 °C, and show a slight increase with curing temperature, which clearly indicates that the phenolic resins are well beyond the gel point. The progress of the cross-linking reaction beyond the gel point at 110 °C seems to be in contradiction to the DSC result shown in Figure 4.1; however, this could be explained by the effect of the molding pressure, which accelerates the reaction in the mold.
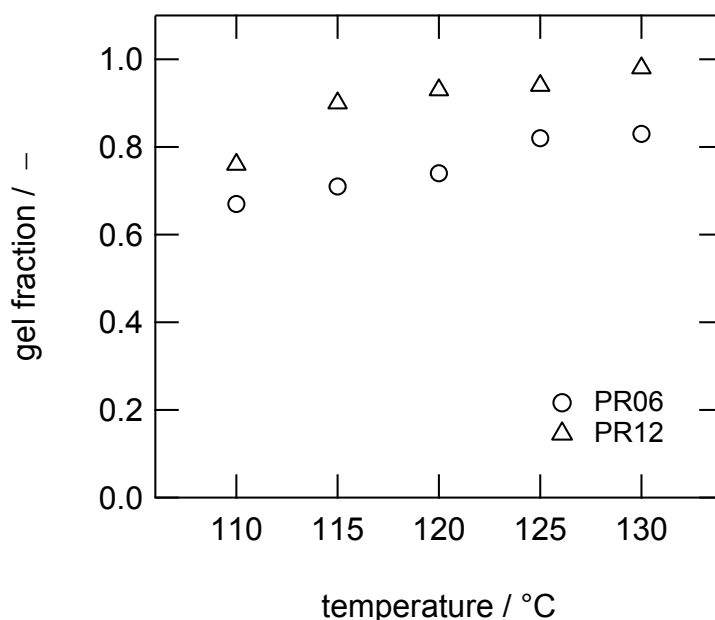

Figure 4.2 Change in the MeOH-insoluble gel fraction: circles, **PR06**; and triangles, **PR12**.

Figure 4.3 shows the change in D_{swell} as a function of curing temperature, which was calculated as a ratio of the volume change. The value D_{swell} for **PR06** gradually decreases from 4.2 to 2.8 with curing temperature, whereas that for **PR12** remains approximately constant at ca. 2.0. The values 4.2–2.8 and 2.0 correspond to swelling ratios of the length change of 1.6–1.4 and 1.3 assuming isotropic swelling. A decrease in D_{swell} can be generally explained by a decrease in the average mesh size of the cross-linked network structure owing to an increase in the degree of cross-linking [16]; however, another mechanism should be considered for **PR12**, which exhibits a constant D_{swell}. A possible network structure evolution mechanism that results

in the behavior of **PR12** is that there are high- and low-cross-link-density domains (HXDs and LXDs, respectively) owing to the cross-link inhomogeneity and percolation of the HXD occurs at 110 °C. The percolated domains dominate the degree of swelling of the gel, in which the degree of swelling of the domain is 2.0. Consistent with this conjecture, **PR06** may also exhibit percolation of the HXD that dominates the degree of swelling of the gel. In this case, the decrease in D_{swell} could be explained by assuming that the degree of cross-linking in the HXD of PR06 is lower than that in **PR12**, and the degree of cross-linking gradually increases with curing; that is, the well-developed, tightly cross-linked network structure results in a constant value for D_{swell} irrespective of the curing temperature, whereas the degree of cross-linking in the loosely cross-linked network structure increases via intradomain reactions accompanying a decrease in D_{swell} with the curing temperature. Here, the presence of tightly and loosely cross-linked network structures in the HXD could be explained by different gelation mechanisms near the gel point, which depend on the stoichiometric amount of cross-linker [17,18]. To investigate the mechanisms of the network structure evolution of **PR06** and **PR12** more precisely, a ^{1}H-pulse NMR analysis and complementary X-ray and neutron scattering analyses have been performed in the following subsections.
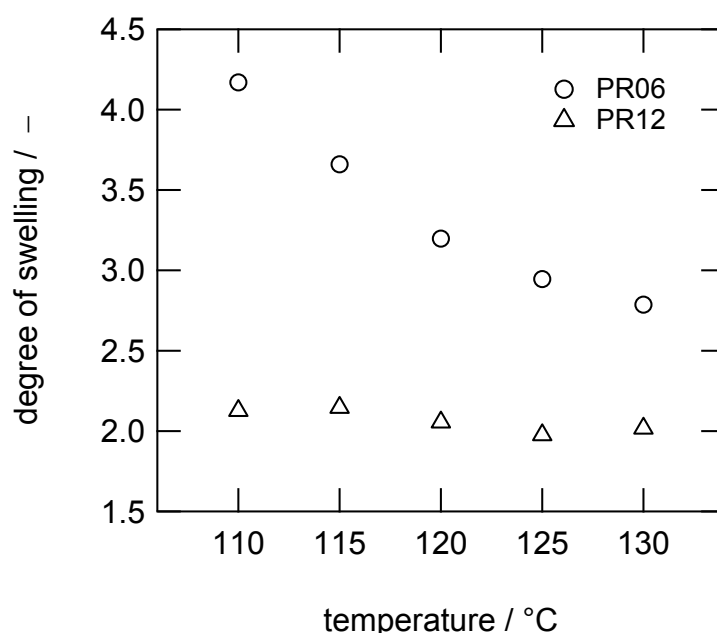

Figure 4.3   Change in the degree of gel swelling in MeOH: circles, **PR06**; and triangles, **PR12**.

4.3.2   ^{1}H-pulse NMR

The nuclear spin–spin relaxation time function of protons is generally described by

$$\frac{M(t)}{M(0)} = \exp\left[-\frac{1}{a}\left(\frac{t}{T_2}\right)^a\right],\tag{4.1}$$

where t, $M(t)/M(0)$, a, and T_2 denote the decay time, normalized magnetization intensity at t, exponent of the decay function, and time constant representing the nuclear spin–spin relaxation of protons, respectively [1–3]. The value a ranges from 1 for an exponential-type slow decay to 2 for a Gaussian-type fast decay. When the molecular mobility of the polymer segments is less constrained, such as in the rubbery and solution states, the relaxation function typically follows exponential-type slow decay. Conversely, when the mobility is highly constrained, such as in the glassy and crystalline states, the function typically follows Gaussian-type fast decay. Our previous study demonstrated that the molecular mobility of solvent-swollen phenolic resins having cross-link inhomogeneity can be classified into three relaxation modes with the value a of 1, and the spin–spin relaxation function can be expressed with a triple-exponential function given by

$$\frac{M(t)}{M(0)} = \varphi_1 \exp\left(-\frac{t}{T_{2,1}}\right) + \varphi_2 \exp\left(-\frac{t}{T_{2,2}}\right) + \varphi_3 \exp\left(-\frac{t}{T_{2,3}}\right),\tag{4.2}$$

where φ_i and $T_{2,i}$ with $i = 1$, 2, and 3 denote the molar fraction of protons and time constant T_2 in the polymer segments of the i-th relaxation mode, respectively, in which the function was derived by a distribution analysis of T_2. Here, $\varphi_1 + \varphi_2 + \varphi_3 = 1$ and $T_{2,1} < T_{2,2} < T_{2,3}$. The first relaxation mode results from the spin–spin relaxations of protons in polymer segments in the HXD where molecular mobility is highly constrained by the cross-links. The third relaxation mode results from the relaxations in the LXD where molecular mobility is less constrained. The second relaxation mode results from the relaxation at the interface region between the HXD and LXD [18].

Figure 4.4 shows the spin–spin relaxation decay of **PR06** and **PR12** in the fully-MeOH-d_4 swollen state, in which solid lines are the fitting curves using Equation (4.2). The decay occurs faster with increased curing temperature, which clearly suggests a decrease in the average mesh size of the cross-linked network structure owing to the progress of curing.
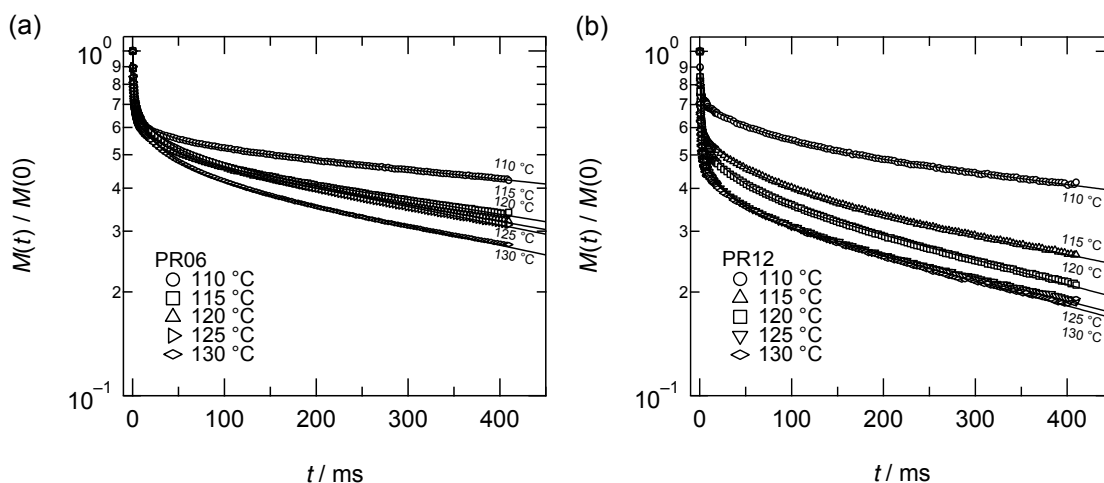
Figure 4.4 Proton nuclear spin–spin relaxation decay in MeOH-d_4: (a) **PR06** and (b) **PR12**.

Figure 4.5(a) s hows the fitting parameters $T_{2,1}$, $T_{2,2}$, and $T_{2,3}$ as a function of curing temperature with a logarithmic scale on the vertical axis, and Figure 4.5(b) shows a re-plot of $T_{2,3}$ with a linear scale on the vertical axis. All the spin–spin relaxation decays shown in Figure 4.5 clearly exhibit three different relaxation modes with time constants in the orders of magnitude of 10^0, 10^1, and 10^2–10^3 ms, which are associated with the first, second, and third relaxation modes, respectively. As seen in Figure 4.5(a), **PR06** and **PR12** exhibit almost the same values of $T_{2,1}$ and $T_{2,2}$, which suggests that they have essentially the same mesh size in the HXD and the interface region. This seems to contradict the conjecture in the previous subsection that the degree of cross-linking in the HXD of **PR06** is lower than that of **PR12**; however, the mesh size may be too small to affect the dynamics of the polymer segment in the domain under the NMR measurement conditions of this study. Further analysis focusing on the faster relaxation decay would provide more precise information for the HXDs. As seen in Figure 4.5(b), the larger $T_{2,3}$ value for **PR06** than that for **PR12** indicates that the network structure of the LXD of **PR06** has a larger average mesh size than that of **PR12**, which results from the difference in the amount of cross-linker. The figure also shows that $T_{2,3}$ of **PR06** and **PR12** exhibits a steep decrease at the beginning of curing, which results from a decrease in the average molecular mobility of the polymer segments in the LXD.
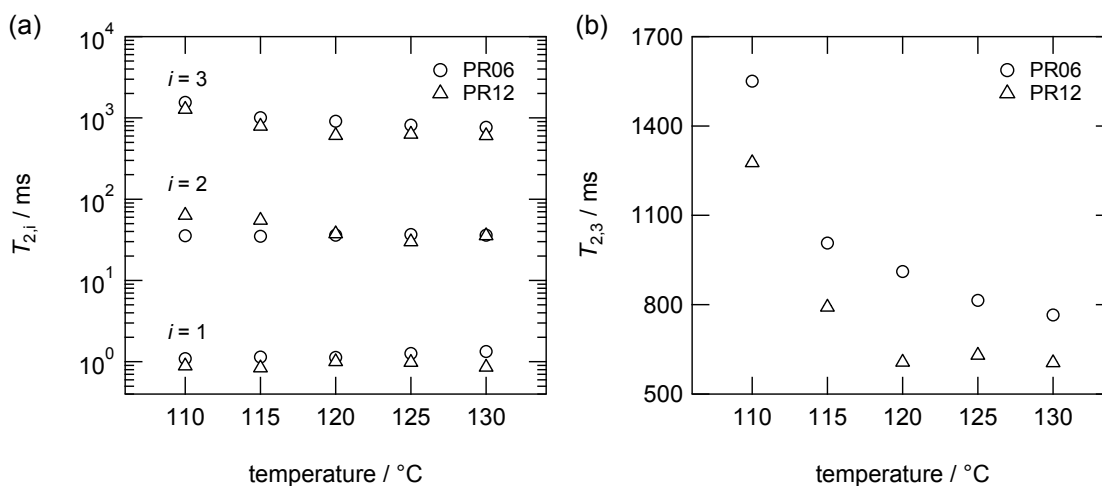
Figure 4.5 (a) Change in $T_{2,n}$ (n = 1, 2, and 3) and (b) $T_{2,3}$ as a function of curing temperature: circles, **PR06**; and triangles, **PR12**. (b) Re-plot of $T_{2,3}$ as a function of curing temperature in a linear scale on the vertical axis.

Figure 4.6(a) shows the change in the values φ_1, φ_2, and φ_3 as a function of the curing temperature. There is an insignificant change in each φ_i value for **PR06** and **PR12** over the temperature range of 115–130 °C, with the exception of a slight change at the beginning of the curing reaction from 110 to 115 °C. The smaller φ_2 value of 0.1–0.2 indicates that the structure defined as the interface region is a minor fraction in the network structure. Here, we introduce the parameter φ_{1+2}, which is the sum of φ_1 and φ_2, to simplify the structural model into two structures with a smaller T_2 of 10^0–10^1 ms and a larger T_2 of 10^2–10^3 ms because, although the interface region is necessary to explain the observed relaxation decay in the swollen state, the definition of the interface structure is ambiguous at present. The value φ_{1+2} represents the molar fraction of protons in the polymer segments whose molecular mobility is suppressed by the cross-links in the swollen state; therefore, this value could be related to the volume fraction of the HXDs in the dry state. The change in the value of φ_{1+2} as a function of the curing temperature is shown in Figure 4.6(b). The value φ_{1+2} for **PR12** is larger than that for **PR06** with an exception at 110 °C, which indicates that the dry-state volume fraction of the HXD in **PR12** is larger than that in **PR06**, which would result from a stoichiometrically larger amount of cross-linker. Figure 4.6(b) also shows that there is a slight but insignificant change in both the φ_{1+2} values for **PR06** and **PR12** over the temperature range of 115–130 °C. Here, the slight increase in φ_{1+2} indicates a slight increase in the size of the HXD in the dry state, while the absence of any significant change in φ_{1+2} indicates that the spatial location and size of the HXD in the dry state are determined at the beginning of the curing process and are essentially unchanged during

the investigated temperature range. This conjecture could be explained by intradomain reactions being dominant in the initial curing process compared with interdomain reactions. It should be noted that the nature of the intradomain and interdomain reactions plays an important role in the growth of network structures of phenolic resins with cross-link inhomogeneity [18]. When the interdomain reaction between the HXD and LXD proceeds via the interface region, some part of the LXD is incorporated into the HXD accompanying an increase and a decrease in the number of protons in the HXD and LXD, respectively; hence, the interdomain reaction results in a distinct increase in the value φ_{1+2}. Conversely, the intradomain reaction in each domain is a reaction between unreacted sites inside the domain, which leads to no significant structural change of the domain. Thus, the intradomain reaction results in no significant change in the time constant T_2, number of protons, spatial location, and volume of the domain. This accounts for the absence of significant change in the values of φ_{1+2} for **PR06** and **PR12** during the curing.
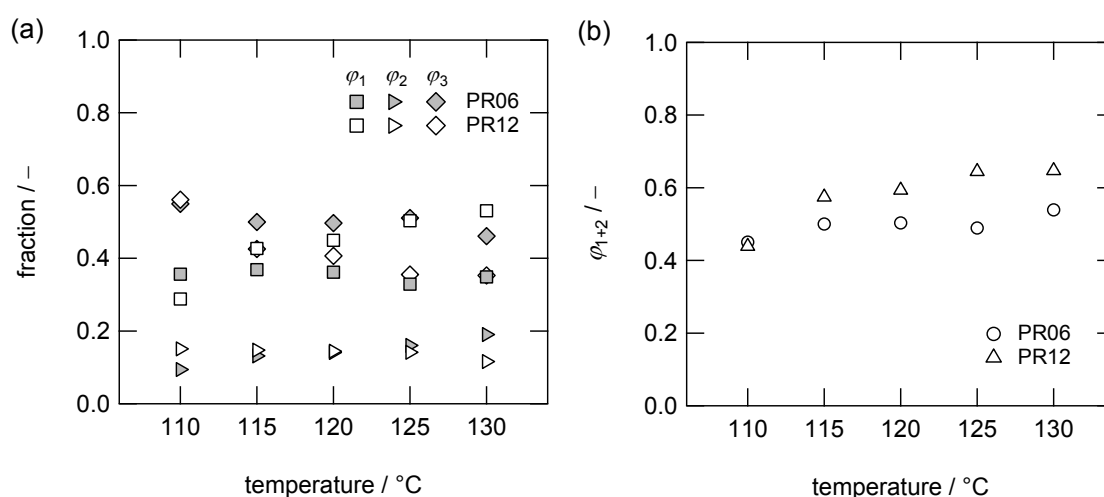

Figure 4.6 (a) Changes in φ_1, φ_2, and φ_3 as a function of the curing temperature: squares, φ_1; right-pointing triangles, φ_2; diamonds, φ_3; filled symbols, **PR06**; and open symbols, **PR12**. (b) Change in φ_{1+2} as a function of curing temperature: circles, **PR06**; and triangles, **PR12**.

4.3.3 SAXS and WAXS

According to previous SAXS and SANS studies, small-angle scatterings from polymer gels can be explained by considering the solid-like crosslink inhomogeneity and the liquid-like concentration fluctuation of polymer chains [7–10,14]. The scattering functions of the inhomogeneity and the concentration fluctuation are generally represented by the squared-Lorentzian equation [19] ($I_{SL}(q)$) and the Ornstein–Zernike equation [19] ($I_{OZ}(q)$), respectively,

and their combined scattering function has long been used to represent the structure of gels having crosslink inhomogeneity, which is given by

$$I(q) = \frac{I_{SL}(0)}{(1 + \Xi^2 q^2)^2} + \frac{I_{OZ}(0)}{1 + \xi^2 q^2},$$
(4.3)

where $I(q)$, Ξ, and ξ denote the scattering intensity at q, and correlation lengths representing the characteristic size of inhomogeneity and that of the concentration fluctuation, respectively. Our previous studies demonstrated that this combined function is also applicable to phenolic resins when they are in the solvent swollen state [17,18]. For fully swollen phenolic resins, Ξ is related to the characteristic size of the inhomogeneity associated with the average sizes of the HXDs and LXDs, and ξ is related to the average mesh size of the LXD that behaves like a polymer chain in semidilute regime. It should be noted that this structural information for solvent swollen phenolic resins could be obtained in a small-angle scattering region with a q range of 10^{-2}–10^0 nm^{-1}; however, a combination of SAXS and WAXS experiments over an extended q range of 10^{-2}–10^1 nm^{-1} allows more precise analysis because the effect of X-ray scattering owing to the concentration fluctuation typically reaches a wide-angle scattering region of $q > 10^0$ nm^{-1} [17,18].

Figure 4.7 shows the combined SAXS and WAXS curve for **PR06** cured at 120 °C for 5 h, in which the curve was obtained in the fully MeOH-swollen state, and also includes solvent scattering. For curve fitting analysis over the wide q range of 0.03–20 nm^{-1}, three additional correction terms for Equation (4.3) were adopted; (i) surface scattering from MeOH-swollen gel particles with sizes larger than the micrometer scale or, more precisely, with sizes that can be observed below the experimental lower q limit, (ii) scattering from short-range electron density fluctuation of phenolic resins in the order of magnitude of 10^{-1} nm, and (iii) solvent scattering. The contribution of the terms (i) and (ii)–(iii) can be observed as scattering intensity upturns in the SAXS region of $q < 0.07$ nm^{-1} and in the WAXS region of $q > 6$ nm^{-1}, respectively. Thus, the theoretical scattering function of Equation (4.3) is revised to

$$I(q) = Aq^{-4} + \frac{I_{SL}(0)}{(1 + \Xi^2 q^2)^2} + \frac{I_{OZ}(0)}{1 + \xi^2 q^2} + B \exp\left[-\frac{(q - q_0)^2}{2w^2}\right] + CI_{MeOH}(q),$$
(4.4)

where A, B, and C represent scaling factors, q_0 and w denote peak position and width of a Gaussian function, respectively, and $I_{MeOH}(q)$ denotes the experimentally determined scattering function of MeOH. The first, fourth, and fifth terms on the right side of the equation correspond to the terms (i), (ii), and (iii), respectively, and the first term is known as Porod's law for flat-and-smooth surfaces [14]. The fitting curve using Equation (4.4) is shown in Figure 4.7 by a

solid line, and each of the five terms on the right of the Equation (4.4) is also represented in order to clarify their individual contribution to the scattering intensity. The results clearly show that Equation (4.4) accurately reproduces the observed X-ray scattering curve for the MeOH-swollen **PR06** over the wide q range of 0.03–20 nm^{-1}.

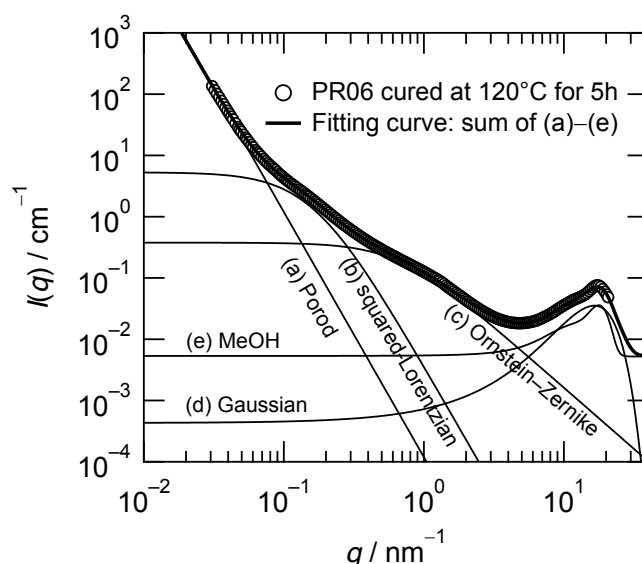**Figure 4.7**   Combined SAXS and WAXS curve for **PR06** cured at 120 °C. Solid lines are fitting curves of Equation (4.4) and the five terms comprising the equation.

Figures 4.8(a) and (b) show changes in the X-ray scattering curves for **PR06** and **PR12**, respectively, in the fully-MeOH swollen state as a function of curing temperature. Solid lines are the fitting curves using Equation (4.4), which indicates the curve fitting is successful for all scattering data. Figure 4.9 shows the change in the fitting parameters Ξ and ξ as a function of curing temperature. The results clearly show that both **PR06** and **PR12** exhibit almost the same values of Ξ and ξ at the respective temperature and curing proceeds with a decrease in Ξ while ξ remains constant, which indicates that the behavior of the network structure evolution with the cross-link inhomogeneity is essentially the same irrespective of the NV/HMTA-ratio.
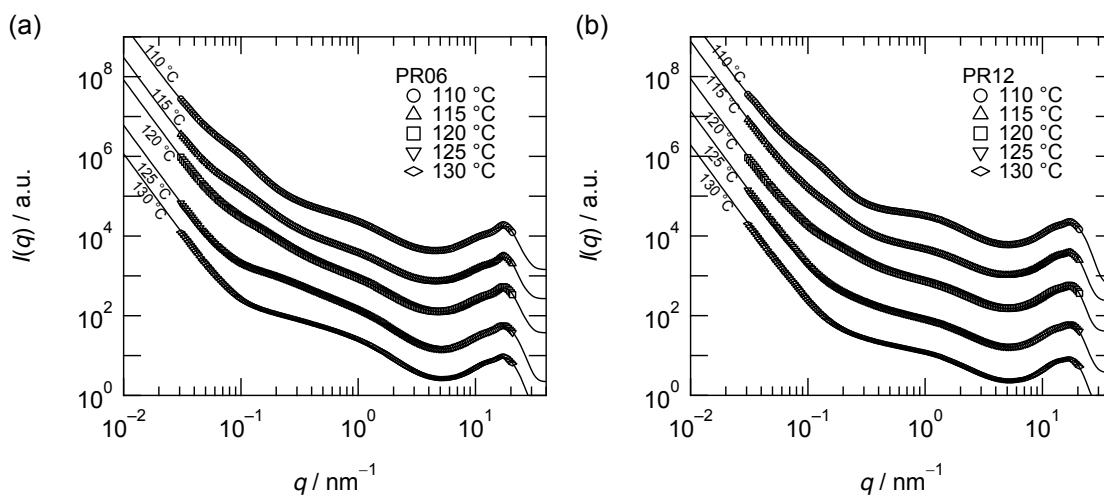
51

Figure 4.8   Change in SAXS and WAXS curves as a function of curing temperature: (a) **PR06** and **PR12** in MeOH. Solid lines are fitting curves using Equation (4.4). The curves are arbitrarily vertically shifted to improve visibility.
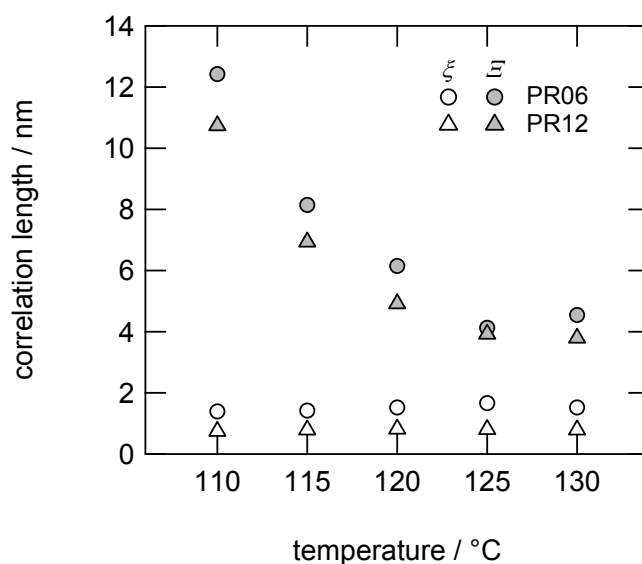

Figure 4.9   Change in the fitting parameters of X-ray scattering curves as a function of curing temperature: circles, **PR06**; and triangles, **PR12**.

The value of ξ being independent of the curing temperature indicates that the average mesh size of the LXD can be determined at the beginning of the curing, and remains unchanged during the initial curing process. The behavior of the values $T_{2,3}$ and ξ indicates that molecular mobility of the polymer segments in the LXD decreases without affecting the mesh size of the domain with increased curing temperature. This can be explained by considering that $T_{2,3}$ could be more significantly affected by polymer segments with very high molecular mobility, such

as dangling chains in the domain; i.e., the steep decrease in $T_{2,3}$ as seen in Figure 4.5(b) could result from intradomain reactions involving the dangling chains with very high molecular mobility, which would not significantly affect the average mesh size of the domain.

The decrease in $\varXi$ with the curing process could be related to a decrease in the size of the LXD, because the progress of the gelation well beyond the gel point suggests that the HXD is dominant and the volume of the domain is sufficiently large. This conjecture and the behavior of φ_{1+2} indicate the presence of interdomain reactions between the HXDs. The reaction results in a slight but insignificant change in the number of protons both in the HXDs and LXDs; however, the reaction could result in a significant decrease in the size of the LXD in the solvent swollen state.

4.3.4 SANS and WANS

To verify the results obtained using the X-ray scattering technique, complementary structural analysis was performed with fully MeOH-d_4-swollen phenolic resins using a combination of SANS and WANS measurements. The SANS and WANS results are shown in Figure 4.10. The observed neutron scattering results from the same structural features of the solvent-swollen phenolic resins as observed by the X-ray scattering technique; therefore, the following theoretical scattering function based on Equation (4.4) was applied in the curve fitting analyses of the neutron scattering data over the wide q range of 0.08–30 nm^{-1}:

$$I_N(q) = A_{\mathrm{N}}q^{-4} + \frac{I_{\mathrm{SL,N}}(0)}{(1 + \varXi_{\mathrm{N}}^2 q^2)^2} + \frac{I_{\mathrm{OZ,N}}(0)}{1 + \xi_{\mathrm{N}}^2 q^2} + B_{\mathrm{N}} \exp\left[-\frac{(q - q_{0,\mathrm{N}})^2}{2w_{\mathrm{N}}^2}\right] \tag{4.5}$$

$$+ C_{\mathrm{N}} I_{\mathrm{MeOH}-d_4}(q) + I_{\mathrm{inc}},$$

where the definitions of the variables are the same as for Equation (4.4) (the subscript "$_{\mathrm{N}}$" is added to distinguish them from those in Equation (4.4), and I_{incoh} denotes incoherent neutron scattering background, which was approximated to be constant in the investigated q range. The fitting curves are shown by solid lines in Figure 4.10, in which the cures accurately reflect the observed neutron scattering curve. Figure 4.11 shows changes in the obtained fitting parameters $\varXi_{\mathrm{N}}$ and ξ_{N} as a function of curing temperature, which clearly support the X-ray scattering results shown in Figure 4.9.
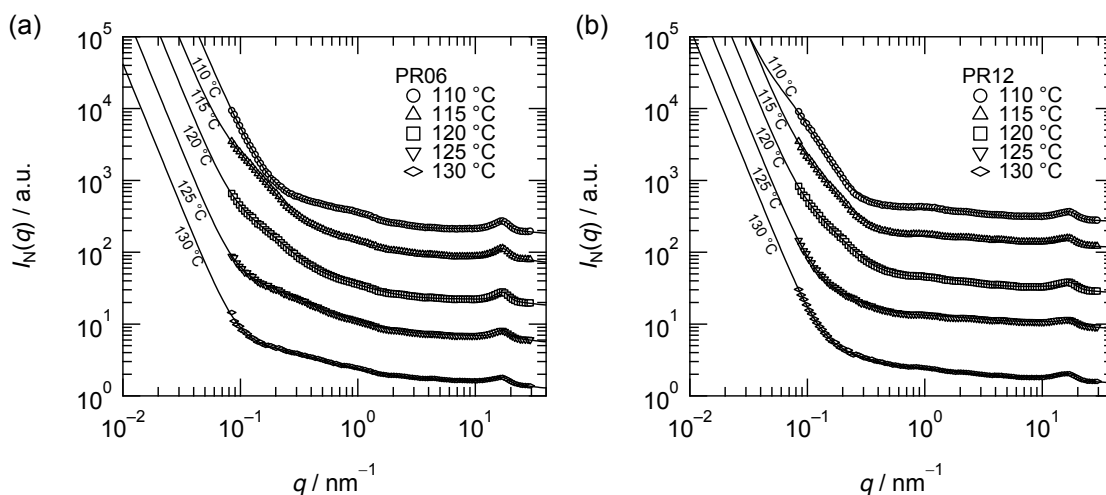
Figure 4.10 Change in SANS and WANS curves as a function of curing temperature: (a) **PR06** and **PR12** in MeOH-d_4. Solid lines are fitting curves using Equation (4.5). The curves are arbitrarily vertically shifted to improve visibility.
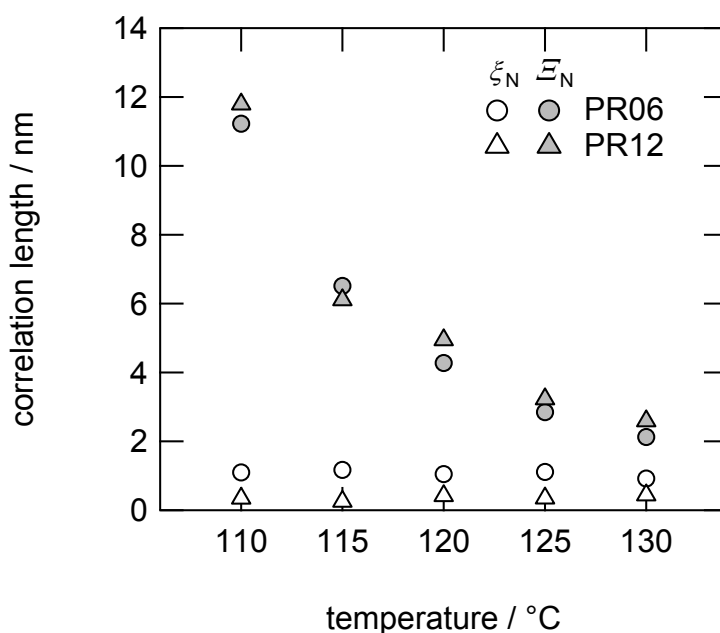

Figure 4.11 Change in the fitting parameters of neutron scattering curves as a function of curing temperature: circles, **PR06**; and triangles, **PR12**.

4.3.5 Network Structure Evolution

Figure 4.12 shows a schematic representation of the network structure evolution mechanism of phenolic resins, highlighting the interdependence of the stoichiometric amount of cross-linker and inhomogeneity in the initial stage of the curing. In the figure, the filled circles, thick circular

outlines, and the spaces between them represent the HXD, the interface region, and the LXD, respectively, whose time constants are $T_{2,1}$, $T_{2,2}$, and $T_{2,3}$, respectively. Lines unconnected at one end represent dangling chains with a higher molecular mobility. The average distance between domain boundaries, which represents the characteristic size or degree of inhomogeneity, and the average mesh size of the LXD correspond to the correlation lengths $\varXi$ and ξ, respectively.
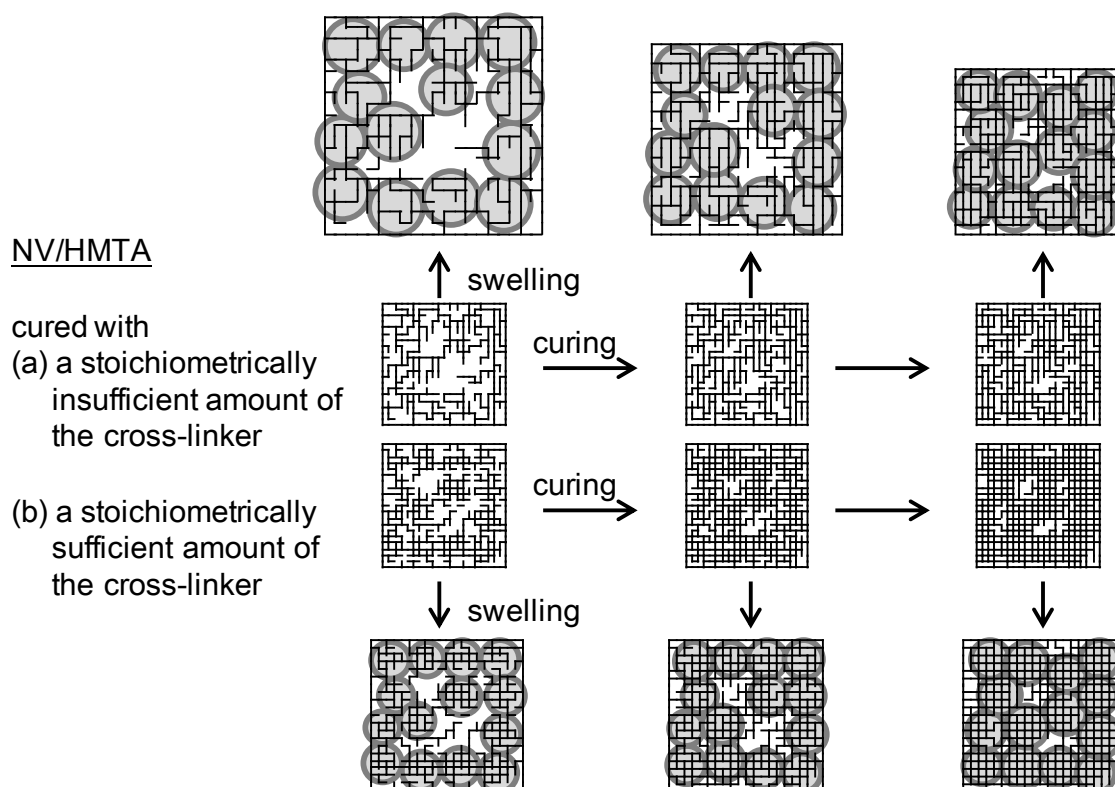

Figure 4.12 Scheme of the network structure evolution mechanism representing the interdependence of the stoichiometric amount of crosslinker and the growth of the inhomogeneity of phenolic resins during the initial stage of the curing: (a) cured with a stoichiometrically insufficient amount of crosslinker, as in the case of **PR06**, and (b) cured with a stoichiometrically sufficient amount of cross-linker, as in the case of **PR12**. The filled circles, thick circular outlines, and the spaces between them represent the high-crosslink density, the interface, and the low-crosslink density regions, respectively, in the swollen state. Lines unconnected at one end represent dangling chains with a higher molecular mobility.

The percolation of the HXDs occurs at 110 °C for both **PR06** and **PR12**, in which the

degree of cross-linking of the percolated domains dominates the degree of swelling of the gel. The HXD of **PR12** has a tightly cross-linked, well-developed network structure from the beginning of the curing process, which results in a constant value of D_{swell} irrespective of the curing temperature. Conversely, **PR06** has a more loosely cross-linked network structure compared with **PR12**, in which the degree of cross-linking in the domain increases via intradomain reactions accompanying a decrease in D_{swell} as curing progresses. The spatial location and size of the percolated domains in the dry state does not change significantly during the initial curing process because of the intradomain reactions being dominant for both HXDs and LXDs, which results in a slight but insignificant increase both in the φ_{1+2} values of **PR06** and **PR12** over the investigated temperature range. Conversely, the minor interdomain reaction at the interface between the HXDs results in a significant decrease in the size of the LXDs in the solvent swollen state, which results in the behavior of φ_{1+2} along with a decrease in Ξ. The intradomain reactions in the LXDs of **PR06** and **PR12** involved reactions with dangling chains with a very high molecular mobility, which does not affect the value of ξ significantly, but results in a steep decrease in $T_{2,3}$ at the beginning of the curing process owing to a decrease in the molecular mobility of the high mobility segments in the domain.

4.4 Conclusions

The cross-link inhomogeneity of phenolic resins at the initial stage of the curing process, well beyond the gel point, in a temperature range of 110–130 °C was successfully elucidated through structural analyses of the network structure evolution mechanism using ^{1}H-pulse NMR spectroscopy and the complementary SAXS/WAXS and SANS/WANS methods in conjunction with a solvent-swelling technique. Two types of phenolic resins **PR06** and **PR12** were prepared with stoichiometrically insufficient and sufficient amounts of cross-linker, respectively, via curing of NV with HMTA. Because of the cross-link inhomogeneity, their network structures comprised three different structures since the beginning of the curing process: HXD, LXD, and the interface region between HXD and LXD. The percolation of HXD occurred at the beginning of the curing. Intradomain reactions inside both HXD and LXD proceeded as the dominant reactions accompanying minor intrerdomain reactions between HXDs, which resulted in no significant change in the spatial location and size of the HXD and LXD. The intradomain reactions inside the LXD involve reactions with dangling chains, which would not significantly affect the average mesh size of the domain. These behaviors of the network structure evolution mechanism at the initial stage of curing are a general feature of phenolic resins that does not

depend on the amount of cross-linker. The difference between the amount of cross-linker in **PR06** and **PR12** was manifested as the difference in the degree of cross-linking in the percolated HXDs, resulting in a difference in the degree of swelling, i.e., the HXD of **PR12** exhibited a tightly cross-linked, well-developed network structure from the beginning of the curing process, whereas, the HXD of **PR06** exhibited a loosely cross-linked network structure, with increasing degree of cross-linking as the curing proceeded.

We believe that this structural analysis method offers new insights for elucidating the inhomogeneity of cross-linked network structures in fully cured phenolic and other thermosetting resins, considering that a detailed clarification on this topic has not been provided in detail more than a century since the invention of the resins.

References

1. J. P. Cohen Addad, In *Physical Properties of Polymeric Gels*, J. P. Cohen Addad, Ed., John Wiley: New York, pp. 39–86, 1996.

2. R. Kimmich, and N. Fatkullin, *Adv. Polym. Sci.*, 2004, **170**, 1–113.

3. A. Asano, *Annu. Rep. NMR Spectrosc.*, 2015, **86**, 1–72.

4. M. Nomoto, Y. Fujikawa, T. Komoto, and T. Yamanobe, *J. Mol. Struct.*, 2010, **976**, 419–426.

5. K. Dušek, *Polym. Gels Networks*, 1996, **4**, 383–404.

6. M. Shibayama, *Macromol. Chem. Phys.*, 1998, **199**, 1–30.

7. M. Shibayama, *Polym. J.*, 2011, **43**, 18–34.

8. M. Shibayama, *Soft Matter*, 2012, **8**, 8030–8038.

9. W. L. Wu, M. Shibayama, S. Roy, H. Kurokawa, L.D. Coyne, S. Nomura, and R. S. Stein, *Macromolecules*, 1990, **23**, 2245–2251.

10. J. Bastide, S. J. Candau, In *Physical Properties of Polymeric Gels*, J. P. Cohen Addad, Ed., John Wiley: New York, 1996, pp. 143–308.

11. H. Masunaga, H. Ogawa, T. Takano, S. Sasaki, S. Goto, T. Tanaka, T. Seike, S. Takahashi, K. Takeshita, N. Nariyama, H. Ohashi, T. Ohata, Y. Furukawa, T. Matsushita, Y. Ishizawa, N. Yagi, M. Takata, H. Kitamura, K. Sakurai, K. Tashiro, A. Takahara, Y. Amemiya, K. Horie, M. Takenaka, T. Kanaya, H. Jinnai, H. Okuda, I. Akiba, I. Takahashi, K. Yamamoto, M. Hikosaka, S. Sakurai, Y. Shinohara, A. Okada, and Y. Sugihara, *Polym. J.*, 2011, **43**, 471–477.

12. A. Takahara, T. Takeda, T. Kanaya, N. Kido, K. Sakurai, H. Masunaga, H. Ogawa, and M.

Takata, *Synchrotron Radiat. News*, 2014, **27**, 19–23.

13. F. Zhang, J. Ilavsky, G. G. Long, J. P. G. Quintana, A. J. Allen, and P. R. Jemian, *Metall. Mater. Trans. A*, 2010, **41A**, 1151–1158.

14. R. J. Roe, *Methods of X-ray and Neutron Scattering in Polymer Science*, Oxford University Press: New York, 2000.

15. S. Takata, J. Suzuki, T. Shinohara, T. Oku, T. Tominaga T, K. Ohishi, H. Iwas, T. Nakatani T, Y. Inamura, T. Ito, K. Suzuya, K. Aizawa, M. Arai, T. Otomo, and M. Sugiyama, *JPS Conf. Proc.*, 2015, **8**, 036020.

16. T. Canal, and N. A. Peppas, *J. Biomed. Mater. Res.*, 1989, **23**, 1183–1193.

17. A. Izumi, T. Nakao, and M. Shibayama, *Soft Matter*, 2013, **9**, 4188–4197.

18. A. Izumi, T. Nakao, and M. Shibayama, *Polymer*, 2015, **59**, 226–233.

19. P. Debye, and A. M. Bueche, *J. Appl. Phys.*, 1949, **20**, 518–525.

20. H. E. Stanley, *Introduction to Phase Transitions and Critical Phenomena*, Oxford University Press: New York, 1971.

Chapter 5

Model Construction and Verification of Crosslinked Phenolic Resins using Molecular Dynamics Simulation with Pseudo-Chemical Reaction

5.1 Introduction

In this chapter, the author proposes a methodology for constructing crosslinked phenolic resins and using MD simulation and pseudo-reactions in order to understand structure–material property relationships. First, suitable parameter sets were investigated with liquid phenol regarding force fields and electrostatic potentials. Then, the construction of crosslinked phenolic resins via novolac resins was attempted using phenol molecules (Figure 5.1(a)) as initial molecules to consider MWDs of resulting polymers and shapes of the MWDs. Different reaction probabilities were introduced according to the *ortho*/*para* positions on phenolic rings to control the ratios of *o–o'*, *o–p'*, and *p–p'* methylene linkages in the reacted resins. These treatments enabled the reproduction of various industrial phenolic resins, such as random novolac and high-*ortho* novolac resins, in addition to highly crosslinked phenolic resins. A conventional crosslinked structure was also constructed from linear novolac chains (Figures 5.1(b) and (c)) with a monodisperse molecular weight (MW) for comparison. The constructed network structure was verified by the unit fraction of phenolic units and methylene linkages, the MWD, the densities, and the scattering functions for various reaction conversions. A structure factor involving atomic configuration was also calculated and compared with the experimental one estimated from the SAXS and WAXS results. Voronoi tessellation analysis was also performed to discuss the occupation volume distribution which is useful technique to evaluate the free volume [1–3]. A full atomic MD simulation was performed with 232,000 and 29,000 atoms. The large-scale MD simulation using 232,000 atoms enabled us to analyze the inhomogeneous crosslinking using the structure factor as well as to improve the precision of the statistical analysis. The methodology used in this study is a powerful and versatile technique for constructing and verifying crosslinked thermosetting resins, and it is not limited to phenolic resins. This investigation is believed to play an important role in understanding the relationships

between crosslinked structures and material properties in thermosetting resins.
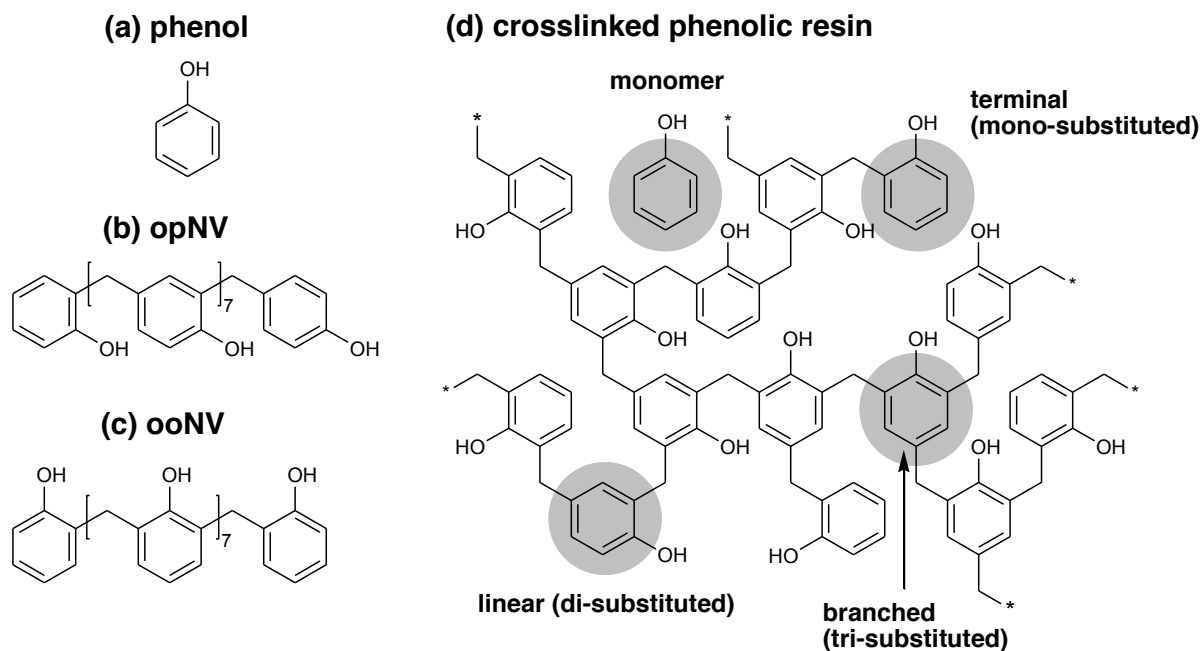

Figure 5.1 Chemical structures of initial molecules used in simulation: (a) phenol, (b) **opNV** (linear chain containing nine phenol rings with *o–p'* methylene linkages), and (c) **ooNV** (linear chain containing nine phenol rings with *o–o'* methylene linkages). (d) Example of crosslinked phenolic resin.

5.2 Method

5.2.1 General

Full atomistic MD simulations were performed for model construction, equilibration, and characterization of material properties in this work. LAMMPS (Sandia National Laboratory, U.S.A.) [4] and J-OCTA ver. 1.8 (JSOL Corp., Japan) were used for all of the MD calculations and the initial molecular modeling, respectively. A combination of general AMBER force field (GAFF) [5] and atomic charges estimated from RHF/6–31G(d,p) calculation was chosen for the potential parameters to perform the MD simulations of phenolic resins in this study. Partial atomic charges were estimated using Gaussian 09 D (Gaussian, Inc., U.S.A.) and a restrained electrostatic potential (RESP) fitting program [6]. The calculations of the Voronoi cell volumes were performed using Voro++ program package [3]. The detailed procedures of the pseudo-reactions used to construct the crosslinked phenolic resins were described later. Large-scale

MD simulations were performed on K Computer system (the RIKEN Advanced Institute for Computational Science (AICS), Japan).

A Nosé–Hoover thermostat and a Parrinello–Rahman barostat were used to control the temperature and the pressure with damping parameters of 200 fs for the thermostat and 500 fs for the barostat [7–9]. The Lennard-Jones and Coulombic interactions were computed with a cutoff length of 11 Å and, in the case of GAFF, a weighting factor of 0.5 was applied for 1–4 interactions. The Particle–Particle Particle–Mesh solver was used to compute the long-range Coulombic interactions with a desired relative error in the forces within an accuracy of 10^{-5} [10].

5.2.2 Force field

In GAFF, the bonding interaction consists of four terms, namely, a two-body bond-stretching potential (U_{bond}), a three-body angle-bending potential, (U_{angle}) and a four-body torsional-angle potential ($U_{torsion}$). The nonbonding interaction consists of two terms, namely, the van der Waals (vdW) interaction potential (U_{vdW}) and an electrostatic (Coulombic) interaction potential ($U_{coulomb}$). The total potential is given by

$$U_{total} = U_{bond} + U_{angle} + U_{torsion} + U_{vdW} + U_{coulomb}, \tag{5.1}$$

where the functional forms of each potential are described by.

$$U_{bond} = \sum_{bonds} \frac{1}{2} k_b (l - l_0)^2, \tag{5.2}$$

$$U_{angle} = \sum_{angles} \frac{k_a}{2} (\theta - \theta_0)^2, \tag{5.3}$$

$$U_{torsion} = \sum_{torsions} \sum_n \frac{k_n}{2} [1 + \cos(n\phi - \gamma)], \tag{5.4}$$

$$U_{vdW} = \sum_{i<j} \left(\frac{A_{ij}}{r_{ij}^{12}} - \frac{B_{ij}}{r_{ij}^6} \right), \tag{5.5}$$

$$U_{coulomb} = \sum_{i<j} \frac{q_i q_j}{\epsilon r_{ij}}, \tag{5.6}$$

l, θ, ϕ are the bond distance, angle and dihedral angle, respectively. k_b, k_a and k_n are the coefficients of each functional. Subscript "0" means the equilibrium value. Standard parameter sets for organic molecules were applied to the force field parameters for the bonding interaction

and van der Waals interaction. The Lennard-Jones 6–12 type potential was used to describe van der Waals interactions. r_{ij} in U_{vdW} and U_{coulomb} is the distance between atom i and atom j. A_{ij} and B_{ij} are the coefficients related to the equilibrium distance and the depth of potential well. q and ϵ in U_{coulomb} are partial atomic charge and the dielectric constant.

The material properties of crosslinked thermosetting resins are strongly affected by force field parameters and the initial molecular configuration [11]. Therefore, it is necessary to understand the effect of these parameters to obtain reliable structural properties. First, we investigated the dependencies of the force field and atomistic charges on the density for unreacted liquid phenol. The density of liquid phenol was calculated at various temperatures to check the accuracy of the force field and atomic charges. Experimental values of the density of liquid phenol are reported in ref. 12 and 13 for the temperature range from 300 K to 400 K and are represented as a solid line in Figure 5.2. The structures of liquid phenols were obtained by the following procedures. (i) First, 2,000 phenol molecules consisting of 26,000 atoms were randomly placed in an isotropic simulation box whose cell length was adjusted to achieve a density of 0.1 g/cm³. (ii) The phenols were stirred for 100 ps in the NVT ensemble at 500 K and for 1 ns in the NPT ensemble at a pressure of 0.1 MPa and a temperature of 500 K. Condensed phenol molecules were obtained throughout this NPT ensemble. (iii) These structures were relaxed at a constant temperature in the range from 280 K to 500 K for 1 ns in the NPT ensemble. The value of the density at each temperature was calculated as an average from the last 100 ps computation. A standard velocity Verlet integrator was used with a time step Δt of 1.0 fs in procedures (i)–(iii).

The computed densities of liquid phenol are plotted in Figure 5.2 for a combination of force fields and electrostatic potentials. DREIDING force field [14] and atomistic charges of B3LYP/6-31G(d,p) were also tried. The reported experimental values are also shown as a solid line [12]. Here the following experimental equation was applied for the density ρ of liquid phenol as $\rho = A + BT + CT^2$, where A, B, and C are 1.28717, -6.01811×10^{-4}, and -4.09922×10^{-7}, respectively, in the temperature range from 298.00 K to 423.15 K. GAFF+B3LYP/6-31G(d,p) showed higher values for the density that were closer to the experimental results than those from DREIDING+B3LYP/6-31G(d,p). Here a combination of DREIDING and B3LYP/6-31G(d,p) was adopted for the crosslinked phenolic resins in ref. 15. This result indicates the validity of using GAFF to express the density of liquid phenol. In addition, the optimal electrostatic parameters were investigated using the results from GAFF+B3LYP/6-31G(d,p) and GAFF+RHF/6-31G(d,p). Combining GAFF and RHF/6-

31G(d,p) resulted in slightly higher density values than B3LYP/6-31G(d,p) yielded and gave good agreement with the experimental values within 10% in this temperature ranges. This result validates the recommendation that a parameter set of GAFF should be used with electrostatic potentials estimated from Hartree–Fock theory for most organic molecules [5]. Coulombic interactions are assumed to play important roles in the material properties of phenolic resins. Arab *et al.* also investigated the dependences of force fields on the material properties of crosslinked polymers using atomistic MD simulation [16]. They modeled a crosslinked network structure from the diglycidyl ether of bisphenol-A and diethylene triamine and estimated the values of the density and elastic constants with various force fields, including the DREIDING force field. The values they obtained using the DREIDING force field were smaller than the experimental values. Such a tendency is believed to be the result of underestimating nonbonding interactions, especially hydrogen bonding, in DREIDING. According to the above results, a combination of GAFF and RHF/6-31G(d,p) was chosen for the potential parameters to perform the MD simulations of phenolic resins in this study.
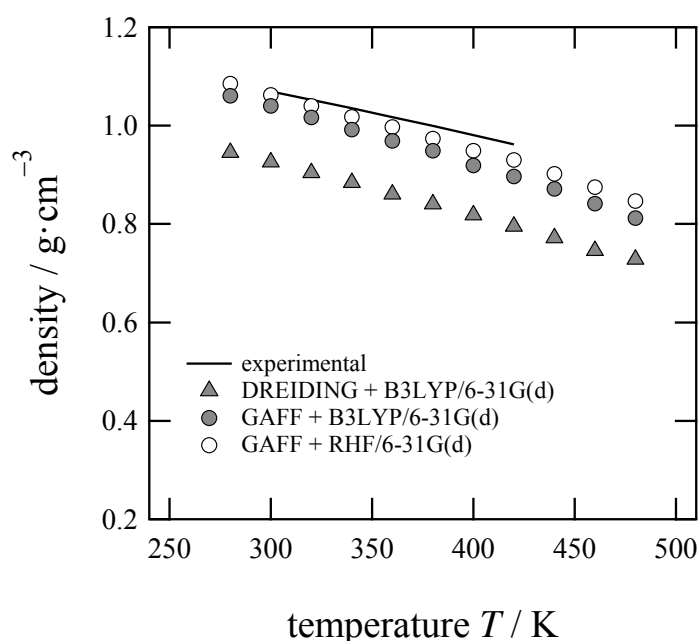

Figure 5.2 Densities of liquid phenol calculated from MD simulation and experimental values as a function of temperature.

5.2.3 Modeling of Crosslinked Structures

The pseudo-reactions were employed to construct a crosslinked phenolic resin. This crosslinking process was performed during MD simulation using an originally customized

simulation code based on *fix/bond create* implemented in LAMMPS. Phenol was used as an initial molecule, and crosslinking procedures were applied to the phenol used in this work. As shown in Figure 5.3, a crosslinking reaction was allowed between a crosslinker atom C_X and two reactive sites belonging to two other phenolic rings. Here the reactive sites are carbon atoms at two *ortho* positions and one *para* position on a phenolic ring. The crosslinking reaction was applied when the distances between C_X and the reactive sites were within a given cutoff distance r_{cutoff}. If there were many candidate atoms larger than two pairs, the nearest pairs were chosen, and their types were checked to determine whether their combinations were *o–o'*, *o–p'*, or *p–p'*. A random number between 0 and 1 was then generated, and the crosslinking reaction was accepted when this number was smaller than the given reaction probability ($p_{o–o'}$, $p_{o–p'}$, and $p_{p–p'}$), according to their combinations. Here the reaction probabilities, $p_{o–o'}$, $p_{o–p'}$, and $p_{p–p'}$, were introduced to control the fractions of the methylene bridges of *o–o'*, *o–p'*, and *p–p'*, which are required to reproduce an experimentally estimated structure. For example, the fractions of methylene linkages are known to be approximately *o–o'*: *o–p'*: *p–p'* = 0.25: 0.50: 0.25 for random novolac phenolic resins [17]. These values indicate that the reactivities of *ortho* and *para* sites are not equivalent and that the *para* position has a higher reactivity than the *ortho* position has in random novolac resins. The reaction probability at the *para* carbon has been reported as being 2.4 times higher than that at the *ortho* carbon in the standard random novolac system [18]. Some parameters concerning crosslinking reactions were tested so that the fractions of the methylene bridges would be close to the experimental values. When the reaction was accepted, the molecular topology and corresponding force field parameters were updated. Two bonds were created between the reactive sites via the crosslinker atom. The C–H bonds of reactive sites on the phenolic rings were deleted, and new C–H bonds were created between the crosslinker and the hydrogen atom. The bond angle and torsion angle potentials were also updated. Atom types of unreacted aromatic carbon and C_X were changed into normal aromatic carbon and reacted alkyl carbon, respectively. Finally, the charges were updated for every atom of the two phenol rings and methylene participating in the reaction to values that were calculated using *ab initio* calculation and RESP fitting in advance.

In this dissertation, the conversion α is defined as the degree of crosslinking given by

$$\alpha = \frac{2N_{CH_2}}{3N_{PhOH}},$$

(5.7)

where N_{CH2} and N_{PhOH} are the number of reacted methylene units and the number of total phenolic rings in the system, respectively. The value α corresponds to a branching coefficient

of a three-functional monomer system in Stockmayer theory [19]. Yamagishi *et al.* also adopted this definition to perform a Monte Carlo simulation with a cubic lattice to investigate the gelation behavior of phenolic resin using a percolation model [20,21]. It should be noted that such a definition is a conversion based on the functionalities of phenol. A structure with $0 \leq \alpha \leq 0.85$ was considered as the subject of the model construction and analysis in this study.
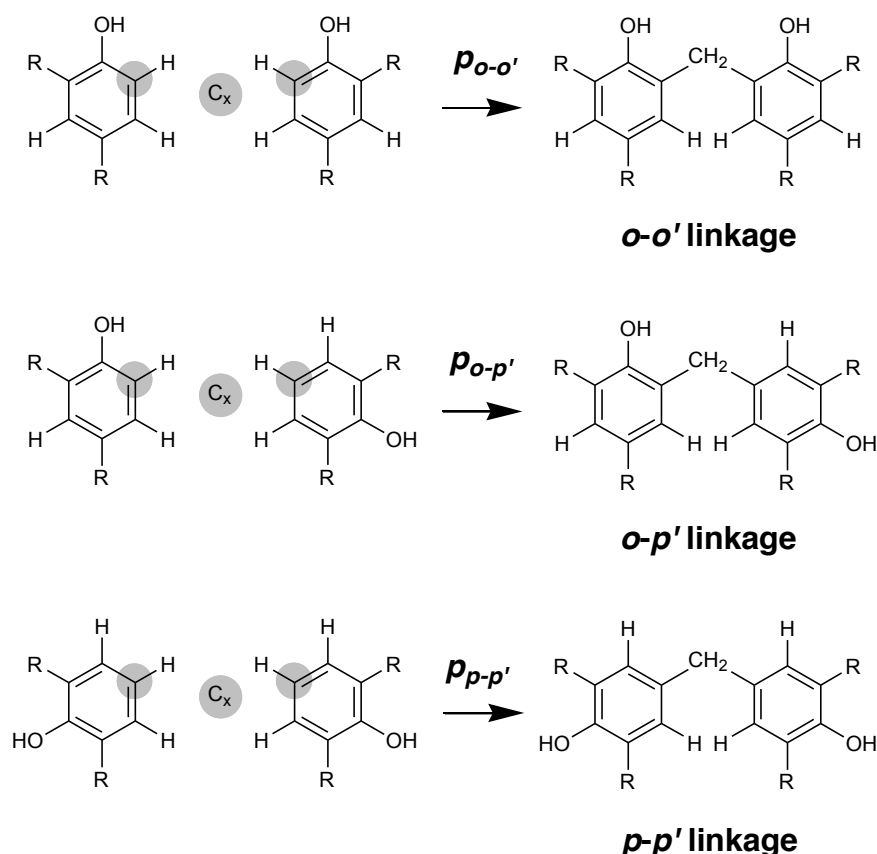

Figure 5.3   Pseudo-crosslinking reaction between two phenolic units used in our computational model. R represents a hydrogen atom (H) or methylene linkage (CH_2) connected to other phenolic rings.

Crosslinked structures were obtained by the following procedures: (i) crosslinker atoms C_X were randomly placed in the amorphous structure of liquid phenols. (ii) These structures were relaxed at a constant temperature of 450 K for 100 ps in the NPT ensemble with an isotropic cell. The crosslinking reaction was permitted in (i) and (ii). (iii) The crosslinking reaction started with a standard NVT ensemble MD simulation at 450 K. A time step Δt of 0.01 fs was applied to avoid an integration error resulting from a large force in high-frequency topology updating. Δt was changed to 0.02 fs, 0.05 fs, 0.1 fs, and 0.5 fs as the conversion

increased. The crosslinking reaction was attempted every 1 fs with given reaction probabilities, in which a generated random number was used to judge whether the reaction was accepted or rejected. Simultaneous reactions at multiple reactive points were allowed in the same way as the conventional reaction model [15]. (iv) After reaching a desired conversion, residual unreacted crosslinker atoms were removed, and the obtained structure was then relaxed at 700 K for 1–2 ns in the NPT ensemble with an anisotropic simulation box by permitting an anisotropic cell deformation to be a rectangular cuboid cell. In addition, a further relaxation process was performed at 300 K for 2–4 ns in the NPT ensemble. A time step Δt of 1.0 fs was applied. In procedures (i)–(iv), a standard velocity Verlet integrator was used.

The parameters used in the crosslinking reaction are listed in Table 1. Each simulation run is named according to system size (L or S), initial molecules in reaction (R1 or R9), and *orhto/para* reactivity (ra or ho). r_{cutoff} was fixed at 2.3 Å for all of the simulations, because a longer reaction distance raises a crosslinking reaction more quickly; on the other hand, unrealistic cyclic structures tend to be produced, such as small-membered calixarenes, which rarely exist in most novolac resins before gelation. The reaction probabilities were decided such that $p_{o-o'} : p_{o-p'} : p_{p-p'} = p_0 : rp_0 : r^2 p_0$. Here a small value of p_0 was chosen to avoid rapid reactions that would cause errors in the MD simulation and to maintain a relaxed structure. r represents the ratio of the reaction probability at the *para* position to that at the *ortho* position. All of the simulation parameters were retained throughout each crosslinking procedure. In **L-R1-ra** and **S-R1-ra**, the crosslinking reactions corresponded to a standard random novolac and cured resin via random novolac resins. Similarly, **L-R1-ho** and **S-R1-ho** corresponded to a high-*ortho* novolac reaction system. $r = 8$ was used for random novolac resins (**L-R1-ra** and **S-R1-ra**), and $r = 0.25$ for high-*ortho* novolac resins (**L-R1-ho** and **S-R1-ho**); p_0 and r were determined based on the results of prior investigations so as to allow the desired fractions of methylene linkages in reacted products to fit experimental results.

The number of atoms used in this simulation was decided based on the simulated cell length L, so that the minimum of the q-vector in the scattering function was 1 nm^{-1} for **L-R1-ra** and **L-R1-ho** and 2 nm^{-1} for **S-R1-ra** and **S-R1-ho**. The density of the final product was assumed to be 1.2 g/cm^3. Details about the q-vector and the scattering function will be given later. The size dependency on the structure and material properties was analyzed by performing comparisons between **L-R1-ra** and **S-R1-ra** and **L-R1-ho** and **S-R1-ho**. To compare the modeling method in this study with a conventional model, crosslinking reactions were also adopted for monodisperse novolac resins: opNV (**S-R9-ra**) and ooNV (**S-R9-ho**). Here opNV

and ooNV represent linear novolac chains with nine phenolic rings having all *o–p'* methylene linkages and *o–o'* linkages. The construction and estimation of material properties for crosslinked ooNV were implemented in previous study [15]. Five different structures were constructed from different initial configurations **S-R1-ra**, **S-R1-ho**, **S-R9-ra**, and **S-R9-ho** and were used for structure and property characterization.

5.2.4 Structural Analysis

Changes in the unit fractions of the phenolic units were evaluated depending on the degree of crosslinking. The phenolic units were classified as *monomer*, *terminal*, *linear*, and *branched*, which correspond to unreacted, mono-substituted, di-substituted, and tri-substituted phenols, respectively. Although these fractions can be obtained using high-resolution liquid and solid ^{13}C-NMR experiments, there have been few systematic studies due to the difficulties associated with the measurements and analyses [22–27]. These can also be estimated from numerical calculations using kinetic equations, as demonstrated in ref. 28. In this work, Aranguren's rate equations were solved and their results were compared to those of our MD simulation results. A set of 14 differential equations was solved by numerical integration with a time step of 0.0001 using a self-written C program and a fourth order Runge–Kutta algorithm. The initial molar ratio of formaldehyde to phenol, $[CH_2O]_0/[PhOH]_0$, was set to 1.5 similarly our MD simulation, and rate constant parameters were given as written in ref. 18.

The unit fractions of the methylene linkages were also evaluated and classified as one of three types depending on the types of carbons on the connected two phenols: *ortho–ortho'*, *ortho–para'*, or *para–para'*. Experimentally, the fractions can be determined using ^{13}C-NMR by analysis of methylene carbon atoms observed in the range from 45 ppm to 25 ppm in the ^{13}C-NMR spectrum. The MWD is one of the most important parameters in characterizing a polymeric material. Changes in the number- and weight-average molecular weights (M_n and M_w, respectively) and distribution function were calculated by analyzing the molecular topologies of the crosslinked phenolic resins before the gel point, depending on the reaction conversion. The gel point was determined based on percolation theory, in which the largest cluster was spanned over the simulation box along all directions [21].

5.2.5 Voronoi Analysis

Voronoi tessellation was performed to the obtained network structure to quantify the volumes per phenolic units [1–3]. All phenolic units were classified to four types (*monomer*, *terminal*, *linear*, and *branched*) as described in 5.2.3, and were represented as beads whose coordinates equal to center-of-mass on each phenolic unit. The Voronoi cell volume was computed for all beads with in simulation box for and their volume distributions were analyzed for each phenolic types. Atoms belonging to methylene linkages (CH_2) were not counted from cell volume calculation. This calculation was adopted for the well equilibrated structure at 300 K with various conversions after gelation.

5.2.6 Scattering Function

The statistical configuration of atoms in each crosslinked structure was characterized using a scattering function or static structure factor $S(q)$ [29]. The computed structure factor $S(q)$ can be obtained from an atomistic configuration followed by a Faber–Ziman definition [30]. $S(q)$ for a multi-component system is given as a Fourier transformation of the partial radial distribution function $g_{\alpha\beta}(r)$, as follows. At first, $g_{\alpha\beta}(r)$ for $\alpha \neq \beta$ is given by:

$$g_{\alpha\beta}(\mathbf{r}) = \frac{N}{\rho N_\alpha N_\beta} \sum_{j=1}^{N_\alpha} \sum_{k=1}^{N_\beta} \langle \delta(\mathbf{r} - \mathbf{r}_{jk}) \rangle, \tag{5.8}$$

and for $\alpha = \beta$,

$$g_{\alpha\alpha}(\mathbf{r}) = \frac{N}{\rho N_\alpha^2} \sum_{j=1}^{N_\alpha} \sum_{k \neq j}^{N_\alpha} \langle \delta(\mathbf{r} - \mathbf{r}_{jk}) \rangle, \tag{5.9}$$

where $\delta(\mathbf{r})$ is the Dirac delta function, and $\mathbf{r}_{jk} = \mathbf{r}_j - \mathbf{r}_k$ represents a displacement vector between two atoms, j and k. α and β denote atom indices representing C, H, or O atoms. N_α and N_β represent the numbers of atoms α and β in the system, respectively. N and ρ denote the total number and number density of all of the atoms, respectively, and $<\ldots>$ denotes a spatial average taken over the simulation box. Similarly, the partial structure factor $S_{\alpha\beta}(q)$ is defined as,

$$S_{\alpha\beta}(\mathbf{q}) = \frac{1 + \delta_{\alpha\beta}}{2N} \sum_{j=1}^{N_\alpha} \sum_{k=1}^{N_\beta} \langle e^{-i\mathbf{q}\cdot\mathbf{r}_{jk}} \rangle = 1 + \rho \int [g_{\alpha\beta}(\mathbf{r}) - 1] e^{-i\mathbf{q}\cdot\mathbf{r}} d\mathbf{r}, \tag{5.10}$$

where $\mathbf{q}$ denotes the magnitude of the scattering vector. In the case of structurally isotropic materials, Equation (5.10) can be written simply as

$$S_{\alpha\beta}(q) = 1 + \rho \int_0^\infty [g_{\alpha\beta}(\mathbf{r}) - 1] \frac{\sin qr}{qr} 4\pi r^2 \mathrm{d}r. \tag{5.11}$$

Finally, the structure factor is given by weighting the X-ray atomic form factor $f(q)$ as

$$S(q) = \frac{\sum_\alpha \sum_\beta c_\alpha c_\alpha f_\alpha(q) f_\beta(q) S_{\alpha\beta}(q)}{\sum_\alpha \sum_\beta c_\alpha c_\alpha f_\alpha(q) f_\beta(q)}. \tag{5.12}$$

Here c_i and $f_i(q)$ denote the molar fractions of the i-th component and the atomic form factor, respectively. In neutron scattering, $f_i(q)$ is replaced by the scattering length b_i. In this calculation, the q range is determined by the length of the periodic boundary cell L as $q_{min} = 2\pi/(L/2)$. Therefore, $q_{min} = 1$ nm^{-1} was used for **L-R1-ra** and **L-R1-ho**, and $q_{min} = 2$ nm^{-1} was used for **S-R1-ra**, **S-R1-ho**, **S-R9-ra**, and **S-R9-ho**. The calculated $S(q)$ was compared with the experimental results obtained from X-ray scattering for reacted phenolic resins at room temperature.

5.2.7   Experimental

Random novolac-type phenolic resins and cured resins were used for structural verification. PR-50716 (a random-type novolac resin; **NV-1**), with M_w and M_n of 7170 g/mol and 910 g/mol, respectively, was provided by Sumitomo Bakelite Co., Ltd. (Tokyo, Japan). The MWD and chemical structure of **NV-1** were well investigated and summarized by Maji *et al.* using GPC and ^{13}C-NMR [31]. Hexamethylenetetramine (HMTA) was purchased from Chang Chung Petrochemical Co., Ltd (Taipei, Taiwan). A highly crosslinked phenolic resin (**NV-2**) was prepared from **NV-1** and HMTA as a curing agent by compression molding using a compression-molding machine (Shinto Metal Industries Corp., Osaka, Japan). Granulated **NV-1** and HMTA were placed in a molding die and molded at 175°C for 3 min under an effective pressure of 100 MPa, followed by post-curing at 180°C for 6 h and 220°C for 3 h under atmospheric pressure. The bulk density was 1.25 g/cm^3 for both **NV-1** and **NV-2**, as measured with pycnometers using distilled water at room temperature.

SAXS experiments over the q range 0.1–5 nm^{-1} were performed on the BL03XU beamline (Frontier Softmaterial Beamline (FSBL)) at SPring-8, which is located in Sayo, Hyogo, Japan [32,33]. A monochromated X-ray beam with a wavelength of 1.0 Å was used to irradiate the samples at room temperature, and the scattered X-rays were counted at a sample-to-detector distance of 2.0 m. The scattered X-rays were counted using an imaging plate system (R-AXIS VII, Rigaku Corporation, Tokyo, Japan) with 3000 × 3000 pixel arrays and a pixel size of 0.1 mm/pixel. WAXS experiments over the q range from 4 nm^{-1} to 60 nm^{-1} were

performed on the BL08B2 beamline (Hyogo-prefectural beamline) at SPring-8. A monochromated X-ray beam with a wavelength of 0.826 Å was used to irradiate the samples at room temperature, and the scattered X-rays were counted at a sample-to-detector distance of 0.05 m. The scattered X-rays were counted using a flat-panel detector system (C9732DK-11, Hamamatsu Photonics K. K., Japan) with 2368 × 2376 pixel arrays and a pixel size of 0.050 mm/pixel. $S(q)$ was obtained from the SAXS and WAXS profile $I(q)$ using the following equation:

$$S(q) = 1 + \frac{I(q) - N\sum_a c_\alpha [f_\alpha(q)]^2}{N[\sum_\alpha f_\alpha(q)]^2}.$$ (5.13)

Here $I(q)$ is the scattering function corrected for absorption, polarization, and background.

5.3 Results and Discussion

5.3.1   Crosslinking Procedure

The conversion curves of runs **L-R1-ra**, **L-R1-ho**, **S-R1-ra**, and **S-R-ho** during crosslinking are shown in Figure 5.4. The solid lines following **L-R1-ra** and **S-R1-ra** correspond to curves estimated from the kinetic rate equations for random novolac resins with a scaling factor of time. Although there are differences between the times required to reach saturated conversion, these shapes are roughly in good agreement. The coincidence of the curve shapes in the MD and kinetics results indicates that the pseudo-reaction used in this MD simulation is a type of stochastic process similar to the experimental one. Therefore, the molecular configuration constructed in this procedure can be evaluated using statistical analysis with gelation theory or a cascade process based on a stochastic process. The differences between runs **L-R1-ra** and **S-R1-ra** and **L-R1-ho** and **S-R1-ho** indicate a system-size dependence in the reaction. This dependence of the reaction speed on the constructed structure will be discussed later.
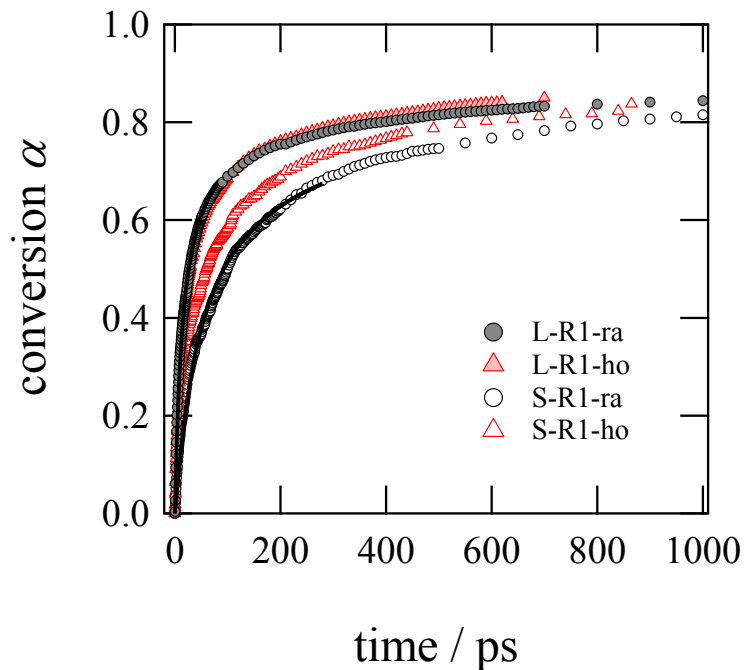
Figure 5.4 Conversion curves of runs **L-R1-ra**, **L-R1-ho**, **S-R1-ra**, and **S-R1-ho** during crosslinking reactions.

5.3.2 Gelation Behavior

The changes in the weight fraction of the largest cluster w_f are shown in Figure 5.5 for **L-R1-ra** and **S-R1-ra** as functions of α. The value of w_f denotes the gel fraction after the gelation point. These two curves sharply increase at $\alpha = 0.57$ and almost overlap after this conversion. Three-dimensional structural models of **L-R1-ra** are shown in Figure 5.6 for various conversions. The growth of the largest cluster in Figure 5.6 clearly indicates that the gel network is formed by an intramolecular reaction between large molecules. Obviously, a conversion of $\alpha = 0.57$ indicates a gel point, for which a percolating cluster appears in the simulation box. Such a spanning cluster is also observable at $\alpha = 0.57$ in **S-R1-ra**. These results show that the system size is independent of the reaction behavior when the number of atoms is larger than 29,000. The shape of the simulation box remains almost cubic for relaxed structures after gelation. This result indicates no deviations in the atomic configurations, molecular orientations, velocities, or interatomic forces during the reaction.
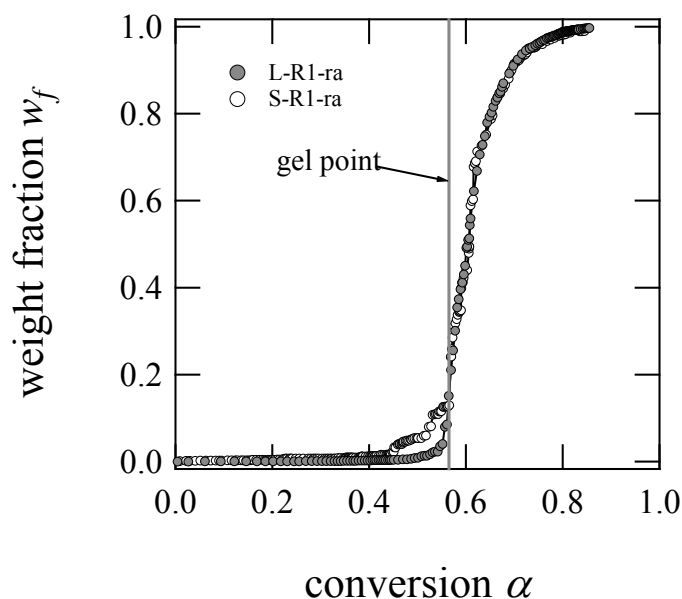
71

Figure 5.5 Weight fraction of the largest cluster in the system w_f as a function of conversion for **L-R1-ra** and **S-R1-ra**.
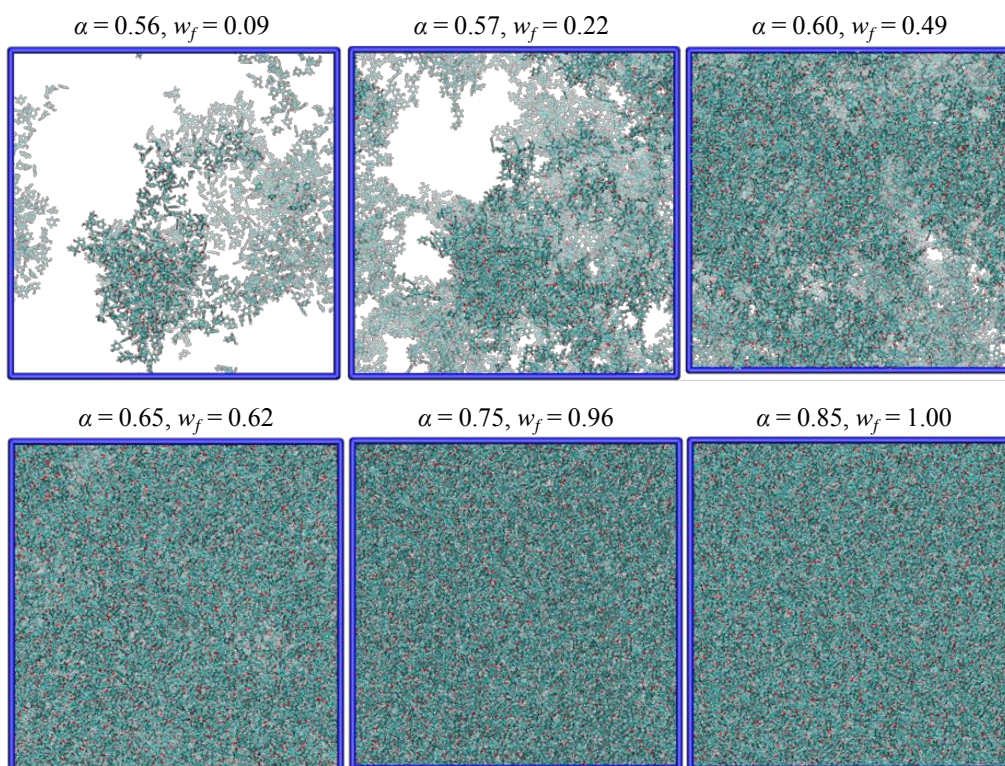

Figure 5.6 Three-dimensional structural model during the reaction process for **L-R1-ra** with various conversions, α: just before gelation ($\alpha = 0.56$), just after gelation ($\alpha = 0.57$), and loosely and highly crosslinked networks ($\alpha = 0.60, 0.65, 0.75$, and 0.85). Only the largest cluster in the system is expressed and the remainder are not displayed.

5.3.3　Chemical Structures of Phenolic Resins

Figure 5.7(a) shows the changes in chemical species on the phenolic units for runs **L-R1-ra** and **S-R1-ra** as a function of the conversion. A comparison with **L-R1-ho** and **S-R1-ho** is shown in Figure 5.7(b). No size dependence is observable in the unit fractions of either the random (**L-R1-ra** and **S-R1-ra**) or the high-*ortho* (**L-R1-ho** and **S-R1-ho**) systems. The curves of the unit fractions in the high-*ortho* system (Figure 5.7(b)) are similar to those of the random novolac systems (Figure 5.7(a)). This agreement was also indicated in an experimental study using ^{13}C-NMR by Nomoto *et al*. [24]. The MD results are consistent with the experimental results, in which the branching degree of the high-*ortho* novolac resins is similar to that of the random novolac resins when compared at the same MW.
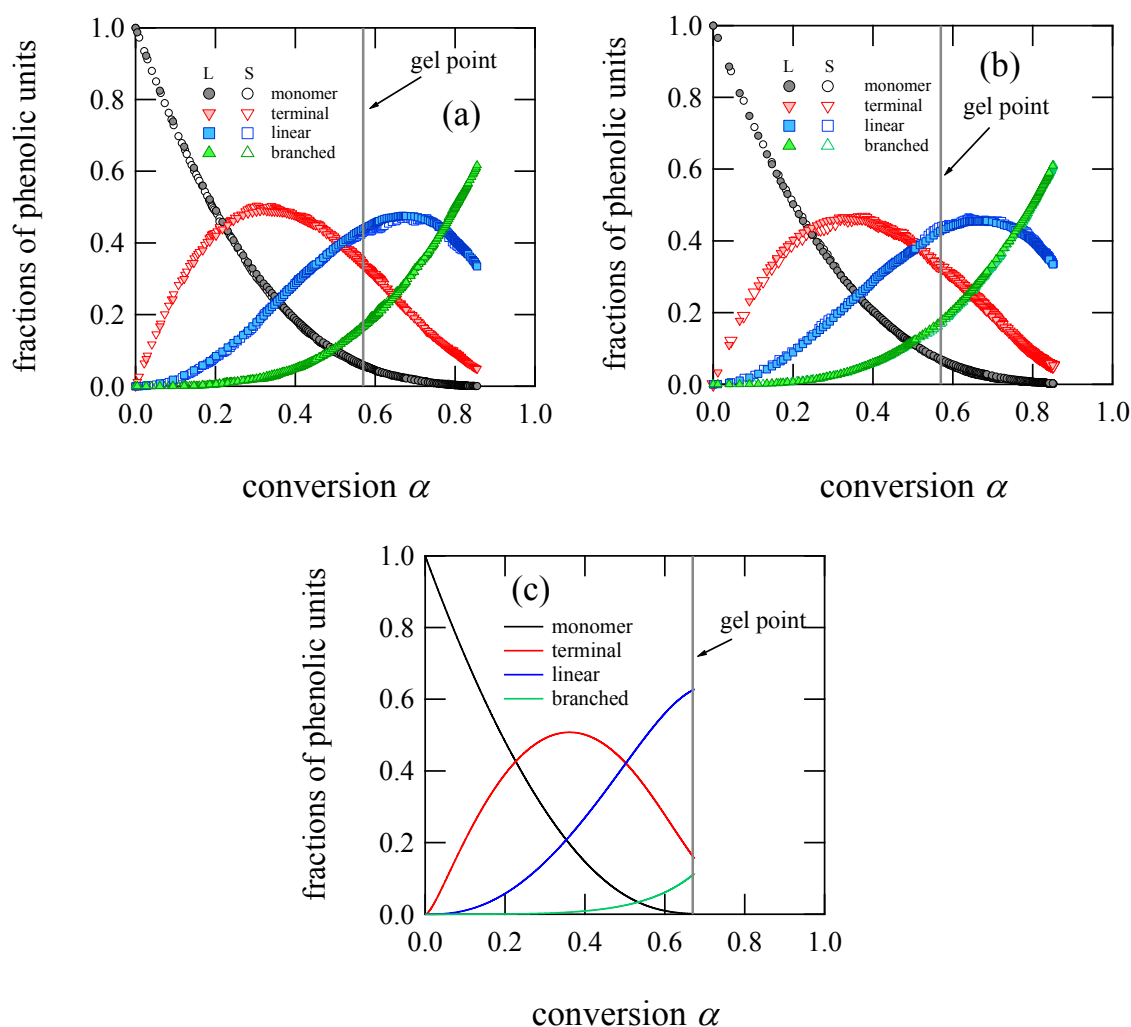

Figure 5.7　Molar fractions of phenolic units as a function of crosslinking conversion in (a) **L-R1-ra** and **S-R1-ra**, (b) **L-R1-ho** and **S-R1-ho**, and (c) Aranguren's kinetic model.

Estimated curves from Aranguren's kinetic equations [18] are also shown in Figure 5.7(c), which corresponds to a random novolac system (**L-R1-ra** and **S-R1-ra**). The fractions of phenolic units from the pseudo-reaction are consistent with the kinetic model and experimental results [17,22,23]. The gel point α_c estimated from the kinetic model ($\alpha_c = 0.64$), is relatively high compared with that of MD ($\alpha_c = 0.57$). As described in ref. 28, it is well known that the gelation conversion depends on the initial molar ratios of phenol and formaldehyde ($[CH_2O]_0/[PhOH]_0$). In previous research, a gel point was found for $N_{CH2}/N_{PhOH} = 0.73$ ($\alpha_c = 0.49$) in the case of $[CH_2O]_0/[PhOH]_0 = 1.5$ [28]. It is assumed that this difference mainly originates from the assumption of constant reactivity irrespective of conversion in the kinetic model. The gel point obtained from our computational study is in the range of generally reported values, although a reaction model with a pseudo-reaction cannot completely simulate an experimental situation. An overestimate of α_c, rather than the Flory–Stockmayer model ($\alpha_c = 0.50$), suggests an intramolecular reaction and substitution effect, including non-equivalence in the reactivity of the three functional points on phenol, structural anisotropy of the phenol rings and changes in the mobilities of the phenolic rings followed by methylene linkages. To understand these effects on the critical behavior in detail, an extended cascade theory that includes these factors is required [34,35].

Figure 5.8 shows the unit fractions of the methylene linkages per all reacted ones as a function of the crosslinking conversion. No system size dependence is evident for either system, as in the preceding phenolic units in Figure 5.7. The ratios of the unit fractions are consistent with the experimental values of unit fractions, *o–o': o–p': p–p' =* 0.25: 0.50: 0.25 for the random novolac resins and 0.58: 0.40: 0.02 for the high-*ortho* novolac resins at an approximate conversion of $\alpha = 0.50$–0.60 [17,31]. Dependence of the unit fractions of the random novolac resins on the reaction conversion, as shown in Figure 5.8(a) was also suggested by an experimental study using ^{13}C-NMR by Yamagishi *et al.* [23].
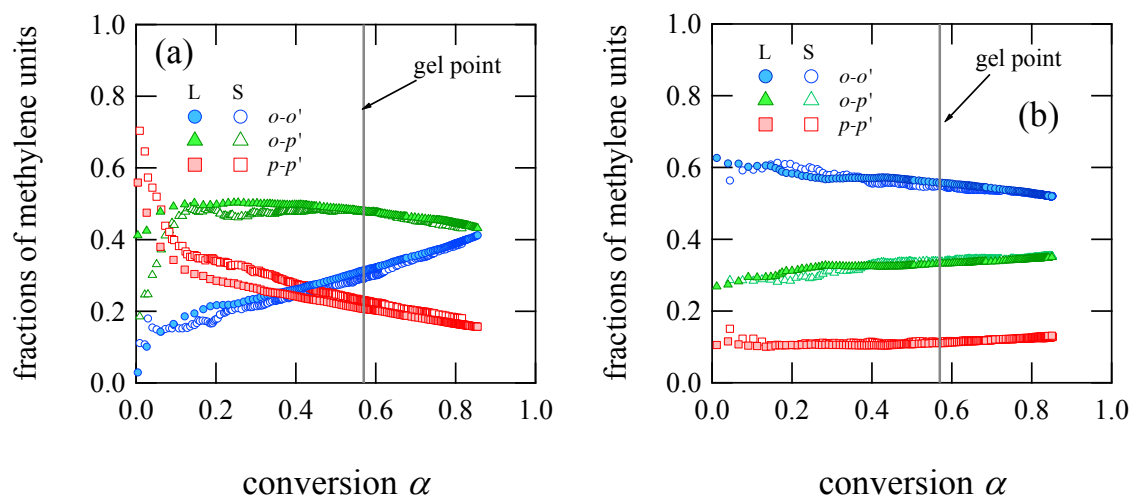
Figure 5.8 Molar fractions of methylene linkages per total reacted ones as a function of crosslinking conversion in (a) **L-R1-ra** and **S-R1-ra**, and (b) **L-R1-ho** and **S-R1-ho**.

As mentioned above, the MWD in the oligomeric state plays an important role in the curing behavior as well as the M_w and M_n values. Figure 5.9(a) shows the MWDs for several reaction conversions calculated from the computational model in **L-R1-ra**. Here each continuous MWD function was estimated from the molar fraction of all of the molecules in the system, using a log-normal Gaussian function [35]. The shapes of the calculated MWDs are obviously similar to those of the experimental MWDs in typical novolac resins. Figure 5.9(b) shows changes in M_n, M_w and MWs of the largest and second-largest molecules in the system as a function of conversion. Rapid increases in the M_w values and the MWs of the largest clusters and decreases in the M_w values and the MWs of the second-largest clusters are evident between before and after the gel point. The conversion when the MW of the second-largest molecule drops is almost equal to the gel point estimated from percolation, as shown in Figure 5.6 [36]. These results also indicate the existence of huge molecules near the gel point, whose MW is 10 times higher than M_w. An explosive increase in the MWs of large clusters indicates a selective intermolecular reaction between large molecules, as shown in DLS experiments [37,38]. In our computational model, a maximum limit on the MW before gelation was determined by the system size, including the number of atoms. A molecule with a MW of about 10^5 g/mol can be observed near the gel point for **L-R1-ra** and **L-R1-ho**. Here molecules with MW = 10^5 g/mol have also been observed experimentally [28,37]. On the other hand, the largest molecules turn into gel clusters before their MWs reach 10^5 g/mol in **S-R1-ra** and **S-R1-ho**. The number of atoms (29,000) used in **S-R1-ra** and **S-R1-ho** is not sufficient to express a MWD

near the gel point. In other words, a large-scale MD simulation, such as in **L-R1-ra** and **L-R1-ho**, is necessary to analyze the effects of critical clusters on the initial structural inhomogeneity just after the gel point. These results demonstrate that the chemical structures and MWs of reacted phenolic resins can be controlled by reaction parameters and reaction conversion in this MD simulation. This reaction methodology is useful for constructing a crosslinked structural model of phenolic resins with various conversions, not only for less crosslinked phenolic resins before gelation but also for highly crosslinked phenolic resins.
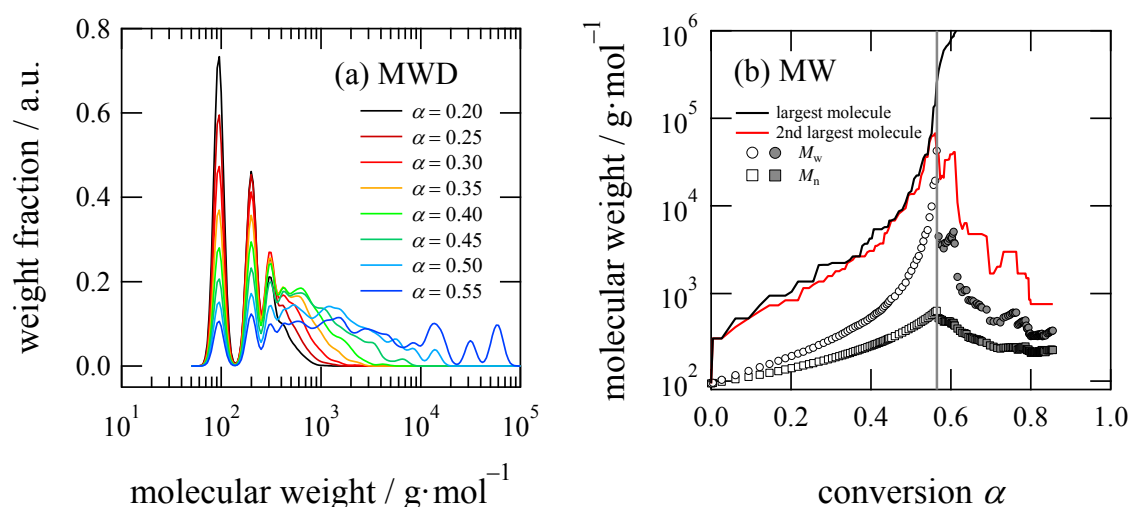

Figure 5.9 (a) Changes in MWD of phenolic units of **L-R1-ra** depending on reaction conversion. (b) Plot of MWs of the largest and second-largest molecules and their M_w and M_n as a function of reaction conversion. The glay line in (b) is a gel point estimated from the percolation model. The filled circles for M_w and M_n represent the MWs of the soluble fraction in the post-gel regime.

Although these reactions in this MD simulation proceed too quickly compared to the actual reaction, the obtained structures showed good agreement in the chemical structures and MWDs. The reason why this pseudo reaction gave an appropriate structure model is suggested in a small reaction probability used for sampling the energetically stable structures efficiently. This situation in MD simulation corresponds to the slow reaction process in the actual reaction system. This assumption is supported by system size independence of the chemical structures in these MD results.

5.3.4 Densities of Crosslinked Phenolic Resins

Changes in the densities of the reacted phenolic resins are shown in Figure 5.10(a) for the equilibrated structure at 300 K as a function of conversion. There is no system size dependence of the density between **L-R1-ra** and **S-R1-ra** or **L-R1-ho** and **S-R1-ho**. The calculated values at $\alpha = 0$ and $\alpha = 0.55$ for **L-R1-ra** agree well with the experimental values of 1.06 g/cm^3 for phenol and 1.25 g/cm^3 for novolac resins (**NV-1**) within an 8% error. The density increases as the reaction proceeds in the pre-gel regime for **L-R1-ra**, **L-R1-ho**, **S-R1-ra**, and **S-R1-ho** ($\alpha = 0$–0.56). This result can be explained by the distances between two phenolic rings becoming shorter than in the unreacted state due to direct chemical bonds between the methylene linkages. On the other hand, a decrease in density is observable in the post-gel regime ($\alpha \geq 0.6$) for all the reactions. The change in the unit fractions shown in Figure 5.7 indicates that this behavior was caused by steric restrictions originating from the branching structure.
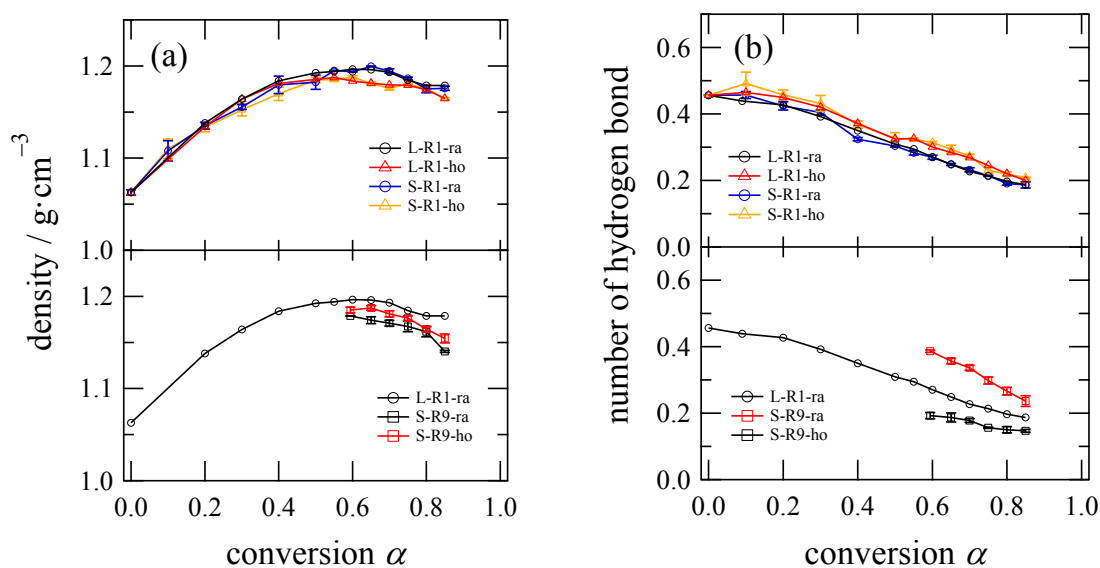

Figure 5.10 (a) Density as a function of conversion α at 300 K. (b) Number of hydrogen bonds per hydroxyl group of phenolic rings as a function of conversion α at 300 K.

The densities of **L-R1-ho** and **S-R1-ho** exhibit slightly smaller values than those for **L-R1-ra** and **S-R1-ra** at the same conversion. Similarly, the density in **S-R9-ra** is smaller than that in **S-R9-ho**. Such a difference, depending on the *ortho*/*para* linkage ratio, has also been observed in other MD simulations [15,39,40]. These differences are the result of hydrogen bonding structures that depend on the *o–o'*/*o–p'*/*p–p'* ratio, because the branching structure is

almost independent of the reactivity of the *ortho* and *para* positions, as shown in Figure 5.7. A crosslinked network having more *o–o'* linkages would easily form hydrogen bonds because the distance between neighboring OH units is smaller than those for *o–p'* and *p–p'*. The lower density of resins having more *o–o'* linkages would result from a structural restriction for atoms to form packed structures by hydrogen bonding. Figure 5.10(b) shows the number of hydrogen bonds per hydroxyl group as a function of conversion. Here hydrogen bonds were counted according to Haughney's definition [41]. The number of hydrogen bonds decreases as the reaction conversion increases for all of the simulations, indicating that methylene linkages are unlikely to form hydrogen bonds because of topological constraints. Furthermore, the high-*ortho* novolac resins (**L-R1-ho**, **S-R1-ho**, and **S-R9-ho**) have larger numbers of hydrogen bonds than the random novolac resins (**L-R1-ra**, **S-R1-ra**, and **S-R9-ra**). Additionally, a large decrease in density is observable at high reaction conversion ($\alpha = 0.75$–0.85) for all of the MD results. Although there are no experimental reports regarding such a change for highly crosslinked phenolic resins, similar behaviors have been reported for several epoxy resins [42,43]. Enns and Gillham suggested that this behavior is due to a rubber-to-glass transition caused by a reaction-induced mobility restriction [43]. This mechanism could be applicable to our MD results for phenolic resins.
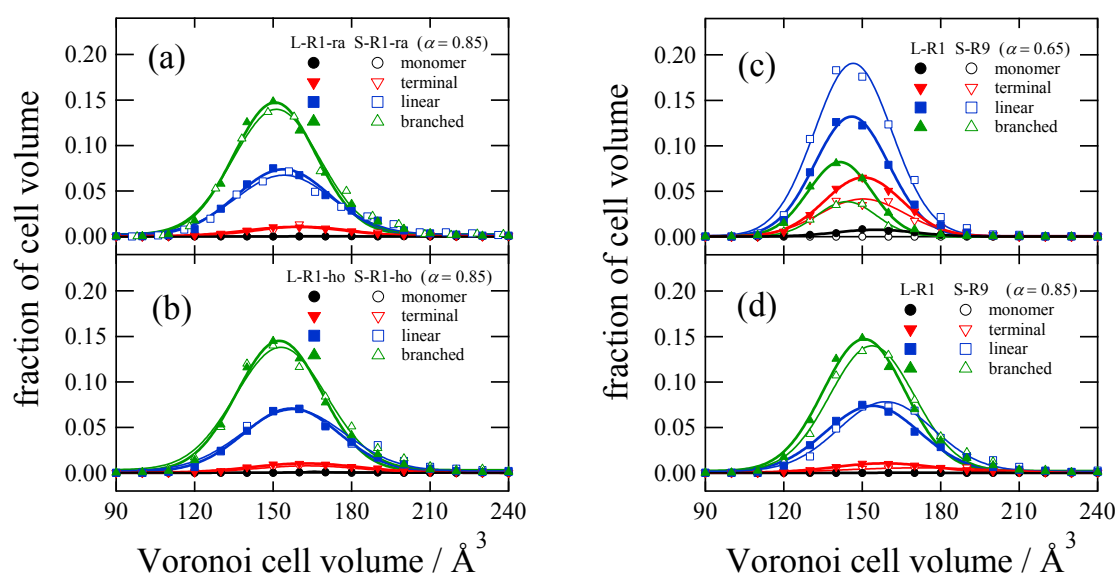

Figure 5.11 Distributions of the Voronoi cell volumes for each phenolic unit for (a) **L-R1-ra** and **S-R1-ra**, and (b) **L-R1-ho** and **S-R1-ho** at conversion $\alpha = 0.85$. Comparison of the Voronoi cell volume distribution for **L-R1-ra** and **S-R9-ra** at (c) $\alpha = 0.65$ and (d) $\alpha = 0.85$.

The densities for **S-R9-ra** and **S-R9-ho** are lower than those for **L-R1-ra** and **L-R1-ho**. These differences cannot be accounted for solely by hydrogen bonds, but are also attributable to the network topology. The initial structures of opNV and ooNV have smaller amounts of *terminal* units and larger amounts of *linear* units than novolac resins before gelation in **L-R1-ra** and **L-R1-ho** ($\alpha \sim 0.55$). Generally, the dynamics of *linear* units tend to be restrained to a greater extent than those of *monomer* or *terminal* units; therefore, the mobility of atoms after gelation is expected to be lower than that of novolac resins having wide MWDs. Consequently, it becomes difficult for ooNV and opNV to fill up a condensed structure since crosslinking proceeds because of topological constraints. On the other hand, phenolic units having high mobilities exist even at large conversions for **L-R1-ra**, **L-R1-ho, S-R1-ra**, and **S-R1-ho** because of their diversities of molecular configurations and wide MWDs. To verify this conjecture, a histogram of occupation volume was calculated for each phenolic unit using Voronoi tessellation, and these are displayed in Figure 5.11. The size distributions of the occupation volumes were estimated for a particle, indicating that each phenolic unit had coordinates that corresponded to the center of the phenolic ring. The Voronoi volume of each phenolic unit is shown in Figures 5.11(a) and (b) for **L-R1-ra** and **S-R1-ra**, and **L-R1-ho** and **S-R1-ho** with $\alpha = 0.85$ for each equilibrated structure at 300 K. These results indicate that there is no significant system size dependence between 29,000 atoms and 232,000 atoms and that the features of the crosslinked networks can be considered to be almost the same. Figures 5.11(a) and (b) also show good agreement with the Voronoi volume distribution, but there is a slight difference between the peak positions for *linear* units. This difference suggests that a *linear* unit is constrained to fill a volume due to hydrogen bonding and that the characteristics of a network structure cannot be determined solely by the local reactivities at the *ortho* and *para* positions.

Comparisons of the Voronoi cell volumes for **L-R1-ra** and **S-R9-ra** at different conversions ($\alpha = 0.65$ and 0.85) are shown in Figures 5.11(c) and (d). Here the crosslinked structures at $\alpha = 0.65$ and 0.85 are a loosely crosslinked network structure close to the gel point and a highly crosslinked structure, respectively. When compared at the same conversion, the average occupation volume per unit follows the order *monomer > terminal > linear > branched* for both results, indicating steric hindrance by the methylene linkages and a decline in configurational freedom caused by mobility constraints as the crosslinking reaction proceeds. No difference between the peak positions of **L-R1-ra** and **S-R9-ra** is observable at $\alpha = 0.65$, although the cell volume fractions differ because of the initial configurations of the molecules.

On the other hand, differences between the peak positions are observable at $\alpha = 0.85$, although the fraction of each phenolic unit is similar. In **S-R9-ra**, the *terminal* and *linear* units occupy larger volumes than they do in **L-R1-ra**. These results indicate that phenolic units do not efficiently fill a space by molecular rearrangement because of topological and dynamic constraints resulting from molecular conformations. The result for **L-R1-ra** shows that *monomer* and *terminal* units play important roles in retaining a packed structure because they have higher mobilities than *linear* and *branched* units and lesser steric constraints resulting from substitution units. Thus, it can be concluded that the structural diversity generated from the reaction from phenol monomers contributes to forming a packed network structure, even for a high degree of crosslinking after gelation. These results indicate that the equilibrated structure of a crosslinked network is clearly affected by structural restrictions due to methylene linkages and hydrogen bonds; the dominant factor that determines the properties of the crosslinked structure could be network topology resulting from methylene linkages, whereas the effect of hydrogen bonds may decrease as the reaction proceeds.

5.3.5   Scattering Function

Figure 5.12 shows the experimental scattering function $I(q)$, the structure factor $S(q)$ estimated from scattering experiments, and the $S(q)$ calculated from MD simulations in phenolic resins before and after gelation. Here the observed scattering profiles $I(q)$ were calculated as azimuthal averages of the two-dimensional isotropic scattering patterns for **NV-1** and **NV-2**. One-dimensional experimental scattering intensities $I(q)$, after combining SAXS and WAXS profiles, are shown in Figure 5.12(a).

In a wide-angle range with $q > 10$ nm^{-1}, a shift of the peak top near 12 nm^{-1} can be observed toward low q as the reaction proceeds, as shown in Figures 5.12(a) and (b). This result is consistent with previous XRD studies reported by Spurr and Erath [44,45] in which they concluded that the peak shift would result from an increase in the average interatomic length of C–C bonds with conversion due to the formation of aliphatic C–C bonds between methylene and aromatic carbon atoms that are longer than the aromatic C–C bonds on phenolic rings. These results in Figures 5.12(a) and (b) could relate to a decrease in density with conversion, as shown in Figure 5.10(a), and an increase in the Voronoi volume with conversion, as shown in Figures 5.11(c) and (d); namely, a shift in the peak position results from an extension of the distance between phenolic units as the crosslinking reaction proceeds.
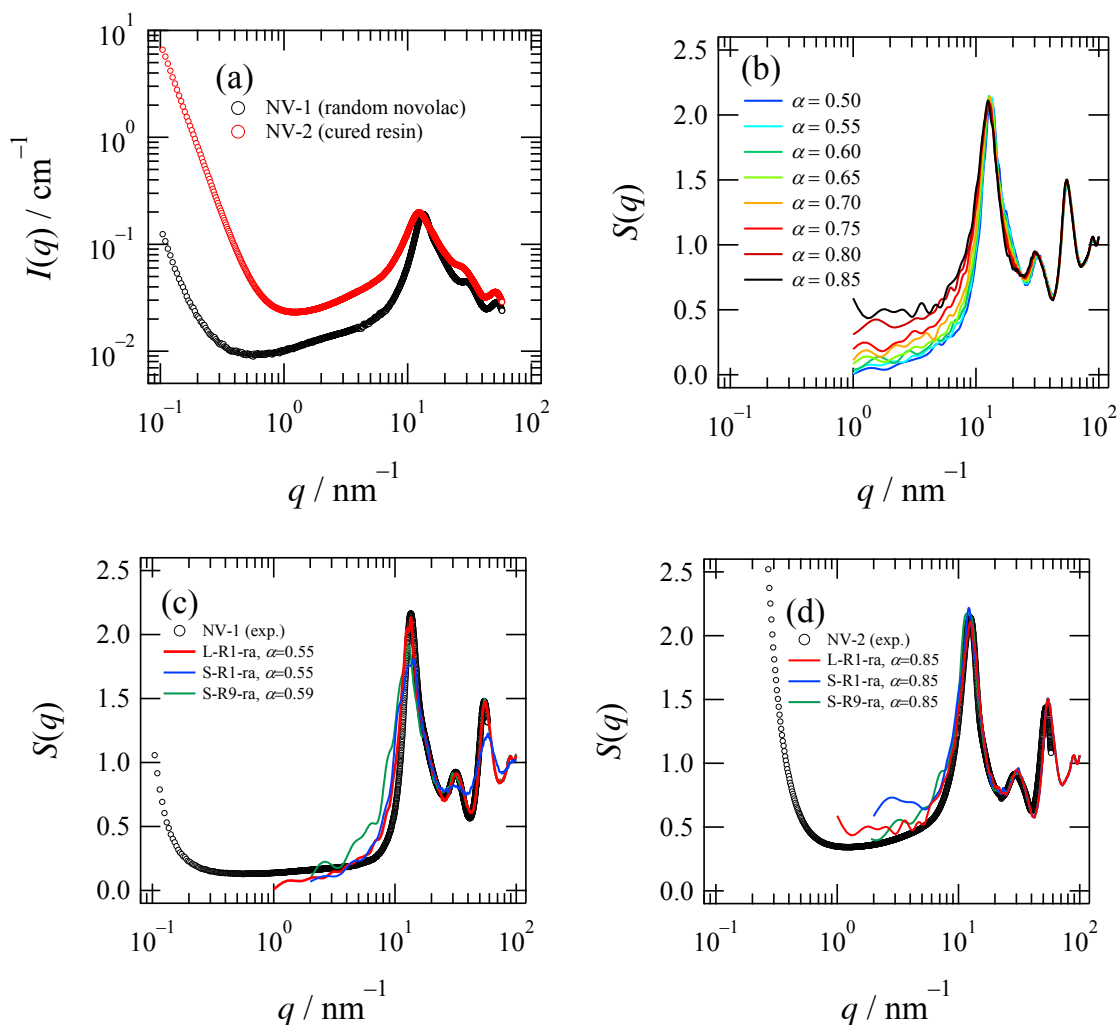
Figure 5.12 (a) Experimental scattering functions obtained from SAXS and WAXS for **NV-1** and **NV-2**. (b) Structure factors calculated from MD simulation for **L-R1-ra** at various conversions. (c) Estimated structure factors of **NV-1**, **L-R1-ra**, and **S-R1-ra** at conversion $\alpha = 0.55$ and **S-R9-ra** at conversion $\alpha = 0.594$. (d) Estimated structure factors of **NV-2** and of **L-R1-ra**, **S-R1-ra**, and **S-R9-ra** at conversion $\alpha = 0.85$.

To verify the structure factor $S(q)$ calculated from the MD simulation results, experimental $S(q)$ values were obtained by removing incoherent scattering from the observed $I(q)$ and inserting necessary corrections, as described in Equation (5.13) for **NV-1** and **NV-2**. Here it was assumed that **NV-1** and **NV-2** corresponded to the structure of **L-R1-ra** with $\alpha = 0.55$ and 0.85, respectively, based on their chemical compositions. The structure factor for **NV-1** and those calculated at $\alpha = 0.55$ for **L-R1-ra** and **S-R1-ra** are shown in Figure 5.12(c). In the same way, Figure 5.12(d) shows a comparison of **NV-2** and $S(q)$ at $\alpha = 0.85$ for **L-R1-ra** and **S-R1-ra**. These results agree well with the $S(q)$ obtained from the MD simulation and the

experimental results for $q > 4$ nm^{-1}. Coincidence of the peak positions at $q = 12$ nm^{-1}, 30 nm^{-1}, and 50 nm^{-1} confirms the validity of the local interatomic distances in the structure obtained with the force field parameters and the atomic configurations used in this MD simulation. As shown in Figure 5.12(c), the peak positions and sharpness of the experimental results are well reproduced by **L-R1-ra**; however, **S-R1-ra** shows a lack of sharpness in the peaks. This characteristic could result from the population size being insufficient to estimate $S(q)$ in **S-R1-ra**; in other words, the number of atoms (29,000) was not sufficient to generate a structure factor $S(q)$ to compare with the experimental results. The q range was also limited by the number of atoms in this simulation; scattering profiles at $q < 2$ nm^{-1} cannot be calculated in principle for **S-R1-ra**, **S-R1-ho**, **S-R9-ra**, and **S-R9-ho** due to their small cell sizes; therefore, the simulation conditions for **S-R1-ra**, **S-R1-ho**, **S-R9-ra**, and **S-R9-ho** are not appropriate for studying the characteristic change in the SAXS profiles that is observed in swollen phenolic networks around the gel point [28,46]. As a result, it is necessary to undertake a large-scale full atomistic simulation with 232,000 atoms, as performed in **L-R1-ra** and **L-R1-ho**, to study the precise structure and properties of phenolic resins. The structure factors $S(q)$ of **S-R9-ra** at $\alpha = 0.594$ (before gelation) and at $\alpha = 0.85$ (highly crosslinked) were also calculated and are shown in Figures 5.12(c) and (d), respectively. The shapes of the curves are essentially similar to those of the experimental and calculated curves of **L-R1-ra** and **S-R1-ra**, but there are discrepancies in terms of the peak position and the shape of the first peak, which indicate the existence of a local configuration.

An increase in intensity as the reaction proceeds is observable in the small-angle region at $q < 10$ nm^{-1} in both the experimental results (Figure 5.12(a)) and the MD results (Figure 5.12(b)). This increase indicates an increase in the structural inhomogeneity on the order of several angstroms to several nanometers during the crosslinking reaction from the gelation stage to the highly crosslinked stage, which can be observed as a structural change in the loosely crosslinked region around the gel point by SAXS experiments [28,46]. These computational results predict an increase in structural inhomogeneity as the crosslinking reaction proceeds, even at high conversions.
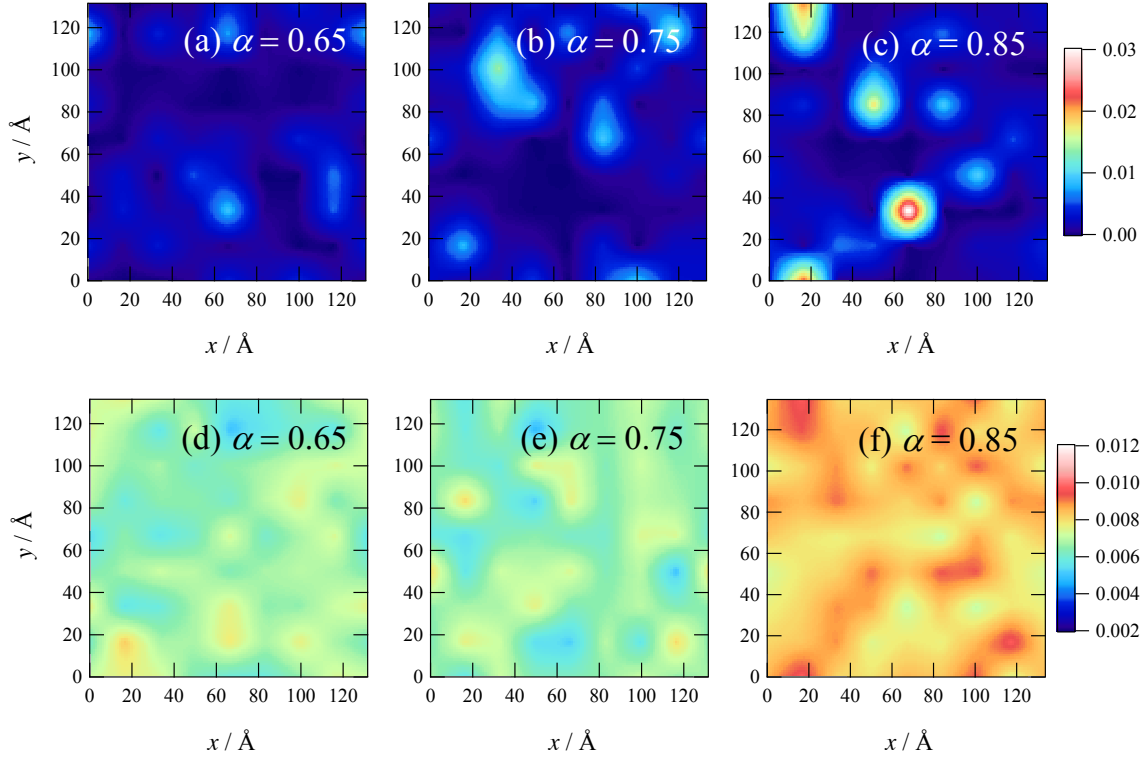
Figure 5.13 Distribution contours for (a)–(c) mass density fluctuations [g^2/cm^6] and (d)–(f) crosslink density distributions [$Å^{-3}$] for **L-R1-ra** at different conversions: (a), (d) $\alpha = 0.65$; (b), (e) $\alpha = 0.75$; and (c), (f) $\alpha = 0.85$.

In order to understand the structural inhomogeneity as revealed by the reciprocal space analysis, the spatial mass density fluctuation and crosslink density distribution in real space are depicted as contour maps in Figure 5.13 for **L-R1-ra** at different conversions. These maps were obtained using the following procedure. A simulation box was divided into 8×8×8 cells, and the mass density fluctuation given by $(\Delta\rho)^2 = [<\rho> - \rho]^2$ and the crosslink density distribution were calculated for each cell and visualized as contour maps [47]. The crosslink density was determined as the number of methylene units for each cell volume. Figures 5.13(a)–(c) indicate that the mass density fluctuation in the simulation box is initially small at $\alpha = 0.65$; however, it increases as the crosslinking reaction proceeds. The distance between domains having a large mass density fluctuation is on the order of several nanometers, which corresponds to a q of 1–10 nm^{-1} in reciprocal space. On the other hand, Figures 5.13(d)–(f) suggest that the correlation between the mass density fluctuation and the crosslink density fluctuation is weak. This result is consistent with the reaction mechanism obtained through the SAXS analysis of the inhomogeneous distribution of crosslinks. It is assumed that restrictions in the network topology and mobility, as mentioned above, could result in the formation of this

inhomogeneous structure. The reactive functional sites located in the vicinity of the reacted sites could have high reaction probability because they have high contact probability due to structural constraints. To investigate this mechanism more precisely, further spatial analysis regarding molecular mobility during the reaction process and the dependency of the reaction conditions was performed using Voronoi tessellation analysis. The techniques of Voronoi tessellation and contour mapping of material properties are useful tools to understand the structure–property relationships from an atomistic viewpoint. In order to characterize the relationships between the structural, mechanical, and thermal properties of constructed structures, structural analysis under tensile elongation and thermal processes will be reported elsewhere.

5.4 Conclusions

A network structure of crosslinked phenolic resins was constructed using a large-scale atomistic MD simulation with a pseudo-reaction model, in which the simulation was performed using J-OCTA and LAMMPS on K Computer. Force field parameters with GAFF and RESP charges based on the RHF/6-31G(d,p) calculation were applied for phenol and reacted phenolic resins. The crosslinked structural model obtained using phenol for the initial molecules exhibited good agreement with the experimental results in terms of the branching structure of the phenolic units, methylene linkages, MWDs, densities, and scattering functions. The structure factor $S(q)$ calculated for the phenolic resins indicated the existence of inhomogeneous crosslinking that expanded as the reaction proceeded after gelation, which agrees with the inhomogeneous reaction mechanism deduced from SAXS experiments. The experimental MWD before gelation and the scattering function were well reproduced by a large-scale simulation with 232,000 atoms. The reaction method performed in this chapter has the advantage of the reactivity control on *ortho* and *para* positions in phenolic resins. Note that there is a possibility that this reaction procedure is refined by reaction scheme based on kinetic rate theory proposed by Okabe et al. [48] if the activation energy and an acceleration factor were given for each reaction. However, it is very difficult to estimate the activation energy and acceleration factor for phenolic resin by *ab initio* calculation because complex formation and phase separation were often used to control *ortho* and *para* reactivity in the synthesis of specific phenolic resin. Hence, we believe that our reaction procedure is suitable for this purpose.

This study also demonstrated the importance of the initial molecular configuration: a network structure constructed from monodisperse novolac oligomers showed a lower density

than that from monomeric phenol because of structural constraints, which was verified by the change in the occupation volume of the phenolic units for a crosslinking reaction using Voronoi tessellation analysis. These results indicate that the structure and properties of crosslinked phenolic resins can be controlled by molecular topology concerning the crosslinking conversion, branching structure (*monomer*/*terminal*/*linear*/*branched* ratio), methylene linkages (*o–o'*/*o–p'*/*p–p'* ratio), and MWD.

References

1. D. Rigby, and R. Roe, *Macromolecules*, 1990, **23**, 5312–5319.
2. S. Yang, and J. Qu, *Phys. Rev. E*, 2014, **90**, 012601.
3. http://math.lbl.gov/voro++/
4. http://lammps.sandia.gov/
5. J. Wang, R. M. Wolf, J. W. Caldwell, P. A. Kollman, and D. A. Case, *J. Comput. Chem.*, 2004, **25**, 1157–1174.
6. C. I. Bayly, P. Cieplak, W. D. Cornell, and P. A. Kollman, *J. Phys. Chem.*, 1993, **97**, 10269–10280.
7. S. Nosé, *J. Chem. Phys.*, 1984, **81**, 511–519.
8. W. G. Hoover, *Phys. Rev. A*, 1985, **31**, 1695–1697.
9. M. Parrinello, and A. Rahman, *J. Appl. Phys.*, 1981, **52**, 7182–7190.
10. R. W. Hockney, and J. W. Eastwood, *Computer Simulation Using Particles*, Adam Hilger: New York, 1989.
11. C. Li, and A. Strachan, *J. Polym. Sci. Part B Polym. Phys.*, 2015, **53**, 103–122.
12. M. Frenkel, X. Hong, Q. Dong, X. Yan, and R. D. Chirico, In *Thermodynamic Properties of Organic Compounds and their Mixtures* (*Landolt-Börnstein - Group IV Physical Chemistry*), M. Frenkel, and K. N. Marsh, Eds., Springer: Berlin, pp. 11–36, 2002.
13. D. A. Mooney, F. Müller-Plathe, and K. Kremer, *Chem. Phys. Lett.*, 1998, **294**, 135–142.
14. S. L. Mayo, B. D. Olafson, and W. A. Goddard III, *J. Phys. Chem.*, 1990, **94**, 8897–8909.
15. A. Izumi, T. Nakao, and M. Shibayama, *Soft Matter*, 2012, **8**, 5283–5292.
16. B. Arab, and A. Shokuhfar, *J. Nano- Electron. Phys.*, 2013, **5**, 01013.
17. A. Gardziella, L. A. Pilato, and A. Knop, *Phenolic Resins: Chemistry, Applications, Standardization, Safety and Ecology*, second ed., Springer: Berlin, 2000.
18. M. I. Aranguren, J. Borrajo, and R. J. J. Williams, *Ind. Eng. Chem. Prod. Res. Dev.*, 1984, **23**, 370–374.

19. W. H. Stockmayer, *J. Chem. Phys.*, 1943, **11**, 45–55.

20. T. Yamagishi, T. Nakatogawa, M. Ikuji, Y. Nakamoto, and S. Ishida, *Angew. Makromol. Chem.*, 1996, **240**, 181–186.

21. D. Stauffer, and A. Aharony, *Introduction to Percolation Theory*, 2nd ed., Taylor & Francis: London, 1994.

22. T. Yamagishi, M. Nomoto, S. Ito, S. Ishida, and Y. Nakamoto, *Polym. Bull.*, 1994, **32**, 501–507.

23. T. Yamagishi, M. Nomoto, S. Yamashita, T. Yamazaki, Y. Nakamoto, and S. Ishida, *Macromol. Chem. Phys.*, 1998, **199**, 423–428.

24. N. Nomoto, T. Yamagishi, and Y. Nakamoto, *J. Network Polym., Jpn.*, 2006, **27**, 210–217.

25. S. Sojka, R. Wolfe, E. A. J. Dietz, and B. Dannels, *Macromolecules*, 1979, **12**, 11–14.

26. X. Zhang, and D. H. Solomon, *Polymer*, 1998, **39**, 405–412.

27. B. Ottenbourgs, P. Adriaensens, R. Carleer, D. Vanderzande, and J. Gelan, *Polymer*, 1998, **39**, 5293–5300.

28. A. Izumi, T. Nakao, and M. Shibayama, *Soft Matter*, 2013, **9**, 4188–4197.

29. R. J. Roe, *Methods of X-ray and Neutron Scattering in Polymer Science*, Oxford University Press: New York, 2000.

30. T. E. Faber, and J. M. Ziman, *Philos. Mag.*, 1965, **11**, 153–173.

31. S. Maji, O. Urakawa, and T. Inoue, *Polym. J.*, 2014, **46**, 584–591.

32. H. Masunaga, H. Ogawa, T. Takano, S. Sasaki, S. Goto, T. Tanaka, T. Seike, S. Takahashi, K. Takeshita, N. Nariyama, H. Ohashi, T. Ohata, Y. Furukawa, T. Matsushita, Y. Ishizawa, N. Yagi, M. Takata, H. Kitamura, K. Sakurai, K. Tashiro, A. Takahara, Y. Amemiya, K. Horie, M. Takenaka, T. Kanaya, H. Jinnai, H. Okuda, I. Akiba, I. Takahashi, K. Yamamoto, M. Hikosaka, S. Sakurai, Y. Shinohara, A. Okada, and Y. Sugihara, *Polym. J.*, 2011, **43**, 471–477.

33. H. Ogawa, H. Masunaga, S. Sasaki, S. Goto, T. Tanaka, T. Seike, S. Takahashi, K. Takeshita, N. Nariyama, H. Ohashi, T. Ohata, Y. Furukawa, T. Matsushita, Y. Ishizawa, N. Yagi, M. Takata, H. Kitamura, A. Takahara, K. Sakurai, K. Tashiro, T. Kanaya, Y. Amemiya, K. Horie, M. Takenaka, H. Jinnai, H. Okuda, I. Akiba, I. Takahashi, K. Yamamoto, M. Hikosaka, S. Sakurai, Y. Shinohara, Y. Sugihara, and A. Okada, *Polym. J.*, 2013, **45**, 109–116.

34. T. Nakao, F. Tanaka, and S. Kohjiya, *Macromolecules*, 2002, **35**, 5649–5656.

35. T. Nakao, F. Tanaka, and S. Kohjiya, *Macromolecules*, 2006, **39**, 6643–6652.

36. V. Varshney, S. S. Patnaik, A. K. Roy, and B. L. Farmer, *Macromolecules*, 2008, **41**, 6837–6842.

37. A. Izumi, T. Takeuchi, T. Nakao, and M. Shibayama, *Polymer*, 2011, **52**, 4355–4361.

38. Y. Shudo, A. Izumi, T. Takeuchi, T. Nakao, and M. Shibayama, *Polym. J.*, 2015, **47**, 428–433.

39. J. D. Monk, J. B. Haskins, C. W. Bauschlicher, and J. W. Lawson, *Polymer*, 2015, **62**, 39–49.

40. J. D. Monk, E. W. Bucholz, T. Boghozian, S. Deshpande, J. Schieber, C. W. Bauschlicher, and J. W. Lawson, *Macromolecules*, 2015, **48**, 7670–7680.

41. M. Haughney, M. Ferrario, and I. R. McDonald, *J. Phys. Chem.*, 1987, **91**, 4934–4940.

42. A. Shimazaki, *J. Polym. Sci. Part C Polym. Symp.*, 1968, **23** 555–568.

43. J. B. Enns, and J. K. Gillham, *J. Appl. Polym. Sci.*, 1983, **28**, 2831–2846.

44. R. A. Spurr, E. H. Erath, and H. Myers, *Ind. Eng. Chem.*, 1957, **49**, 1838–1839.

45. E. H. Erath, and R. A. Spurr, *J. Polym. Sci.*, 1958, **28**, 233–234.

46. A. Izumi, T. Nakao, and M. Shibayama, *Polymer*, 2015, **59**, 226–233.

47. J. Kang, C. Wang, D. Li, G. He, and H. Tan, *Phys. Chem. Chem. Phys.*, 2015, **17**, 16519–16524.

48. T. Okabe, T. Takehara, K. Inose, N. Hirano, M. Nishikawa, and T. Uehara, *Polymer*, 2013, **54**, 4660–4668.

Chapter 6

Structure–Mechanical Property Relationships in Crosslinked Phenolic Resins investigated by Molecular Dynamics Simulation

6.1 Introduction

To design a highly crosslinked thermosetting polymers with high elastic properties, it is one of the most important and attractive subject to clarify the structure–mechanical property relationships. For phenolic resins, de Boer and Houwink performed a theoretical model calculation regarding their tensile modulus and strength, which is analogous to that of crystalline materials [1,2]. They reported significant discrepancies between the theoretical predictions and experimental results, implying that the elasticity of crosslinked phenolic polymers is essentially different from crystal elasticity. Following their works, very few further theoretical or numerical studies on these structure–mechanical property relationships have been undertaken because of the difficulties in experimental structure analysis of cured resins owing to their insolubility and infusibility. Fractographic studies using electron microscope observation have indicated the existence of crosslink inhomogeneity and stress concentration in low-crosslink-density domains when external stress is induced [3–5]. However, there is no strong evidence to demonstrate these mechanisms. Therefore, the structure–property relationships in crosslinked thermosetting resins have not been well elucidated.

In this chapter, MD simulation was carried out to investigate the mechanical properties of crosslinked phenolic resins as functions of strain in order to clarify the structure–property relationships from an atomistic perspective. A full atomic MD simulation was performed with crosslinked structures containing 220,000–232,000 atoms including 16,000 phenols with different conversions and hydrogen bonds that were constructed in Chapter 5 [6]. We characterized the structural changes in the network and tensile stress and modulus under tensile deformation, and analyzed the relationships between the moduli and the interactions.

6.2 Simulation Method

6.2.1   General

Atomistic MD simulations were performed for model construction and characterization of material properties in this work. The model structures of crosslinked phenolic resins were the same as those constructed in Chapter 5 [6]. J-OCTA 1.8 (JSOL Corp, Japan) was used for model construction. A combination of general AMBER force field (GAFF) [7] and atomic charges estimated from RHF/6-31G(d,p) calculation was chosen for the potential parameters to perform the MD simulations of phenolic resins in this study. Partial atomic charges were estimated using Gaussian 09 D (Gaussian, Inc., USA) and a restrained electrostatic potential (RESP) fitting program [8]. LAMMPS (Sandia National Laboratory, USA) [9] was used for the crosslinking reaction and subsequent MD calculation on the K computer (RIKEN Advanced Institute for Computational Science, Japan).

A standard velocity Verlet integrator was used with a time step (Δt) of 0.5 fs in the procedures for all calculations. The Nosé–Hoover thermostat [10,11] and Parrinello–Rahman barostat [12] were used to control the temperature and the pressure, respectively, with a damping parameter of 200 fs for the thermostat and 500 fs for the barostat. Lennard-Jones and Coulombic interactions were computed with a cutoff length of 11 Å and a weighting factor of 0.5 for 1–4 interactions. The Particle–Particle Particle–Mesh solver [13] was used to compute long-range Coulombic interactions with the desired relative error in forces within 10^{-5} accuracy.

6.2.2 Structure Model

In this simulation, two types of crosslinked phenolic resins, **RN** and **HO**, were used as structure models with various reaction conversions after gelation ($\alpha_{gel} = 0.57$). Here the structures of **RN** and **HO** correspond to **L-R1-ra** (random novolac system) and **L-R1-ho** (high-*ortho* novolac system) in Chapter 5, respectively. These structures were constructed from 16,000 phenols and crosslinkers using the pseudo-reaction technique, and the final number of atoms in the simulation box was approximately 220,000–230,000. The structural information is given in Chapter 5. **HO** has a larger number of hydrogen bonds than **RN** because **HO** has many *ortho-ortho'* methylene linkages causing intramolecular hydrogen bonds [14]. In addition, the branching degree of phenolic units increases with conversion, and these values are similar for **RN** and **HO** at the same conversion. Consequently, these models give the dependencies of the mechanical properties on hydrogen bonds and crosslinking (increase of branching).

6.2.3 Stress–Strain Relationships

A dynamic method using uniaxial elongation was applied to the crosslinked structures to obtain their mechanical properties with the *NPT* ensemble. The cell deformation perpendicular to the elongation direction was induced by external pressure, and the cell was constrained so as to keep a rectangular shape. The time step (Δt) in the deformation process was set to 0.5 fs. The deformation rate of the MD cell ($d\varepsilon/dt$) was kept to be 10^8 s^{-1}, which is a typical value generally used in atomistic MD simulations for crosslinked thermosetting polymers [15,16].

The elastic modulus (E) and Poisson's ratio (v) were estimated from the stress–strain relationships calculated under deformation. The strain for the elongation along the *i*-axis (ε_i) is defined as a function of time by

$$\varepsilon_i(t) \equiv \frac{L_i(t) - L_i(0)}{L_i(0)}, \tag{6.1}$$

where $L_i(0)$ denotes the initial value of L_i before elongation ($t = 0$). The strain (ε) in this chapter is given as the Cauchy strain for elongation direction under tensile deformation. The stress (σ) is defined as the stress parallel to the elongation direction subtracted by the average stress perpendicular to the elongation direction

$$\sigma = \sigma_{ii} - \frac{1}{2}(\sigma_{jj} + \sigma_{kk}), \tag{6.2}$$

where j and k denote the directions lateral to the elongation axis i. The stress tensor of the system was calculated from the forces on each atom resulting from each interaction based on the virial theorem as implemented in LAMMPS [17,18]. As is clear from the expression on the stress tensor in ref. 17, the value of stress in our MD simulation is calculated from atomic coordinates and the force on each atom. In other words, the tensile stress is strongly affected by deviation of structural parameters from equilibrium state such as bond length, and bond orientations for deformation direction. Details on molecular structural analysis are described in the next subsection.

The elastic modulus (E) was obtained from a linear fitting of the stress–strain curve in the low strain region:

$$E = \left(\frac{\partial \sigma}{\partial \varepsilon}\right)_{\varepsilon=0}. \tag{6.3}$$

Poisson's ratio (v) was calculated from the relative change in cell volume (ΔV) given by:

$$\frac{V_0 + \Delta V}{V_0} = (1 + \varepsilon)^{1-2v} - 1, \tag{6.4}$$

where $V_0 = L_i(0)L_j(0)L_k(0)$ is an initial cell volume before elongation. Each component of the stress tensor was calculated from the atomic forces via the potential function described in Equation (5.1). Thus, the values of stress and tensile moduli can be written as a sum of *bond, angle, torsion, van der Waals,* and *Coulomb* by

$$\sigma_{\text{total}} = \sigma_{\text{bond}} + \sigma_{\text{angle}} + \sigma_{\text{torsion}} + \sigma_{\text{vdW}} + \sigma_{\text{coulomb}}, \tag{6.5}$$

$$E_{\text{total}} = E_{\text{bond}} + E_{\text{angle}} + E_{\text{torsion}} + E_{\text{vdW}} + E_{\text{coulomb}}. \tag{6.6}$$

The stress–strain relationship was obtained for a cured structure with a different crosslink conversion. Then, the tensile modulus and the Poisson's ratio were computed, and the relationships between the moduli and the interactions were analyzed in detail.

6.2.4 Structure Analysis

Figure 6.1 shows the parameters evaluated in the structural analysis. The changes in the atomistic structure under deformation were analyzed in terms of chemical bond length (l), angle (θ), hydrogen bonds, and bond orientation as a function of strain. In this chapter, weak non-bonding interactions such as π–π and π–H were not analyzed in detail, because their interaction energy is not the dominant factor on governing the structures of phenols as suggested by computational studies using classical MD and *ab initio* calculation [19]. The bond length between two phenolic units ($l_{\text{PhOH-PhOH}}$) was also calculated, which was defined as the distance between the center-of-mass of connected phenolic rings. The strain dependencies of orientation degree (S) were calculated for two kinds of C–C bonds and PhOH–PhOH as shown in Figure 6.1(b). S is represented by the orientation order parameter defined as

$$S = \frac{3\langle \cos^2 \beta \rangle - 1}{2}, \tag{6.7}$$

where β is the angle between bond direction and elongation axis. S is the definition commonly used to describe orientations of crystals or liquids crystal. β is calculated as scalar product of bond vector ($\vec{l}$) and unit vector for elongation axis ($\vec{e_i}$) by

$$\cos \beta = \frac{\vec{l} \cdot \vec{e_i}}{|\vec{l}|}, \tag{6.8}$$

S equals to 0 when the bond vector distributes at random. In case that the molecular chain orientates to the elongation axis as shown in Figure 6.1(b), the values of S for C_{Ar}–C_{Ar}, C_{CH2}–

C_{Ar} and PhOH–PhOH are expected to be larger than 0. Conversely in case that all phenolic rings are arranged such that their planes are perpendicular to the elongation axis, the value of S shows negative value. Thus, the orientation of the bond is represented by the orientation of the molecule. After all, if the orientation of the molecular chain is induced by tensile deformation, the value of S for these bonds is expected to increase as the tensile deformation progresses.
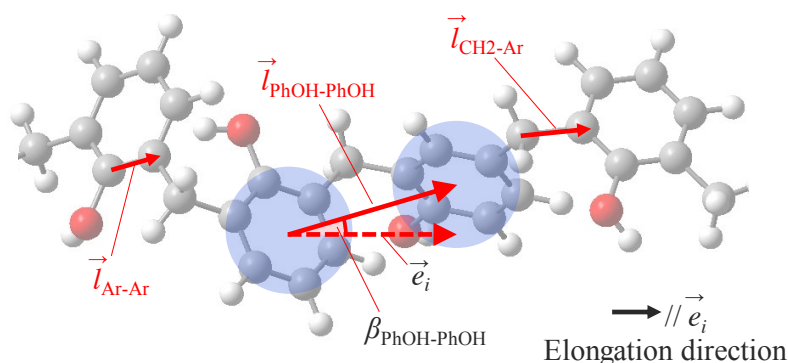
(a)
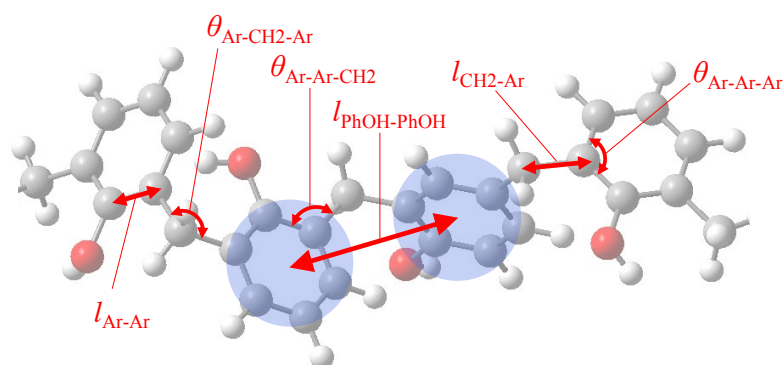
(b)

Figure 6.1 (a) Definition of bond length (l) and bonding angle (θ) for local chemical structure. Subscripts for l and θ indicate sets of atomic species (Ar: carbon of benzene ring, CH$_2$: carbon of methylene). $l_{PhOH-PhOH}$ is defined as the distance between the center-of-mass of directly connected two phenolic rings via methylene linkage. (b) Definition of bond vector ($\vec{l}$) and orientation angle (β). $\vec{l}$ is defined as the relative position vector of two atoms or the center-of-mass of two phenolic rings. β is angle between $\vec{l}$ and unit vector ($\vec{e_i}$) which is parallel to elongation axis.

To understand the development of spatial inhomogeneity distribution in the deformation process, the spatial distributions on stress (σ), and the crosslink density were also

computed and visualized. The entire simulation box was divided into $10 \times 10 \times 10$ small cubic cells, then the corresponding information in each cell was collected and expressed as contour maps.

6.3 Results and Discussion

6.3.1 Stress–Strain Relationships

The calculated stress–strain curves for **RN** under uniaxial elongation with three different conversions are shown in Figure 6.2. These results clearly show that the total stress increases with strain and conversion. The stress shows a linear change in a strain range of $0 \leq \varepsilon \leq 0.02$ for all simulation results. Consequently, tensile modulus was calculated as the gradient of the fitting line in this region according to the definition in Equation (6.3). Poission's ratio v was also evaluated in this range.
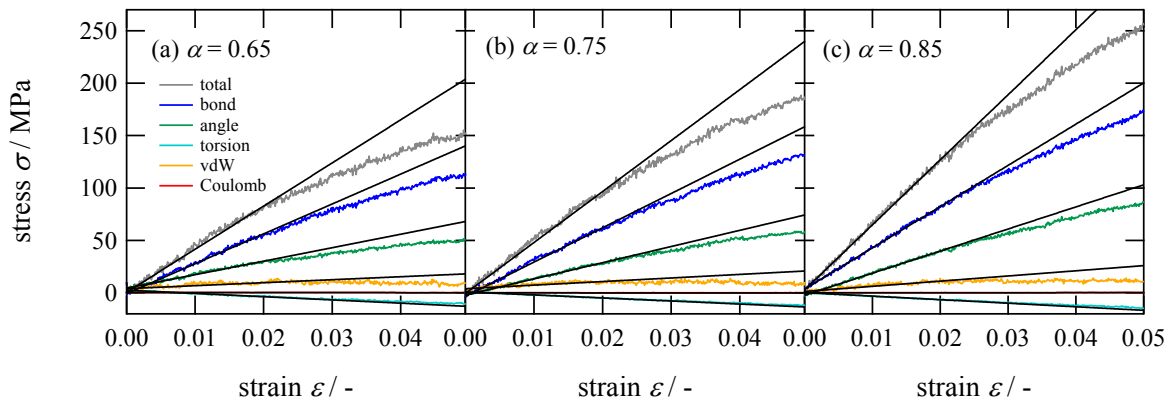
Figure 6.2 The stress–strain curves of crosslinked phenolic resin (**RN**) with various crosslink conversions (a) $\alpha = 0.65$, (b) 0.75, and (c) 0.85 under uniaxial elongation at 300 K. Solid lines represent a fitting result in a range of strain $0 \leq \varepsilon \leq 0.02$.

Figures 6.3(a) and (b) indicate the dependency of tensile modulus E on conversion for **RN** and **HO**, respectively. The estimated tensile modulus is well consistent with the experimental value 5–6 GPa at conversions of 0.8–0.85. The estimated Poisson's ratio is also shown in Figure 6.3(c). Similar dependencies for tensile modulus and Poisson's ratio as crosslinking proceeds are also seen in the MD simulation for phenolic resins reported in our previous study [20] and in studies on general thermosetting resins [15,21]. These results clearly show that the structure model and force field parameters used are appropriate to investigate

structure–mechanical property relationships. The tensile modulus in **HO** represents a slightly lower value than that of **RN** when compared at the same conversion. The dependencies of tensile modulus and Poisson's ratio on conversion are quite similar in both systems. As shown in Table 1, **HO** has a larger number of hydrogen bonds than **RN** at the same conversion. Hence, the elasticity in crosslinked phenolic resins is indicated to originate from network topology related to the local chemical bonds, not from hydrogen bonds.
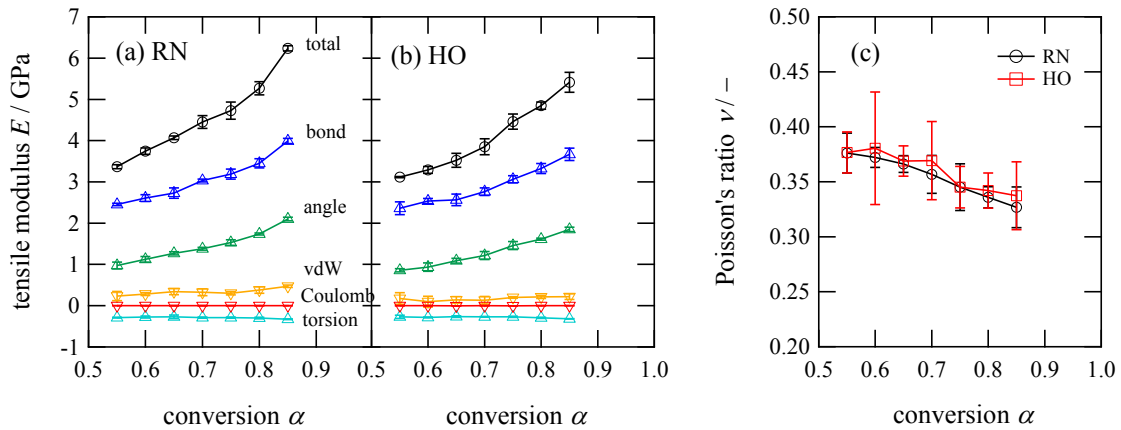
Figure 6.3 The tensile modulus as a function of crosslink conversion α for (a) **RN** and (b) **HO** estimated from a linear fitting of corresponding stress–strain curves. (c) Estimated Poisson's ratio as a as a function of crosslink conversion α for (a) **RN** and (b) **HO**.

To analyze the relationships between the moduli and interactions in detail, the total stress was divided into five molecular interactions that correspond to five terms on the right side of Equation (6.5) and the computed results are shown in Figure 6.2. In addition to the total stress, the tensile moduli of the five interactions were estimated using a linear fitting, which correspond to five terms on the right side of Equation (6.6), and are given in Figures 6.3(a) and (b). These results clearly show that *bond* and *angle* components mainly contribute to the total tensile stress and modulus, whereas *torsion* and non-bonding interactions including *vdW* and *Coulomb* do not. Furthermore, the tensile moduli of *bond* and *angle* increase as crosslinking proceeds, whereas those of *vdW* and *Coulomb* are almost independent of conversion.

Figures 6.4(a)–(c) show the potential energy changes $\Delta U(\varepsilon) = U(\varepsilon) - U(0)$ for all interactions of **RN** under tensile elongation for with different conversions at 300 K. Here, $U(\varepsilon)$ is a normalized potential energy divided by the number of phenolic rings in the simulation box. The potential energy changes of non-bonding interactions, i.e. *vdW* and *Coulomb*, show larger changes than those of bonding interactions as strain increases, although the tensile moduli of

the non-bonding interactions are small. This disagreement is accounted for by the isotropy of non-bonding interactions; the structural anisotropy does not change by this deformation, although the distance between non-bonded neighboring atoms changes. Conversely, the elasticity is strongly correlated with a change of anisotropy in local bonding interactions under deformation. These results indicate that the tensile modulus is mainly governed by the structural restriction by chemical bonds. Hereafter, we focus the structural analysis on **RN**, and discuss the structural changes under deformation.
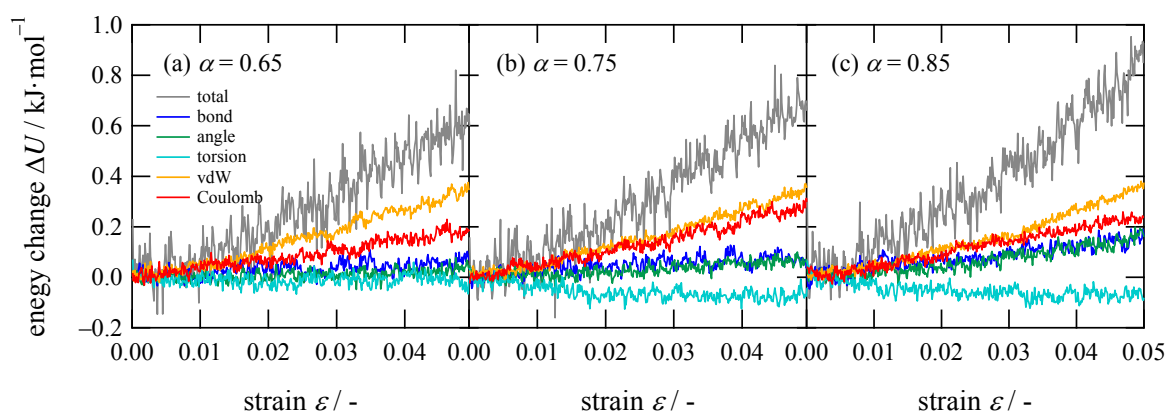
Figure 6.4   Changes in potential energy of crosslinked phenolic resin (**RN**) with various crosslink conversions α = (a) 0.65, (b) 0.75, and (c) 0.85 under tensile elongation at 300 K.

6.3.2   Structure Analysis

Figures 6.5(a) and (b) show changes in bond length and angle in the network under uniaxial elongation for **RN** with α = 0.85. These results clearly show that the average bond length and angle do not noticeably change by deformation in this range ($0 \leq \varepsilon \leq 0.05$). This corresponds to a change in potential energy in Figure 6.4. On the assumption that the changes of bond length and angle only concern carbon atoms, the average changes in bond length and angle calculated using force field parameters and potential energy changes are estimated to be 0.007 Å and 0.4°, respectively, at ε = 0.05. These values are consistent with the results in Figure 6.5. These results suggest that the elasticity of crosslinked phenolic resins does not originate from the stretching and compression of chemical bonds or angles. This statement clearly contradicts the crystal elasticity model supposed by de Boer [1]. The small deviations of bond length or angle also suggested the concentration of stress on specific domains.
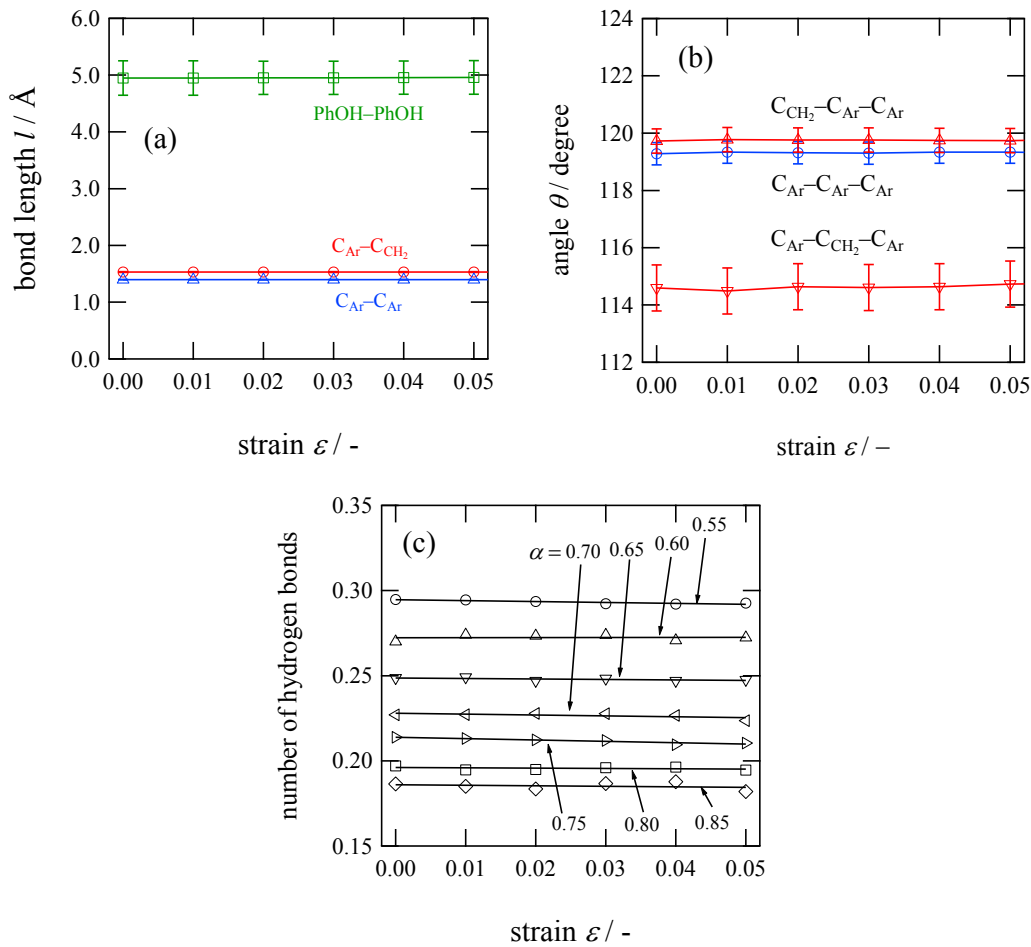
Figure 6.5 Changes in chemical structure under tensile elongation for **RN**: (a) average bond length (α = 0.85), (b) average angles (α = 0.85), and (c) a number of hydrogen bonds with different conversions.

The distance of center-of-mass between connected phenolic units ($l_{\text{PhOH–PhOH}}$) is also given in Figure 6.5(a). The cell volume increased during tensile deformation as shown in Figure 6.3(c), though $l_{\text{PhOH–PhOH}}$ did not noticeably change in this strain range. These results indicate an increase of the distance between phenolic units that are not connected by methylene linkage and are also supported by an increase of non-bonding energy in Figure 6.4.

　　　The change in the number of hydrogen bonds is displayed in Figure 6.5(c). In this range of tensile elongation ($0 \leq \varepsilon \leq 0.05$), the number of hydrogen bonds is preserved during elongation. This result suggests that hydrogen bonds are almost irrelevant to the mechanical response of highly crosslinked networks, as is supported by Monk et al. based on MD simulations of crosslinked novolac resins [22,23]. Results from previous study by Izumi et al. [20] and this MD simulation indicate that hydrogen bonding between hydroxyl groups in the

crosslinked network plays an important role in maintaining a static condensed structure, but does not affect the dynamic properties significantly.

To understand the effect of stress concentration on specific chemical bonds, the distributions of C–C bond lengths were calculated for C_{Ar}–C_{Ar} and C_{Ar}–C_{CH2} bonds in the methylene linkages, as displayed in Figures 6.6(a) and (b). These figures clearly indicate that bond length distributions are represented by a typical Gauss-type function and that the shape of the distribution does not change under elongation. If inhomogeneities are caused by stretching, the distribution function may become broader and/or new peaks may emerge. However, such changes are not observed in the distribution function for these strain ranges. This suggests that the dominant factor of the tensile stress is not the bond stretching but the bond orientation along the deformation axis as discussed above.
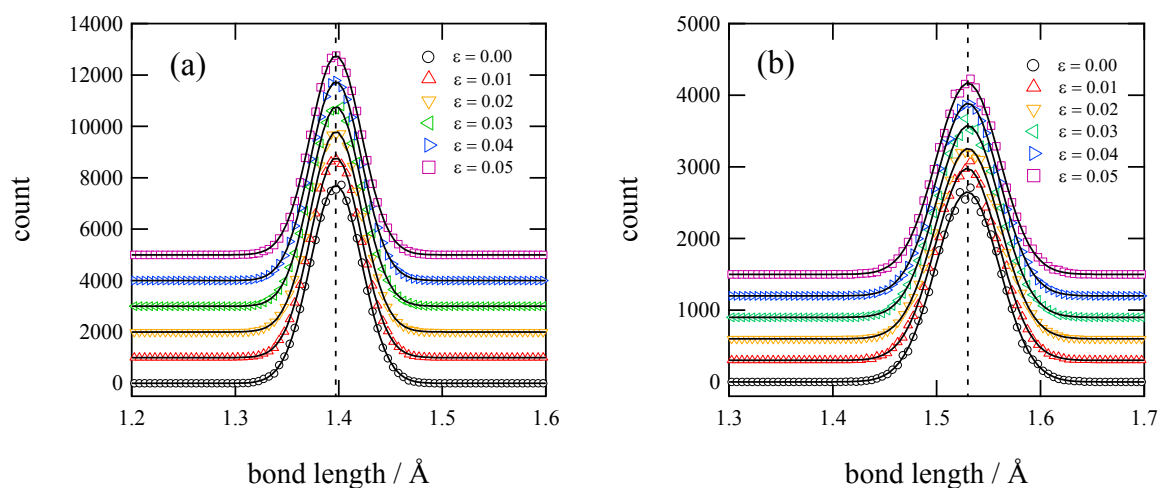
Figure 6.6   Distribution of chemical bond length (l) and their changes under tensile elongation: (a) C_{Ar}–C_{Ar} (b) C_{Ar}–C_{CH2} for **RN** at $\alpha = 0.85$ and $T = 300$ K. The graphs were shifted vertically to improve the visibility.

Figure 6.7 shows the orientation order parameter of chemical bonds and phenol–phenol linkages toward the elongation axis as a function of tensile strain for **RN** with $\alpha = 0.85$. These results clearly show an increase of bond order parameters under tensile deformation, as expected. The value of the tensile stress is determined by the diagonal component of the second-order stress tensor, which is given as a tensor product of force and displacement vector [17]. This definition indicates the stress component of bonding interaction is strongly affected by the bond length and the orientation degree for elongation axis on these two vectors. The results of Figures 6.5 and 6.7 suggested that the increase in the bond orientation towards the deformation

axis under deformation manly contributes to the tensile stress of the crosslinked phenolic resins. In addition, highly crosslinked phenolic resins have a large number of crosslinking chemical bonds in the structure per volume due to the short distance between crosslinking points. Therefore, a small change in bond orientation causes a large change in the stress tensor in response to external deformation.
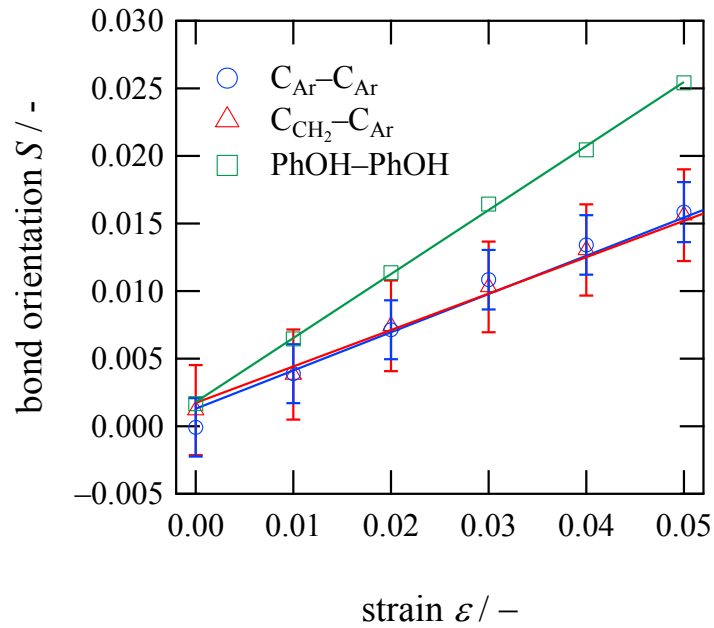

Figure 6.7   Bond orientation order parameter toward elongation axis on C_{Ar}-C_{Ar}, C_{CH2}-C_{Ar} bonds and phenol–phenol linkage for **RN** at $\alpha = 0.85$ and $T = 300$ K as a function of tensile strain.

6.3.3   Spatial Inhomogeneity

There results above suggest that the origin of the elasticity in highly crosslinked phenolic resins is not the stress concentration on specific domains in the network but rather a change of molecular orientation under structural restriction by crosslinking. To understand the relationships between elasticity and structural inhomogeneity, the spatial distributions of instantaneous stress and crosslink density and their changes are shown in Figure 6.8 for a specific plane parallel to the elongation direction under tensile deformation for **RN** with $\alpha = 0.85$. At $\varepsilon = 0$, the stress is well uniformly distributed. The existence of crosslink density fluctuations at equilibrium corresponds to experimental results, as discussed in our previous report [6]. As tensile deformation proceeds, spatial inhomogeneities are clearly observed in both stress and crosslink density. However, comparing (a) and (d), (b) and (e), or (c) and (f)

indicates little correlation in stress and crosslink density. Furthermore, the spatial location of higher-stressed domains changes as the reaction proceeds. The stress is not concentrated in specific domains, such as highly crosslinked domains, but propagates through the entire system under tensile deformation. These results indicate that there is no clear relationship between the stress and crosslink density in these strain ranges.
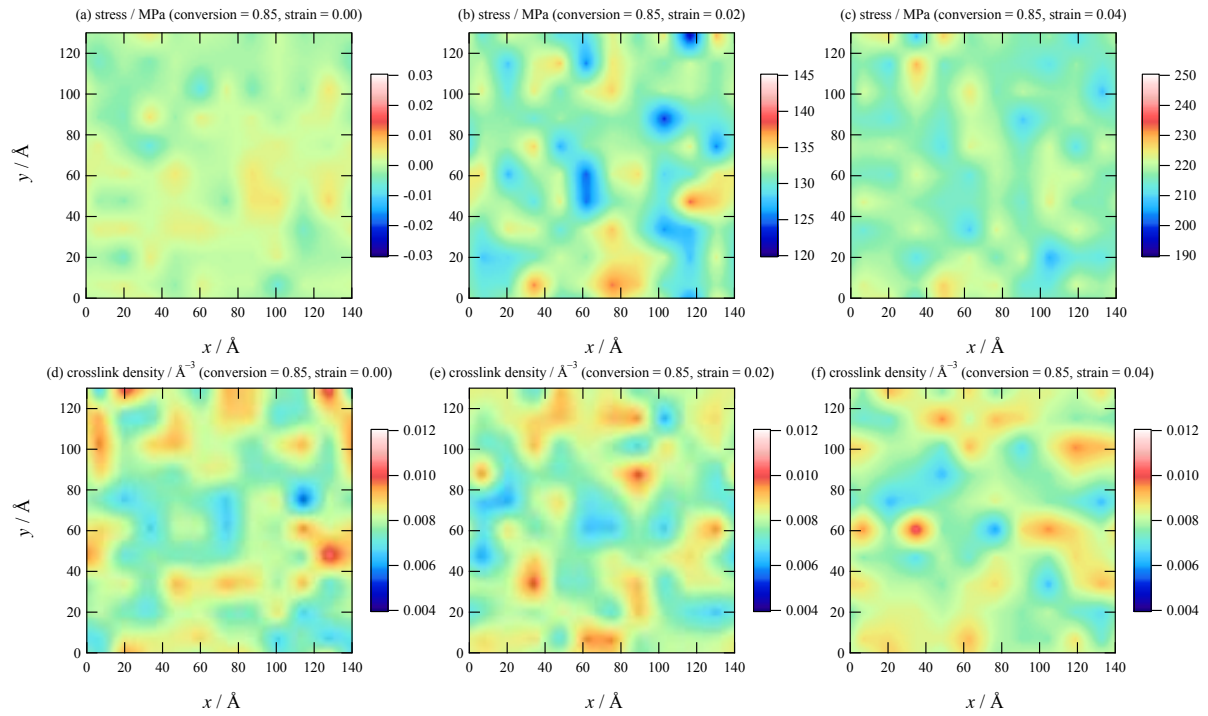

Figure 6.8   Distribution contours for (a)–(c) tensile stress σ [MPa] and (d)–(f) crosslink density [Å^{-3}] for RN with $\alpha = 0.85$ at different strains: (a), (d) $\varepsilon = 0.00$; (b), (e) $\varepsilon = 0.02$; and (c), (f) $\varepsilon = 0.04$. Horizontally axis (x) in these contours corresponds to elongation direction and the others (y and z) are transverse directions.

The results disclosed in this work suggest that the mechanical properties of crosslinked phenolic resins in the low-strain region originate from the energy derived from the elastic potential energy, not from crystal elasticity as predicted by de Boer and Houwink in 1936 [1,2]. A change in the molecular orientation especially that of the chemical bonds, causes tensile stress and modulus under structural restriction by high crosslinking. This result is assumed to be generally applicable to highly crosslinked thermosetting resins in the glassy state. These results also provide the specifications for the design of chemical structures for thermosetting polymers with high elastic moduli.

High crosslink conversion and high crosslink density are required to improve the

tensile modulus of crosslinked polymers, rather than an alteration in the chemical structure of the main chain in the network to a rigid one. A pioneering study by Megson predicted the existence of a conversion limit. For typical phenol-formaldehyde resins, it is impossible to achieve a perfect conversion ($\alpha = 1$) because of topological restrictions to the chemical structure for phenol-formaldehyde resins [24]. In fact, experimental studies based on solid-state ^{13}C NMR measurements have shown that the maximum value of α is around 0.80–0.85 for crosslinked phenolic resins by [25–27]. Conversely, as reported in our previous MD study, the density (or crosslink density) is dependent on several factors, such as molecular configuration, molecular weight distribution before gelation, and the ratio of *ortho–ortho'*, *ortho–para'* and *para–para'* methylene linkages. Therefore, it is assumed that crosslinked structures exhibiting higher tensile moduli can be obtained by optimization of these structural parameters. The development of novel "structurally optimized" novolac oligomers would be a possible strategy for this purpose, which may be achieved by means of new catalysts, combined synthesis processes, or molecular weight fractionation.

6.4 Conclusions

Structure–mechanical property relationships in highly crosslinked phenolic resins were investigated by atomistic MD simulation using uniaxial tensile deformation for the structures with different conversions and numbers of hydrogen bonds. The tensile stress and moduli were analyzed according to the molecular interactions in this model. The structural changes under the deformation process were investigated such as bond length, bond angle, hydrogen bond, and bond orientation. Spatial distribution analysis of the tensile stress and crosslink density was also conducted to study stress concentration.

Analyses of stress–strain curves and changes in chemical structure showed that the elasticity of the network is mainly derived from bonding energy potential involving the orientation of chemical bonds towards deformation axis, rather than bond stretching or hydrogen bonds. These results indicate a molecular mechanism governing mechanical properties quite different from the theoretical model proposed by de Boer. Although hydrogen bonds play important roles in static condensed structures, the dependence of elastic modulus on them is not clearly observed in our MD calculation. A spatial distribution analysis of the tensile stress and crosslink density indicated no significant correlation between them in the linear elastic region with a strain of up to 0.05.

Our MD results provide information on how to design highly elastic thermosetting resins, showing that it is essential to improve crosslink conversion and crosslink density. For phenolic resins, further increase in tensile modulus may be achieved by reducing the number of hydrogen bonds or by adjustment of molecular weight distribution for novolac resins before gelation.

In this atomistic MD study, fracturing behavior was not considered. Brittle fracturing is generally observed at ε = ca. 0.01 in experimental tensile tests for fully cured phenolic resins [2,5]. However, obvious structural changes leading to a fracturing were not seen in our MD simulation, even at ε = 0.05. The chemical bond lengths in this network structure was within a range of 0.1 Å in order that the harmonic approximation was appropriate for bond potentials in a strain range of $0 \leq \varepsilon \leq 0.05$. Experimental fracture behavior might arise from a large deformation in a specific domain owing to an inhomogeneous deformation of the specimen in the experimental set up. In MD simulation, the displacement of all atoms occurs almost ideally in response to external deformation. Therefore, it is important to investigate structural changes under more intense deformation conditions in order to understand fracture behavior in highly crosslinked networks [28]. Consequently, further investigation into larger deformations and the fracture behavior of crosslinked phenolic resins using MD simulation and void analysis will be performed and reported in due course [29,30].

References

1. J. H. de Boer, *Trans. Faraday Soc.*, 1936, **32**, 10–37.
2. R. Houwink, *Trans. Faraday Soc.*, 1936, **32**, 122–131.
3. E. H. Erath, and R. A. Spurr, *J. Polym. Sci.*, 1959, **35**, 391–399.
4. J. Mijović, and J. A. Koutsky, *Polymer*, 1979, **20**, 1095–1107.
5. B. E. Nelson, and D. T. Turner, *J. Polym. Sci.*, 1973, **11**, 1949–1961.
6. Y. Shudo, A. Izumi, K. Hagita, T. Nakao, and M. Shibayama, *Polymer*, 2016, **103**, 261–276.
7. J. Wang, R. M. Wolf, J. W. Caldwell, P. A. Kollman, and D. A. Case, *J. Comput. Chem.*, 2004, **25**, 1157–1174.
8. C. I. Bayly, P. Cieplak, W. D. Cornell, and P. A. Kollman, *J. Phys. Chem.*, 1993, **97**, 10269–10280.
9. http://lammps.sandia.gov/
10. S. Nosé, *J. Chem. Phys.*, 1984, **81**, 511–519.

11. W. G. Hoover, *Phys. Rev. A.*, 1985, **31**, 1695–1697.

12. M. Parrinello, and A. Rahman, *J. Appl. Phys.*, 1981, **52**, 7182–7190.

13. R. W. Hockney, and J. W. Eastwood, *Computer Simulation Using Particles*, Adam Hilger: New York, 1989.

14. M. Haughney, M. Ferrario, and I. R. McDonald, *J. Phys. Chem.*, 1987, **91**, 4934–4940.

15. C. Li, and A. Strachan, *J. Polym. Sci. Part B Polym. Phys.*, 2015, **53**, 103–122.

16. T. W. Sirk, K. S. Khare, M. Karim, J. L. Lenhart, J. W. Andzelm, G. B. Mckenna, and R. Khare, *Polymer*, 2013, **54**, 7048–7057.

17. A. P. Thompson, S. J. Plimpton, and W. Mattson, *J. Chem. Phys.*, 2009, **131**, 154107.

18. T. W. Sirk, S. Moore, and E. F. Brown, *J. Chem. Phys.*, 2013, **138**, 064505.

19. K. Sagarik, and P. Asawakun, *Chem. Phys.*, 1997, **219**, 173–191.

20. A. Izumi, T. Nakao, and M. Shibayama, *Soft Matter*, 2012, **8**, 5283–5292.

21. J. -P. Pascault, H. Sautereau, J. Verdu, and R. J. J. Williams, *Thermosetting Polymers*, Marcel Dekker: New York, 2002.

22. J. D. Monk, J. B. Haskins, C. W. Bauschlicher, and J. W. Lawson, *Polymer*, 2015, **62**, 39–49.

23. J. D. Monk, E. W. Bucholz, T. Boghozian, S. Deshpande, J. Schieber, C. W. Bauschlicher, and J. W. Lawson, *Macromolecules*, 2015, **48**, 7670–7680.

24. N. J. L. Megson, *J. Soc. Chem. Ind.*, 1948, **67**, 155–160.

25. X. Zhang, and D. H. Solomon, *Polymer*, 1998, **39**, 405–412.

26. K. Hirano, and M. Asami, *React. Funct. Polym.*, 2013, **73**, 256–269.

27. B. Ottenbourgs, P. Adriaensens, R. Carleer, D. Vanderzande, and J. Gelan, *Polymer*, 1998, **39**, 5293–5300.

28. C. W. Bauschlicher Jr., J. D. Monk, and J. W. Lawson, *Polymer*, 2015, **80** 265–274.

29. S. Yang, and J. Qu, *Phys. Rev. E*, 2014, **90**, 012601.

30. K. Hagita, H. Morita, and H. Takano, *Polymer*, 2016, **99**, 368–375.

Chapter 7

Diffusion Behavior of Methanol Molecules Confined in Crosslinked Phenolic Resins Studied using Neutron Scattering and Molecular Dynamics Simulation

7.1 Introduction

For automotive parts and semiconductor packages, high solvent resistance is required because such materials may be exposed to various solvents under prolonged conditions of high temperature and pressure [1–3]. Solvent penetration into cured thermosetting resins causes many problems, including dimensional changes, decreases in mechanical strength and modulus (leading to solvent stress cracking), and short-circuiting. In designing thermosetting materials, it is necessary to understand the relationships between a crosslinked structure and solvent resistance. Elucidation of the diffusion mechanism of small molecules, such as water, methanol, or ethanol, in cured resins is of special importance for achieving high solvent resistance.

The diffusion coefficient (D) of the penetrating solvent molecule is considered an important parameter for characterizing solvent resistance. In general, measurements of weight change for a piece of test material are often used to estimate the diffusion coefficient [3]. Kaplan et al. investigated the solvent penetration behavior in cured epoxy resins to elucidate the influence of various penetrant solvents, crosslinking agents, and temperature [4]. They assumed a simple Fickian diffusion model for solvent transport. The differential equation of Fick's second law in the one-dimensional case was given for weight change as a function of D and time. D was estimated by the weight change curve. Soles et al. investigated the effect of nanovoid size, molecular flexibility, and temperature on the moisture diffusion coefficient for typical epoxy resins using similar diffusion measurements together with positron annihilation lifetime spectroscopy (PALS) [5].They proposed a molecular mechanism for moisture transport in epoxy resins from the transport kinetics, in which water molecules in the cured epoxy network form hydrogen bonds with the polar group of the epoxy resins (hydroxyl or amine groups) and diffuse in the nanovoid space. Here, the dominant factor for the moisture diffusion

coefficient was the lifetime of hydrogen bonding, not the size or shape of the nanovoid spaces in the network [6].

One of the problems of adsorption experiments is that it takes several days to several months to obtain a solvent uptake curve. Furthermore, it is necessary to prepare an ideal plate-shaped test piece with a flat and smooth surface. The most critical problem of this method is that it cannot be applied to the case of non-Fickian diffusion behavior. As seen in Kaplan's experiments, no clear equilibrium point may be seen in the weight-change curve, which indicates the presence of irreversible processes.

Quasielastic neutron scattering (QENS) is a powerful technique for investigating the dynamics of molecular diffusion in liquids or the fast relaxation processes in polymer chains [7–9]. QENS is able to detect molecular motion over a time scale of 1 ps–10 ns with a spatial scale of 1–100 Å. This space-time scale corresponds to molecular vibrations, rotations and translations. Accordingly, QENS analysis provides atomistic-order information on the molecular structure and the molecular dynamics. Although the diffusion coefficient (D) of molecules can also be characterized by other methods, like pulse field gradient nuclear magnetic resonance (PFG-NMR) spectroscopy, most methods do not provide information on the atomistic spatial scale [10]. Furthermore, the space-time scale of QENS is almost consistent with that of an atomistic molecular dynamics (MD) simulation. Many studies have proved that combination analysis using QENS and MD simulations is a very powerful technique for providing a basic understanding of molecular motion [11,12].

In incoherent QENS, the scattering intensity originates from the incoherent scattering cross-sections (σ_{inc}). The value of σ_{inc} in hydrogen is 80.27 barn, which is much larger than that of deuterium (2.05 barn). Therefore, for most organic materials, the dynamics of a target component (including hydrogen) can be efficiently detected by deuteration of the other components. There are many incoherent QENS studies on the self-diffusion behavior of bulk liquids and polymers. Bermejo investigated the diffusion behavior of bulk methanol by QENS in detail [13], and the estimated value of D in translational diffusion correlated well with the value measured using other techniques, such as PFG-NMR [14]. The dynamics of small molecules in confined spaces was also investigated by many researchers using QENS. Takahara et al. investigated the dynamics of water, methanol, and ethanol confined in porous silica using QENS and dielectric analyses [15–17]. The constrained dynamics of small molecules confined in zeolites [18],carbon nanotubes [19], and micelles [20] have also been investigated using QENS. These studies reported that the D of small molecules in confined spaces was one order

of magnitude smaller compared with those in the bulk state.

In contrast to these studies, QENS studies on the dynamics of liquids confined in cured thermosetting resins have not been reported so far. One reason for this lack of study is that thermosetting resins contain a large amount of hydrogen atoms and lead to larger incoherent scattering than that of penetrated solvent, as mentioned above. In general, deuteration of most of thermosetting resins is not trivial because of synthetic difficulties and costs. Therefore, QENS has not been applied for cured thermosetting polymers, except by Rosenberg, Jørgensen, and Arai for fracton dimension analysis of cured epoxy resins [21–23]. For phenolic resins, we succeeded in synthesizing highly deuterated novolac resins (dNV) through polycondensation of phenol-d_6 and formaldehyde-d_2 [24]. The results of the ^{1}H-NMR analysis for dNV showed that the degree of deuteration, except for the hydroxyl group, was >98%, and the small-angle neutron scattering (SANS) intensity for the cured resin with hexamethylenetetramine (HMTA) exhibited a much lower incoherent scattering background than that of the non-deuterated phenolic resin. Subsequently, we performed small-angle X-ray scattering (SAXS) and SANS experiments for dNV and cured dNV to investigate the structural inhomogeneities in the crosslinking networks [25]. This complementary analysis indicated the presence of nanovoids in the cured resins. The scattering intensity in the range of 3 to 1600 nm^{-1} was mainly accounted for by the internal fractal interfaces between nanovoids and resins. These results suggested that penetrated solvent molecules existed in the resin nanovoids.

Molecular dynamics (MD) simulations for small molecule diffusion have been reported for many systems, such as for bulk liquids and small molecules in confined spaces. In an MD simulation, D can be estimated by calculating the mean squared displacement of each molecule or the velocity auto-correlation function from the MD trajectories [26,27] Solvent diffusion in cured polymer networks is a subject of interest in MD simulations of thermosetting resins. Yarovsky et al. reported the modeling of cured networks for phosphate modified epoxy resins and crosslinkers and the diffusion of water and oxygen in cured networks [28]. Wu et al. investigated moisture content dependence on the structure and D of water in cured bisphenol-A type epoxy resin [29]. It is well known that, in the simulation of thermosetting resins, the modeling method of the crosslinked structure greatly affects the calculation results [30]. Therefore, the structure used in an MD simulation has to be thoroughly examined beforehand. As described in Chapter 5 and 6, atomistic MD simulations were performed on a phenolic resin model constructed using pseudo-crosslink reactions [31,32] and mechanical property characterizations [33]. The obtained model structure was verified by comparison with

experimental data on the chemical structure and X-ray scattering profiles. We confirmed that a large-scale atomistic MD simulation with optimized reaction parameters was appropriate for representing the crosslinked structure, including the crosslink inhomogeneity observed by SAXS experiments using the solvent swelling technique [34–36]. This model structure can be used as an initial structure to calculate solvent diffusion in a crosslinked phenolic network.

In this chapter, the diffusion dynamics of methanol was investigated confined in highly crosslinked phenolic resins by using QENS and atomistic MD simulations. Methanol was chosen as the penetrating solvent because methanol is empirically known to be a solvent that is easily absorbed in cured phenolic resins. A highly deuterated phenolic resin cured with HMTA was used after immersion in methanol or deuterated methanol for the QENS experiments. The incoherent scattering from the methanol molecules was selectively analyzed by model fitting with a Lorentz function using the difference in incoherent scattering cross-sections of hydrogen and deuterium. The diffusion behavior of methanol was discussed based on the diffusion model in confined space. Atomistic MD simulations were also performed on the methanol-dispersed crosslinked phenolic resin model. The diffusion coefficient calculated from the MD trajectories was compared with the QENS result.

7.2 Method

7.2.1   Materials

For QENS experiments, highly deuterated crosslinked phenolic resins were prepared via two processes: synthesis of deuterated novolac resin (i.e., phenolic resin oligomer) and subsequent crosslink reaction using a curing agent, as shown in Figure 7.1. Phenol-d_6 (98.9 atom% D) and 20 wt% formaldehyde-d_2 (99.8 atom% D) in D_2O were purchased from C/D/N isotopes Inc. Oxalic acid and hexamethylenetetramine (HMTA) were purchased from Wako Pure Chemical Industries and Chang Chun Petrochemical Co., Ltd., respectively. Methanol-d_4 (**CD₃OD**, 99.8 atom% D) and methanol (**CH₃OH**) were purchased from Cambridge Isotope Laboratories, Inc. and Wako Pure Chemical Industries, respectively. All materials were used without further purification. Deuterated novolac-type phenolic resin (**dNV**) was synthesized from phenol-d_6 and 20 wt% formaldehyde-d_2 in D_2O according to previous study [24].
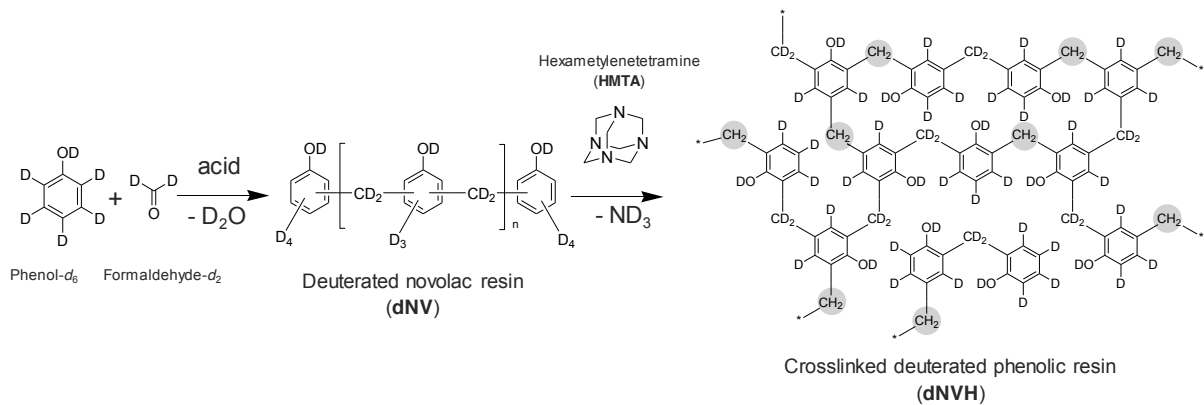
Figure 7.1 Synthesis of highly deuterated phenolic resin (**dNV**) and crosslinked resin (**dNVH**).

7.2.2 Sample Preparation for QENS Experiments

A plate-like test piece of cured phenolic resin (**dNVH**) was prepared from dNV and HMTA as a curing agent by compression molding using a compression molding machine (Shinto Metal Industries Corp., Osaka, Japan). Granulated dNV and HMTA were placed in a molding die and molded at 175 °C for 3 min under an effective pressure of 100 MPa, followed by post-curing at 180 °C for 6 hours and 220 °C for 3 hours under atmospheric pressure. The approximate size of the test pieces was 10 mm × 80 mm with 2 mm thickness. The sample (**dNVH**) and solvent (**CH₃OH** or **CD₃OD**) were sealed in a pressure vessel and allowed to stand for 72 hours in an 80 °C oven. Then, the sample was dried in the air and pulverized with a mill for QENS measurement. The powdered sample was abbreviated as **dNVH–CH₃OH** and **dNVH–CD₃OD**. The dried **dNVH** was also prepared for the comparison. The amount of penetrant methanol in **dNVH–CH₃OH** and **dNVH–CD₃OD** was estimated to be about 8 wt% from the weight change measurement value after heating in a vacuum oven at 120 °C for 1 hour.

From the composition of **dNVH** and methanol in **dNVH–CH₃OH**, the calculated number ratio of H atoms and D atoms is given as H_{dNVH} : D_{dNVH} : H_{CH3OH} = 1 : 5.6: 1.6. Accordingly, the ratio of incoherent scattering cross-sections (σ_{inc}) is given as $\sigma_{inc}(H_{dNVH})$: $\sigma_{inc}(D_{dNVH})$ $\sigma_{inc}(H_{CH3OH})$ = 6.9 : 1: 11.1. This suggests that sufficient incoherent scattering intensity from the **CH₃OH** in the **dNVH–CH₃OH** can be obtained by the QENS measurement for **dNVH–CH₃OH**. However, 42 % in the incoherent scattering intensity in the **dNVH–CH₃OH** originate mainly from the methylene groups in the **dNVH**. In contrast, the incoherent scattering intensity of the methylene groups in **dNVH-CD₃OD** is dominant (96% in the incoherent scattering). Comparing between **dNVH-CH₃OH** and **dNVH-CD₃OD**, the

incoherent scattering from the **CH₃OH** can be extracted.

7.2.3   Quasielastic Neutron Scattering (QENS) Measurements

QENS experiments were performed using the time-of-flight near-backscattering spectrometer (DNA, BL02) installed at the Materials and Life Science Experimental Facility (MLF) of J-PARC, located in Tokai, Ibaraki, Japan [37–39]. Powder samples were lapped with thin aluminum foil (40 mm height, 44 mm width) and were loaded in a cylindrical aluminum sample holder (14.0 mm in inner diameter of the cylinder with 0.25 mm thickness) in a high-purity helium-gas atmosphere. The sample holder was sealed using an indium gasket. The dynamic scattering functions $S(q,\omega)$ were measured at 296 K, in a momentum transfer range $0.1 < q <$ 1.8 Å^{-1} where q is the momentum transfer defined by the neutron wavelength (λ) and the scattering angle (2θ) as $q = (4\pi \sin\theta)/\lambda$. The energy window and resolution were $-40\ \mu$eV $\leq \hbar\omega$ $\leq 100\ \mu$eV and $\Delta E = 3.6\ \mu$eV, respectively. The resolution function was determined using a vanadium standard. The counting time was about 3 hours for QENS. The QENS data reduction and analyses were performed using software provided by the DNA group of J-PARC MLF.

7.2.4   Molecular Dynamics (MD) Simulation

Full atomistic MD simulations were carried out on the methanol-dispersed crosslinked phenolic resin model systems. The crosslinked phenolic resin model structures were generated from phenol molecules via a pseudo-crosslink reaction, as described in our previous research [31]. J-OCTA 1.8 (JSOL Corp, Japan) was used for model construction of phenol and methanol. Partial atomic charges were estimated from RHF/6-31G (d,p) calculation using Gaussian 09 D (Gaussian, Inc., USA) and a restrained electrostatic potential fitting program [40]. The general AMBER Force Field (GAFF) [41] was applied to the potential function for all molecules. LAMMPS (Sandia National Laboratory, USA) [42] was used for the crosslinking reaction and subsequent MD calculation on the K computer (RIKEN Advanced Institute for Computational Science, Japan). A standard velocity Verlet integrator was used with a time step (Δt) of 0.5 fs in the procedures for all calculations. The Nosé–Hoover thermostat [43,44] and Parrinello–Rahman barostat [45] were used to control the temperature and the pressure, respectively, with a damping parameter of 200 fs for the thermostat and 500 fs for the barostat. Lennard-Jones and Coulombic interactions were computed with a cutoff length of 11 Å and a weighting factor

of 0.5 for 1–4 interactions. The Particle–Particle Particle–Mesh solver was used to compute long-range Coulombic interactions with the desired relative error in forces within 10^{-5} accuracy.

The model structure for methanol molecules dispersed in a crosslinked phenolic resin was prepared according to the following procedure: First, crosslinked phenolic resins were constructed from 2,000 phenol molecules and crosslinker atoms using pseudo-reaction algorithms. The details of the crosslinking procedure and features of the resulting structure are described in Chapter 5. The degree of crosslinking for the crosslinked phenolic resin was 0.85. This value is nearly identical to the experimental value estimated by solid-state ^{13}C-NMR spectroscopy for novolac resins cured with HMTA. Thereafter, 594 molecules of methanol were randomly inserted into the equilibrated phenolic network. The weight fraction of methanol in the resulting structure was approximately 8 wt%, which corresponds to the experimental value. 100 ps of MD was performed with the soft repulsive potential implemented in LAMMPS for non-bonding pairwise interactions instead of using a Lennard-Jones potential. This was selected to break up overlapping atoms and unstable atomic configurations between inserted methanol molecules and the resin. This process ensured that methanol molecules were placed in resin cavities, which are relatively stable structures in terms of energy. Finally, the equilibrated structure was obtained after 2 ns of MD with an *NPT* ensemble under atmospheric pressure and given temperature in the range of 220–330 K.

The diffusion coefficient of methanol was estimated from the time dependence of the mean squared displacement (MSD) of methanol molecules using Einstein's relation,

$$D = \frac{1}{6}\frac{d}{dt}\left\{\frac{1}{N}\sum_{i=1}^{N}[\mathbf{r}_i(t) - \mathbf{r}_i(0)]^2\right\} = \frac{1}{6}\frac{d}{dt}\text{MSD}(t), \tag{7.1}$$

where $\mathbf{r}_i(t)$ represents the coordinates of the center-of-mass of the i-th methanol molecule at time t. In this MD study, at first, the diffusion coefficient of methanol in a bulk liquid state was calculated based on this equation. To confirm the validity of the potential parameters, 500 methanol molecules were placed in an isotropic cubic simulation cell with periodic boundaries for each direction, and *NPT* dynamics was performed to equilibrate the cell size and atomic configuration under atmospheric pressure. Subsequently, 1 ns of MD was carried out to calculate the MSD of methanol molecules using an *NVT* ensemble. *D* can be obtained from the MSD–*t* diagram as a gradient. The estimated values of *D* and the density for bulk methanol at 300 K and at atmospheric pressure were 2.3×10^{-5} cm^2/s and 0.81 g/cm^3, respectively, and are well consistent with the experimental values of 2.2–2.4×10^{-5} cm^2/s and 0.79 g/cm^3 [14,46].

7.3 Results and Discussion

7.3.1   QENS Experiment

Figure 7.2 shows the obtained two-dimensional dynamic structure factor $S(q,\omega)$ of **dNVH–CH₃OH** and dried **dNVH**. The **dNVH–CH₃OH** shows both elastic scattering around $\hbar\omega = 0$ (red band) and quasielastic scattering (blue region). Meanwhile, the dried **dNVH** shows much less quasielastic broadening than that of **dNVH–CH₃OH**.
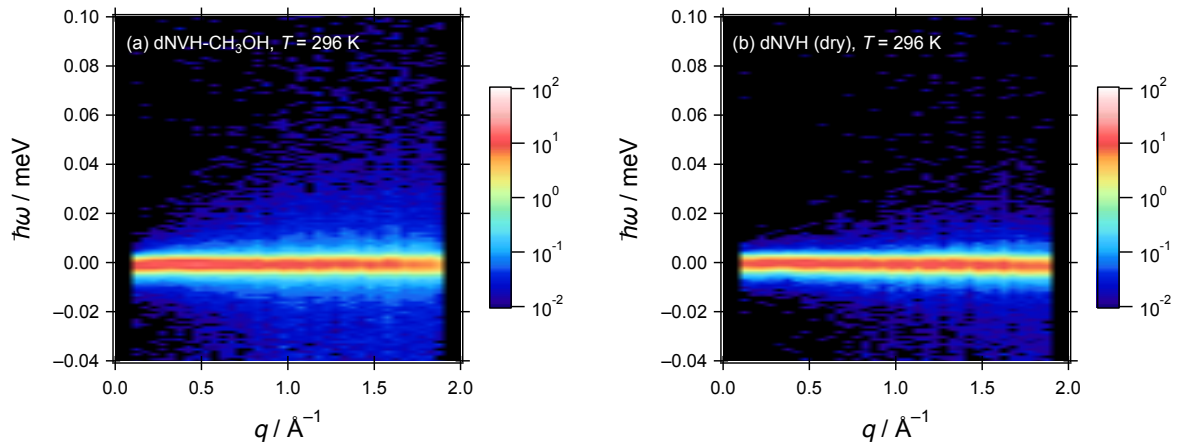

Figure 7.2   Two dimensional-$S(q,\omega)$ of (a) **dNVH–CH₃OH** and (b) dried **dNVH**.

Figure 7.3 shows the QENS profiles of **dNVH–CH₃OH**, **dNVH–CD₃OD**, and dried **dNVH** normalized by the elastic intensity at $q = 1.7$ Å^{-1}. The difference in scattering intensity between **dNVH–CH₃OH** and **dNVH–CD₃OD** indicates the existence of quasielastic broadening from methanol. Furthermore, the larger intensity in **dNVH–CD₃OD** than that of dried **dNVH** in the quasielastic region implies the induction of resin dynamics derived from solvent invasion. Here, this quasielastic scattering is assumed to be from the hydrogen atoms of the crosslinking methylene groups derived from HMTA. As mentioned in our previous study [32], even in highly cured resin, there are independent clusters of small molecules not belonging to a percolated network. The methylene belonging to such a cluster is plasticized by methanol invasion and exhibits motility.
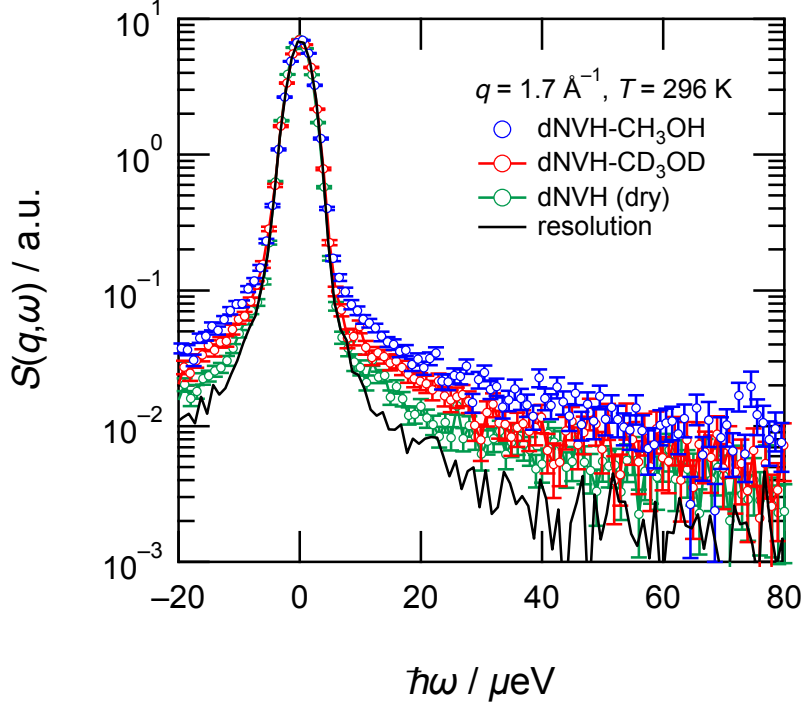
Figure 7.3 Typical QENS spectra for **dNVH–CH₃OH**, **dNVH–CD₃OD** and dried **dNVH** at $q = 1.7$ Å⁻¹. Spectra are normalized by the elastic intensity.

As previously mentioned, the quasielastic scattering profiles of **dNVH–CD₃OD** and **dNVH** in Figure 7.3 suggest the existence of dynamics in the polymer framework induced by solvent invasion. It is reasonable that the QENS profile of **dNVH–CH₃OH** is represented by the sum of methanol and **dNVH** components. Accordingly, Equation (7.2) can be adopted to analyze the scattering profile of **dNVH–CH₃OH** in this chapter.

$$S(q,\omega) = R(q,\omega) \otimes \left[A_{el}^{M}(q)\delta(\omega) + A_{qe}^{M}(q)L(\Gamma^{M},\omega) + A_{el}^{dNVH}(q)\delta(\omega) \right.$$
$$\left. + A_{qe}^{dNVH}(q)L(\Gamma^{dNVH},\omega) \right] + bkg., \tag{7.2}$$

where $R(q,\omega)$, $\delta(\omega)$ and $L(\Gamma,\omega)$ are the resolution function of the DNA spectrometer, the delta function and Lorentz function, respectively, and bkg. denotes the background. A_{el}^{M}, A_{qe}^{M}, A_{el}^{dNVH}, and A_{qe}^{dNVH} denote the coefficients of each scattering component for elastic and quasielastic scatterings of methanol, and elastic scatterings and quasielastic scatterings of **dNVH**, respectively. Γ^{M} and Γ^{dNVH} represent the HWHM in the Lorentz function of methanol and resin, respectively. Parameters of the **dNVH**, A_{el}^{dNVH}, A_{qe}^{dNVH} and Γ^{dNVH} were obtained by the fitting of **dNVH–CD₃OD** as following Equation (7.3):

$$S(q,\omega) = R(q,\omega) \otimes \left[A_{el}^{dNVH}(q)\delta(\omega) + A_{qe}^{dNVH}(q)L(\Gamma^{dNVH},\omega) \right] + bkg., \tag{7.3}$$

because the contribution from the **CD₃OD** was small. The data was well fitted as shown in Figure 7.4(a). The molar fraction of **CH₃OH** in **dNVH–CH₃OH** system is almost the same as that of **CD₃OD** in **dNVH–CD₃OD**. Therefore, Γ^{dNVH}, A_{el}^{dNVH} and A_{qe}^{dNVH} in Equation (7.2) for **dNVH–CH₃OH** are regarded to be the same as those for **dNVH–CD₃OD**. In the subsequent analysis, a parameter fitting was done for A_{el}^{M}, A_{qe}^{M}, Γ^{M} on QENS profile of **dNVH–CH₃OH** using the fixed parameters of A_{el}^{dNVH}, A_{qe}^{dNVH}, Γ^{dNVH} estimated from the fitting result for **dNVH–CH₃OH**. The typical fitting result is shown in Figure 7.4(b). The curve fitting was successful using the above-mentioned model.
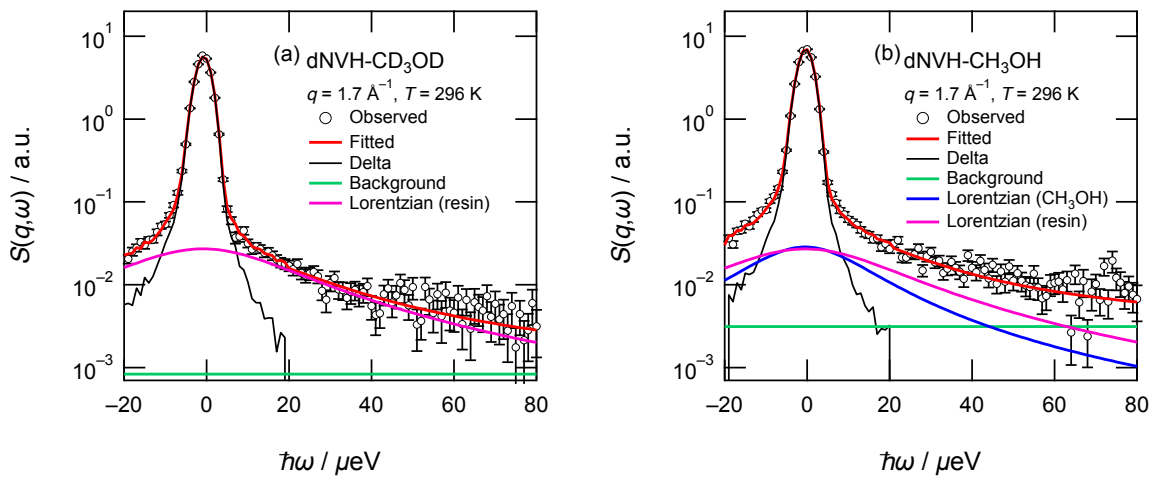
Figure 7.4   QENS spectra of (a) **dNVH–CD₃OD** and (b) **dNVH–CH₃OH** at $q = 1.7$ Å⁻¹.

The q^2-dependence of Γ^{M} is shown in Figure 7.5. The Γ of the bulk methanol is also shown for comparison. In this analysis, the data points of Γ in the range of $q < 0.8$ Å⁻¹ were excluded because the scattering intensity in low-q region likely contains an experimental artifact. The q-dependence of Γ usually reflects diffusion-like molecular motions. In case of continuous diffusion, Γ is expressed as follows;

$$\Gamma(q) = Dq^2, \tag{7.4}$$

where D is the translational diffusion coefficient [7,47]. Random-jump diffusion model shows following relationship;

$$\Gamma(q) = \frac{Dq^2}{1 + \tau_0 Dq^2}, \tag{7.5}$$

where τ_0 is the mean residence time and D is the translational diffusion constant [7]. The q-dependency of the Γ for methanol in cured resin well followed a fitting curve of random-jump

diffusion model, though continuous diffusion did not match in high-q range. The fitting using Equation (7.5) result in $D = 1.6 \times 10^{-6}$ cm^2/s for methanol confined in cured resin, which is one order of magnitude smaller than the value in the bulk, $D = 2.3 \times 10^{-5}$ cm^2/s [13]. From the fitting results of $\tau_0 = 14$ picoseconds and $D = 1.6 \times 10^{-6}$ cm^2/s, mean jump distance $< l > = (6D\tau_0)^{1/2}$ in jump diffusion process can be estimated to be 1.2 Å.
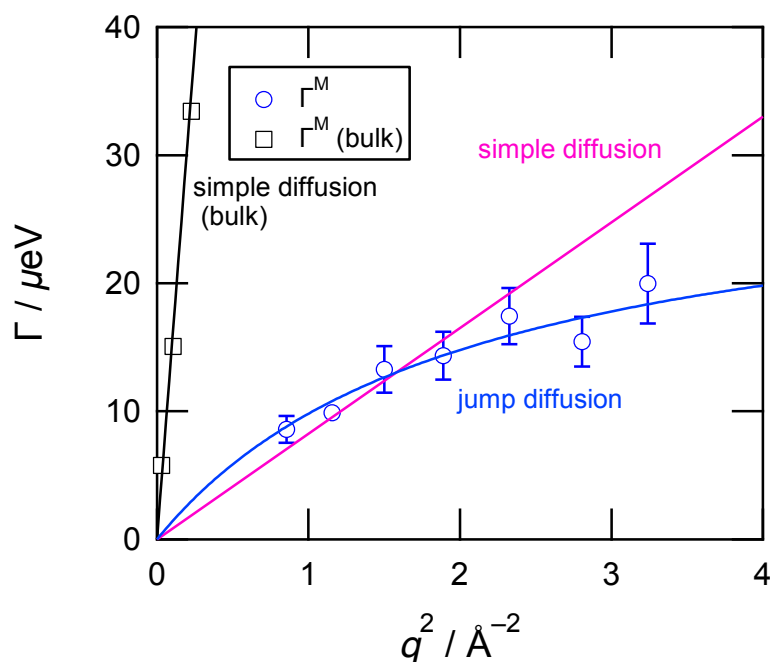
Figure 7.5 q^2-dependence of Γ for bulk **CH₃OH** and Γ^M for **dNVH–CH₃OH** obtained from QENS fitting at $T = 296$ K. Red and blue lines are fitting results by the simple-diffusion and the jump-diffusion models, respectively.

7.3.2 MD simulation

Figure 7.6 shows a 3D image of methanol dispersed in a crosslinked phenolic resin after equilibration at 1 atm and 300 K. The visualization is obtained using the program OVITO [48]. Methanol molecules exist in a vacant space with various sizes. Such a configuration is consistent with the experimental facts of SAXS and SANS, in which voids exist in the network in various sizes ranging from 1 to 1000 nm [25].
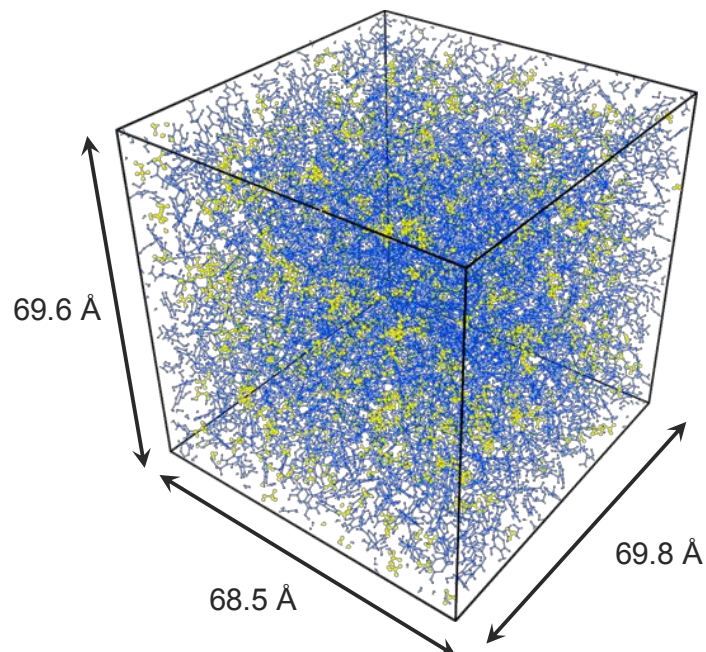
Figure 7.6 3D model of methanol molecules (yellow), confined in cured phenolic resins (blue), used in the MD simulation. The number of methanol is 594 in this simulation box.

The atomistic configuration of methanol was characterized by hydrogen bonds. Figure 7.7 shows the radial distribution functions (RDFs) of the O–O pair between the hydroxyl groups of methanol–methanol, methanol–phenol, and phenol–phenol. The existence of peaks at $r = 2.8$ Å for the $g_{OO}(r)$ of phenol–methanol in Figure 7.7 clearly shows that the hydroxyl groups of methanol molecules in cured resin can form hydrogen bonds to the phenolic network. For phenolic hydroxyl group, the number of hydrogen bonds was calculated and was summarized in Table 7.1 according to the definition by Haughney [49]. This result shows approximately 60 % of methanol molecules form hydrogen bonds to phenolic hydroxyl group. The change in the number of phenolic hydroxyl group forming hydrogen bonds to other phenolic hydroxyl group is small. This implies that penetrant methanol selectively forms hydrogen bonds with the free hydroxyl groups of phenolic units. These results suggest that methanol molecules in the resin network reside in void spaces near hydroxyl groups of phenolic units and form hydrogen bonds to the phenolic hydroxyl group or other methanol molecule.
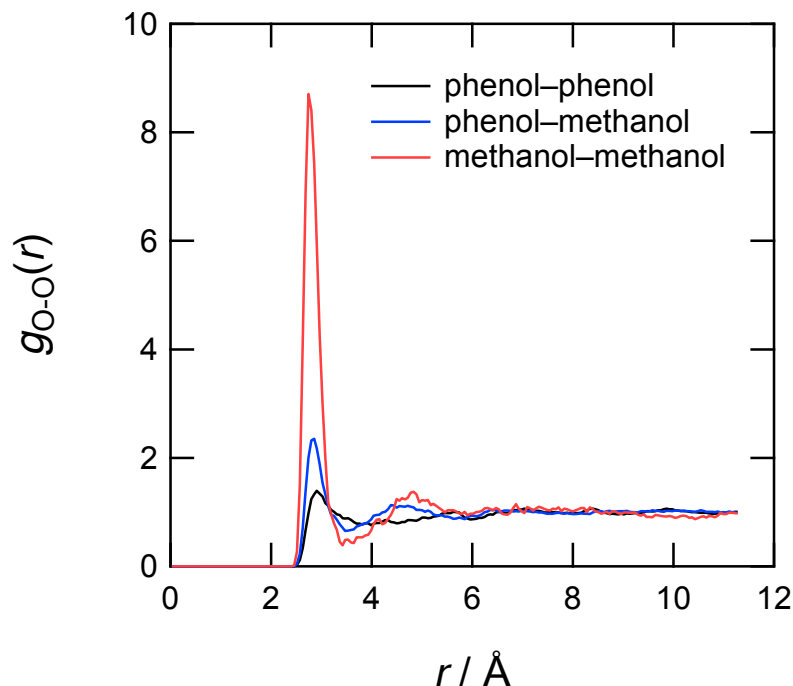
Figure 7.7   Radial distribution function $g(r)$ of oxygen–oxygen in the MD results for the methanol and phenolic resin system.

Table 7.1   The number of free phenolic hydroxyl group and that forming hydrogen bond for before (dried) and after CH_3OH invasion at 300 K.

	dried	after CH_3OH invasion
free	1608	1323
bonded to PhOH	392	332
bonded to CH_3OH	-	345

This can be also explained by the free space of the resin network using Voronoi tessellation [32]. Voronoi analysis was performed for atoms of resin network and the resulted Voronoi volume distribution is shown in Figure 7.8. Here, hydrogen atoms of resins and methanol molecules were excluded for Voronoi tessellation. The strong peaks at the Voronoi volume of 15 $Å^3$ and 20 $Å^3$ in aromatic carbon atom indicate occupying spaces of substituted and unsubstituted carbons on benzene ring, respectively. Carbon atom of methylene linkage and oxygen atom of phenolic hydroxyl group have relatively larger Voronoi volumes compared to aromatic carbon due to smaller topological restriction. The approximate volume of methanol is estimated to be 36.1 $Å^3$ by using the reported kinetic diameter of 4.1 Å [50–52]. Figure 7.8 indicates oxygen atoms with a Voronoi volume larger than this value are present at 33%, while

there are not many carbon atoms. It is concluded that methanol molecules tend to exist in the void space around the hydroxyl group of phenolic resins.
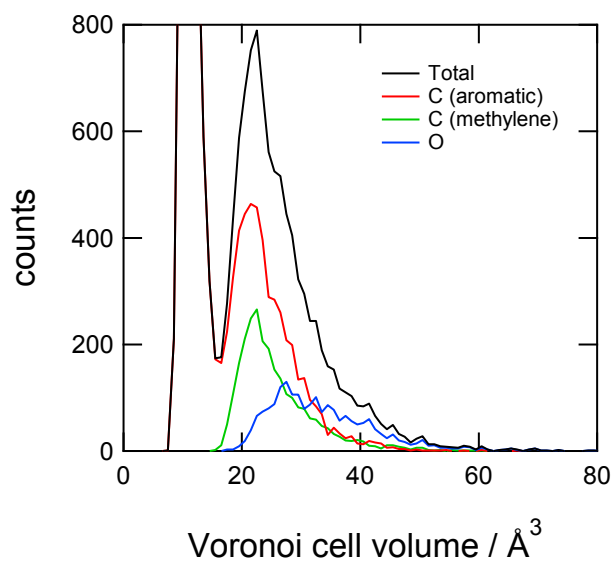

Figure 7.8 Size distribution of Voronoi volume for carbon and oxygen atoms of phenolic network.

To understand the local dynamics of methanol in a network from a real-space view, the MSD of the center-of-mass was calculated for all methanol molecules. The individual MSD of 20 randomly extracted methanol molecules and the averaged MSD curve for all methanol are shown in Figure 7.9. Note that the calculated MSD in Figure 7.9 is the instantaneous value at time t. The average curve in the bulk liquid is also given for comparison. This figure clearly shows that the averaged MSD curve in a network (resins) is lower than that in the bulk. The estimated D is 1.6×10^{-7} cm^2/s for the total average in a network and is smaller than those of the bulk liquid (2.3×10^{-5} cm^2/s) and of the above QENS experiment (1.6×10^{-6} cm^2/s). However, the individual MSD curve categorized into several types of methanol; some molecules move greatly, and others do not move at all. To analyze this heterogeneity, the individual Ds were calculated for all methanol molecules in the system according to Einstein relation:

$$D_i = \frac{1}{6}\frac{d}{dt}[\mathbf{r}_i(t) - \mathbf{r}_i(0)]^2 = \frac{1}{6}\frac{d}{dt}\text{MSD}_i(t), \tag{7.6}$$

where subscript i denotes the i-th molecule. The number average of D_i is the diffusion coefficient originally defined from statistical mechanics. Figure 7.9 shows the logarithm of the

average MSD showed a good linear relationship with the logarithm of time in the range of 50 −1000 ps of time. Taking this into account, we regarded 1/6 of the gradient in this range as the diffusion coefficient D. Similarly, D for individual molecules, D_i, is determined as 1/6 of the slope of individual MSD in this range for the sake of convenience.
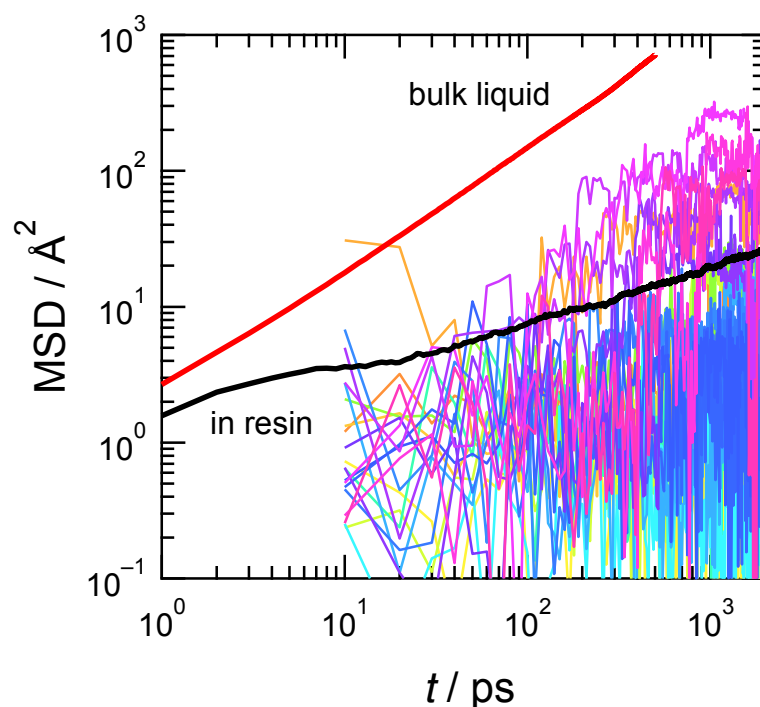

Figure 7.9 The MSD of individual methanol molecules confined in cured phenolic resins (colored lines) and their average (black-bold line) used in the MD simulation. The averaged bulk value is also described for reference (red-bold line).

The distribution of calculated D_i is shown in Figure 7.10. The histogram shows the existence of D over a wide range, showing inhomogeneous diffusivity of methanol in the network. For further analysis, the methanol molecules are roughly classified into diffusive and non-diffusive modes. Here, we regarded diffusive one with larger average diffusion coefficient and non-diffusive smaller one for the fitting results of the D_i distribution with the sum of two Gamma distribution functions. The averaged D and the fraction of diffusive molecules is 1.63 $\times 10^{-6}$ cm^2/s. This result is in good agreement with the QENS experiments, i.e., $D = 1.6 \times 10^{-6}$ cm^2/s. This agreement suggests that our constructed MD model is very reasonable and the existence of confined dynamics for methanol is highly probable. More information about the diffusion behavior of methanol in resin can be also obtained from the time course of the 3D

atomic configuration in the MD simulation. Figure 7.11(a) shows the trajectory lines of randomly chosen 20 methanol molecules in 2 nanoseconds acquired every 10 picoseconds. These molecular trajectories in the MD simulation clearly show that some methanol molecules diffuse by moving a small distance in a limited space, although most methanol molecules are not moving. Such a leaping movement corresponds well to the jump-diffusion model, as suggested from the QENS results. Figure 7.11(b) shows an enlarged snapshot of a methanol molecule surrounded by broken lines in Figure 7.11(a). The jump distance between 140 and 150 ps is longer than that of other steps. It corresponds to a leaping step between the void spaces, that corresponds to an instantaneous rapid increase in MSD as seen in Figure 7.9. It seems that the dynamics of phenolic resins which is induced by methanol invasion as suggested by QENS, also contributes to such jumping motion.
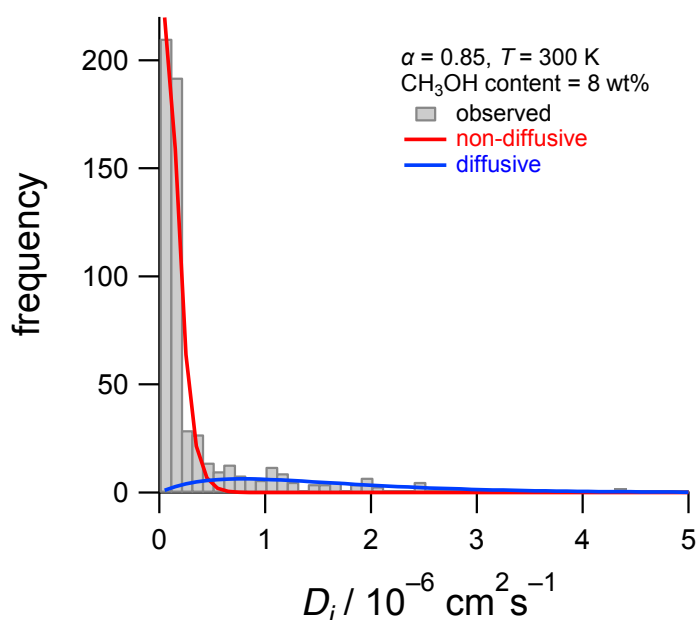
Figure 7.10 Distribution of D for methanol molecules confined in cured phenolic resins in the MD simulation. Two solid lines are fitting curves by Gamma distribution function.
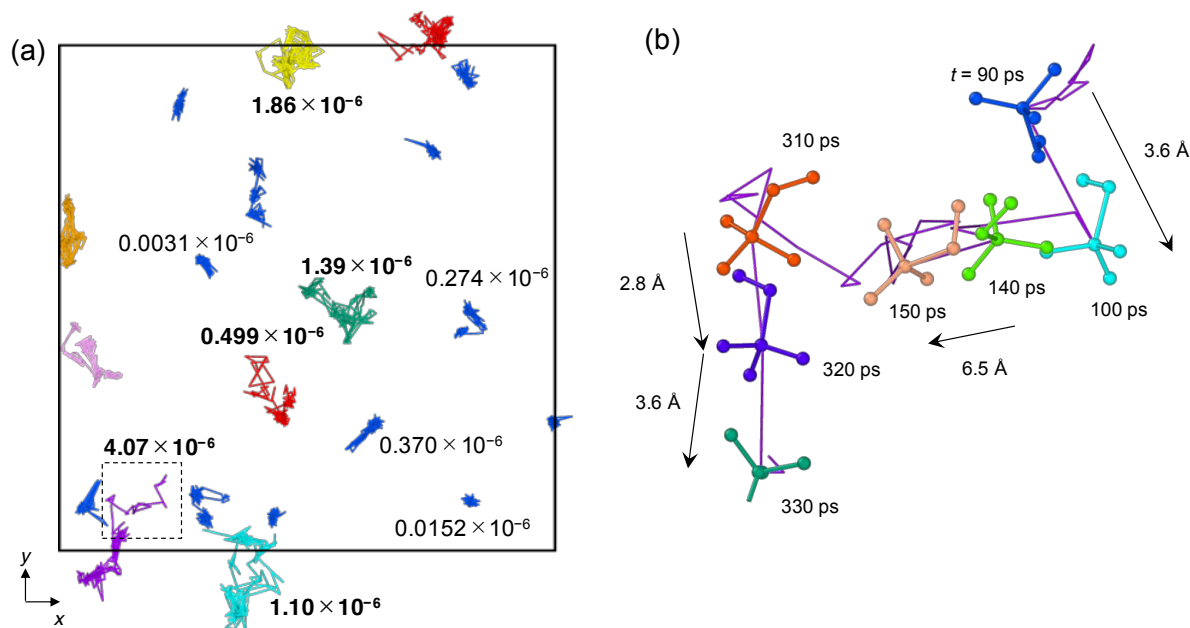
Figure 7.11 (a) Representative trajectory lines of methanol molecules in 2 nanoseconds acquired every 10 picoseconds. The values shown close to the particles indicate D (cm^2/s). Lines of non-diffusive methanol are shown in blue, and diffusive methanol are displayed with different colors. (b) Trajectory of a methanol surrounded by broken lines in (a). Phenolic resin is not displayed to increase visibility for both images.

Figure 7.12 shows the diffusion coefficient of methanol molecules as a function of reciprocal temperature (T^{-1}) in MD simulation. MD results in bulk liquid were also calculated and presented. For both results, it can be seen that the diffusion coefficient follows the Arrhenius equation, $D = D_0 \exp(-E/k_BT)$, as given by a straight line in the figure, where D_0, E, and k_B are the pre-exponential factor, the activation energy, and the Boltzmann constant, respectively. The values of $D_0 = 5.76 \times 10^{-3}$ (cm^2/s) and $E/k_B = 1.64 \times 10^3$ for bulk liquid well agree with experimental values (4.82×10^{-3} and 1.58×10^3)[49,53]. The values for methanol in cured phenolic resins were estimated to be 3.16×10^{-4} and 1.63×10^3, respectively. The agreement of the activation energy suggested that the intermolecular forces on diffusive methanol are equivalent to that on bulk methanol, that is, diffusive methanol forms a hydrogen bond to other methanol or hydroxyl group of phenolic resins. The smaller value of D_0 compared to bulk also indicates the existence of steric hindrance of the resin network acting as interference factor on methanol diffusion.
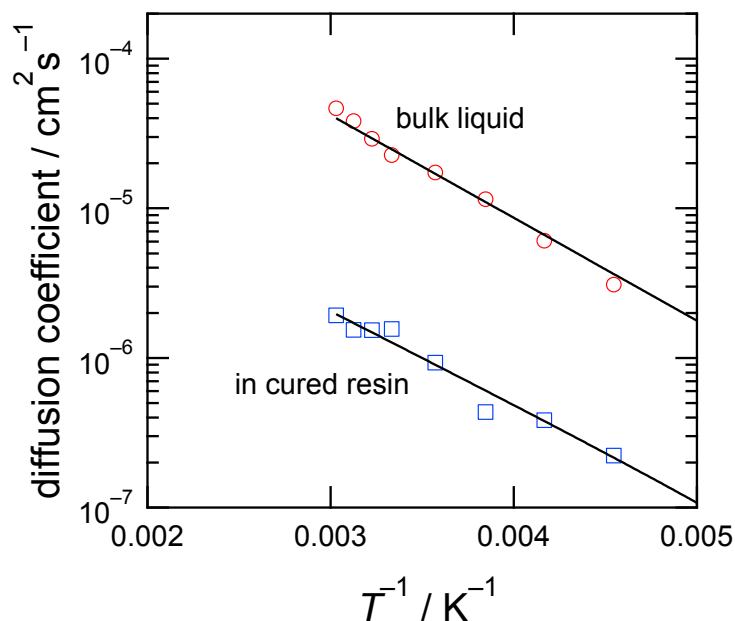
Figure 7.12 Calculated diffusion coefficients of methanol molecules by MD simulation as a function of reciprocal temperature. Solid line represents fitting one by Arrhenius-type equation.

The above-disclosed results suggest the following solvent penetration model: Penetrating methanol molecules stay in the vacant spaces around the hydroxyl groups of phenolic units for some time and then diffuse by jumping to adjacent void spaces. This process then repeats. In the equilibrium structure, methanol molecules in the network are likely to form hydrogen bonds with the hydroxyl group of phenolic units and other methanol molecules. Hydrogen bonding between penetrating molecules and the polymeric network is recognized as an important factor for solvent swelling in other thermosetting polymers, such as the epoxy resin and water system previously mentioned. This situation is identical to our phenolic resin and methanol system. These results suggest that there are several ways for preventing solvent penetration by small molecules having hydroxyl groups, like water and methanol. One of the solutions would be to reduce the free volume and the fraction of hydroxyl groups in the resin network. Specifically, in a phenolic resin system, changing the molecular weight distribution and the *ortho*/*para* linking ratio in the prepolymer stage before gelation is supposed to be effective, as revealed in our previous MD study [32].This investigation also showed that QENS analysis is an effective technique for understanding the diffusion behavior of penetrant molecules confined in crosslinked phenolic resins. To prove the versatility of this method for other polymer/solvent systems, further experimental and computational studies will be required.

7.4 Conclusions

The diffusion behavior of methanol confined in a crosslinked phenolic resin was investigated by QENS experiments and atomistic MD simulations. In the QENS experiment, a deuterated phenolic resin and methanol (both deuterated and non-deuterated) were used to obtain incoherent scattering functions of methanol because difference in incoherent scattering cross-sections for hydrogen and deuterium was shown. The QENS profiles were well represented as a sum of one elastic and two quasielastic components, indicating the presence of resin dynamics induced by methanol invasion and confined diffusion of methanol molecules. The q-dependence of EISF analysis suggested that the diffusive motion of methanol in the spherical confined space of a resin network would look like. The q-dependence of the HWHM on methanol revealed that the diffusion coefficient of methanol was 1.6×10^{-6} cm^2/s, which is one order of magnitude smaller than the value in the bulk, $D = 2.3 \times 10^{-5}$ cm^2/s, indicating confinement by a polymer network. The MD simulation showed that methanol molecules reside in the vicinity of phenolic hydroxyl groups. Additionally, the presence of diffusive and non-diffusive methanol molecules in highly cross-linked phenolic resins was suggested using mean squared displacement analysis for individual methanol molecules. The MD trajectories showed that some methanol molecules diffuse within a limited space in the resin network by jump-diffusion like behavior, as suggested by QENS analysis.

This study showed that QENS and MD simulations play important, complementary roles in understanding the diffusion behavior of invading methanol molecules into cross-linked phenolic resins from an atomistic viewpoint. This study also indicated the direction of the molecular design of thermosetting polymers to prevent solvent penetration of methanol, for example, by reduce hydroxyl groups and free volumes by means of adjusting the functional groups and the molecular weight distribution of prepolymers. We believe these techniques and the findings by this study are applicable to general solvent swelling problems of any thermosetting polymer.

References

1. A. Gardziella, L. A. Pilato, and A. Knop, *Phenolic Resins: Chemistry, Applications, Standardization, Safety and Ecology*, second ed., Springer: Berlin, 2000.
2. *Phenolic Resins: A Century of Progress*, L. Pilato, Ed., Springer: Berlin, 2010.

3. J. -P. Pascault, H. Sautereau, J. Verdu, and R. J. J. Williams, *Thermosetting Polymers*, Marcel Dekker: New York, 2002.

4. M. L. Kaplan, *Polym. Eng. Sci.*, 1991, **31**, 689–698.

5. C. L. Soles, F. T. Chang, D. W. Gidley, and A. F. Yee, *J. Polym. Sci. B: Polym. Phys.*, 2000, **38**, 776–791.

6. C. L. Soles, and A. F. Yee, *J. Polym. Sci. B: Polym. Phys.*, 2000, **38**, 792–802.

7. M. Bée, *Quasielastic Neutron Scattering: Principles and Applications in Solid State Chemistry, Biology and Materials Science*; Adam Hilger: Bristol and Philadelphia, 1988.

8. *Dynamics of Soft Matter: Neutron Applications*; V. García Sakai, C. Alba-Simionesco, and S. -H. Chen, Eds., Springer: Berlin, 2012.

9. V. García Sakai, and A. Arbe, *Curr. Opin. Colloid Interface Sci.*, 2009, **14**, 381–390.

10. H. Mehrer, *Diffusion in Solids*; Springer: Berlin, 2009.

11. L. N. Gergidis, D. N. Theodorou, and H. Jobic, *J. Phys. Chem. B*, 2000, **104**, 5541–5552.

12. J. Colmenero, M. Brodeck, A. Arbe, and D. Richter, *Macromolecules*, 2013, **46**, 1678–1685.

13. F. J. Bermejo, F. Batallán, E. Enciso, R. White, A. J. Dianoux and W. S. Howells, *J. Phys.: Condens. Matter*, 1990, **2**, 1301–1314.

14. N. Karger, T. Vardag, H. D. Lüdemann, N. Karger, T. Vardag, and H. Lodemann, *J. Chem. Phys.*, 1999, **93**, 3437–3444.

15. S. Takahara, M. Nakano, S. Kittaka, Y. Kuroda, T. Mori, H. Hamano, and T. Yamaguchi, *J. Phys. Chem. B*, 1999, **103**, 5814–5819.

16. S. Takahara, N. Sumiyama, S. Kittaka, T. Yamaguchi, M. -C. Bellissent Funel, *J. Phys. Chem. B*, 2005, **109**, 11231–11239.

17. S. Takahara, S. Kittaka, T. Mori, Y. Kuroda, T. Takamuku, and T. Yamaguchi, *J. Phys. Chem. C* **2008**, *112* (37), 14385–14393.

18. N. M. Gupta, D. Kumar, V. S. Kamble, S. Mitra. R. Mukhopadhyay, and V. B. Kartha, *J. Phys. Chem. B*, 2006, **110**, 4815–4823.

19. E. Mamontov, C. J. Burnham, S. -H. Chen, A. P. Moravsky, C. -K. Loong, N. R. de Souza, and A. I. Kolesnikov, *J. Chem. Phys.*, 2006, **124**, 194703.

20. M. R. Harpham, B. M. Ladanyi, N. E. Levinger, and K. W. Herwig, *J. Chem. Phys.*, 2004, **121**, 7855.

21. H. M. Rosenberg, *Phys. Rev. Lett.*, 1985, **54**, 704–706.

22. A. J. Dianoux, J. N. Page, and H. M. Rosenberg, *Phys. Rev. Lett.*, 1987, **58**, 886–888.

23. M. Arai, and J. -E. Jørgensen, *Phys. Lett. A*, 1988, **133**, 70–74.

24. A. Izumi, T. Nakao, and M. Shibayama, *J. Polym. Sci. Part A Polym. Chem.*, 2011, **49**, 4941–4947.

25. A. Izumi, T. Nakao, H. Iwase, and M. Shibayama, *Soft Matter*, 2012, **8**, 8438–8445.

26. M. P. Allen, and D. J. Tildesley, D. J. *Computer Simulation of Liquids*; Clarendon Press: New York, 1989.

27. *Computer Simulation of Polymeric Materials: Applications of the OCTA System*; Japan Association for Chemical Innovation, Ed.; Springer: Berlin, 2016.

28. I. Yarovsky, and E. Evans, *Polymer*, 2002, **43**, 963–969.

29. C. Wu, and W. Xu, *Polymer*, 2007, **48**, 5440–5448.

30. C. Li, and A. Strachan, *J. Polym. Sci. Part B Polym. Phys.*, 2014, **53**, 103–122.

31. A. Izumi, T. Nakao, and M. Shibayama, *Soft Matter*, 2012, **8**, 5283–5292.

32. Y. Shudo, A. Izumi, K. Hagita, T. Nakao, and M. Shibayama, *Polymer*, 2016, **103**, 261–276.

33. Y. Shudo, A. Izumi, K. Hagita, T. Nakao, and M. Shibayama, *Polymer*, 2017, **116**, 506–514.

34. A. Izumi, T. Nakao, and M. Shibayama, *Soft Matter*, 2013, **9**, 4188–4197.

35. A. Izumi, T. Nakao, and M. Shibayama, *Polymer*, 2015, **59**, 226–233.

36. A. Izumi, Y. Shudo, T. Nakao, and M. Shibayama, *Polymer*, 2016, **103**, 152–162.

37. K. Shibata, N. Takahashi, Y. Kawakita, M. Matsuura, T. Yamada, T. Tominaga, W. Kambara, M. Kobayashi, Y. Inamura, T. Nakatani, K. Nakajima, and M. Arai, *JPS Conf. Proc.*, 2015, **8**, 036022.

38. H. Seto, S. Itoh, T. Yokoo, H. Endo, K. Nakajima, K. Shibata, R. Kajimoto, S. Ohira-Kawamura, M. Nakamura, Y. Kawakita, H. Nakagawa, and T. Yamada, *Biochim. Biophys. Acta - General Subjects*, 2017, **1861**, 3651–3660.

39. K. Nakajima, Y. Kawakita, S. Itoh, J. Abe, K. Aizawa, H. Aoki, H. Endo, M. Fujita, K. Funakoshi, W. Gong, M. Harada, S. Harjo, T. Hattori, M. Hino, T. Honda, A. Hoshikawa, K. Ikeda, T. Ino, T. Ishigaki, Y. Ishikawa, H. Iwase, T. Kai, R. Kajimoto, T. Kamiyama, N. Kaneko, D. Kawana, S. Ohira-Kawamura, T. Kawasaki, A. Kimura, R. Kiyanagi, K. Kojima, K. Kusaka, S. Lee, S. Machida, T. Masuda, K. Mishima, K. Mitamura, M. Nakamura, S. Nakamura, A. Nakao, T. Oda, T. Ohhara, K. Ohishi, H. Ohshita, K. Oikawa, T. Otomo, A. Sano-Furukawa, K. Shibata, T. Shinohara, K. Soyama, J. Suzuki, K. Suzuya, A. Takahara, S. Takata, M. Takeda, Y. Toh, S. Torii, N. Torikai, N. L. Yamada,

T. Yamada, D. Yamazaki, T. Yokoo, M. Yonemura, and H. Yoshizawa, *Quantum Beam Sci.*, 2017, **1**, 9.

40. C. I. Bayly, P. Cieplak, W. D. Cornell, and P. A. Kollman, *J. Phys. Chem.*, 1993, **97**, 10269–10280.

41. J. Wang, R. M. Wolf, J. W. Caldwell, P. A. Kollman, and D. A. Case, *J. Comput. Chem.*, 2004, **25**, 1157–1174.

42. http://lammps.sandia.gov/

43. S. Nosé, *J. Chem. Phys.*, 1984, **81**, 511–519.

44. W. G. Hoover, *Phys. Rev. A*, 1985, **31**, 1695–1697.

45. M. Parrinello, and A. Rahman, *J. Appl. Phys.*, 1981, **52**, 7182–7190.

46. M. Frenkel, X. Hong, R. C. Wilhoit, and K. R. Hall, In *Thermodynamic Properties of Organic Compounds and their Mixtures: the Densities of Alcohols (Landolt–Börnstein - Group IV Physical Chemistry)*, K. R. Hall, and K. N. Marsh, Eds., Springer: Berlin, Vol. 8G, pp. 11–301, 2000.

47. P. A. Egelstaff, *An Introduction to the Liquid State*; Academic: London, 1967.

48. A. Stukowski, *Modelling Simul. Mater. Sci. Eng.*, 2010, **18**, 015012.

49. M. Haughney, M. Ferrario, and I. R. McDonald, *J. Phys. Chem.*, 1987, **91**, 4937–4940.

50. B. van der Bruggen, J. Schaep, D. Wilms, and C. Vandecasteele, *J. Membr. Sci.*, 1999, **156**, 24–41.

51. D. Shah, K. Kissick, A. Ghorpade, R. Hannah, and D. Bhattacharyya, *J. Membr. Sci.*, 2000, **179**, 185–205.

52. J. E. ten Elshof, C. R. Abadal, J. Sekulić, S. R. Chowdhury, and D. H. A. Blank, *Micropor. Mesopor. Mater.*, 2003, **65**, 197–208.

53. R. L. Hurle, and A. W. Lawrence, *Aust. J. Chem.* 1980, **33**, 1947–1952.

Summary

In this study, structure analyses using scattering analysis and atomistic MD simulation were performed to understand the structure–property relationships in crosslinked phenolic resins from an atomistic perspective. The author has focused on observing structural inhomogeneity during the curing process of novolac-type phenolic resin using HMTA, as well as the construction and characterization of cured structure of phenolic resins by MD simulation. The details of the respective chapters are summarized as follows.

In Chapter 2, the basic equations required to understand the structure and dynamics of matter through scattering experiments were derived. The static and dynamic structure factors, which include information about the structure and the dynamics and are obtained from elastic and inelastic scattering experiments, can be obtained by Fourier transformation of a probability density function in time and space. These equations indicate that atomistic trajectories obtained from atomistic MD simulation can reproduce the static and dynamic structure factors. In other words, the MD simulation results can be compared and verified via scattering profiles.

In Chapter 3, the behavior of the novolac resin was investigated using DLS cured with different amounts of HMTA in a pre-gel regime for the curing reaction. The plot of the hydrodynamic radius of novolac resin in THF as a function of weight-average molecular weight indicated two different growth mechanisms during curing with HMTA in the pre-gel regime irrespective of the amount of HMTA. An initial power-law relationship (scaling exponent: 0.94) and a subsequent large deviation from this relationship were observed. As the gel point was reached, intermolecular reactions between larger molecules became dominant due to crosslinking via methylene linkages, which occurred after decomposition of the initially formed HMTA decomposition products. These results suggest that the structural differences governing the mechanical properties of phenolic resins are established in the pre-gel stage followed by noticeable differences in the mechanical properties during the subsequent curing process.

In Chapter 4, the crosslink inhomogeneity of phenolic resins at the initial stage of the curing process (110–130 °C) was investigated through structural analyzes of the network

127

structure evolution using ^{1}H-pulse NMR spectroscopy and complementary SAXS/WAXS and SANS/WANS with a solvent-swelling technique. ^{1}H-pulse NMR analysis revealed that three structures in the swollen gel, i.e., the high-crosslink-density domain, the interface region between the high- and low-crosslink-density domains, and the low-crosslink-density domain, are characterized by three different proton nuclear spin−spin relaxation behaviors with T_2. Complementary SAXS/WAXS and SANS/WANS results clearly indicated the characteristic behavior that curing of novolac with HMTA proceeds with a decrease in $\varXi$ while ξ remains constant, and that the change in the value of $\varXi$ starts from essentially the same value at 110 °C, irrespective of the novolac/HMTA ratio. The intradomain reactions in the high- and low-crosslink-degree domains were dominant at the initial stages of the curing process, which resulted in no significant change in the spatial location and size of these domains during the investigated initial curing temperature range. In addition, minor intradomain reaction at the interface of the high-crosslink-density domains occurred, which could be observed as a significant reduction in the size of the low-crosslink-density domain in the solvent swollen state.

In Chapter 5, the network structure of crosslinked phenolic resins was constructed via large-scale atomistic MD simulation using a pseudo-reaction model. The crosslinked structural model obtained using phenol for the initial molecules exhibited good agreement with the experimental results in terms of the branching structure of the phenolic units, methylene linkages, molecular weight distributions, densities, and scattering functions. The structure factor $S(q)$ calculated for the phenolic resins indicated the existence of inhomogeneous crosslinking that expanded as the reaction proceeded after gelation, which agrees with the inhomogeneous reaction mechanism deduced from SAXS experiments. The experimental molecular weight distribution before gelation and the scattering function were well reproduced by a large-scale simulation with 232,000 atoms. The reaction method discussed in this chapter demonstrates reactivity control on the *ortho* and *para* positions in phenolic resins. This study also demonstrated the importance of the initial molecular configuration, i.e., a network structure constructed from monodisperse novolac oligomers showed lower density than that constructed from monomeric phenol due to structural constraints, which was verified by the change in the occupation volume of the phenolic units for a crosslinking reaction through Voronoi tessellation analysis. These results indicate that the structure and properties of crosslinked phenolic resins can be controlled by molecular topology in consideration of crosslinking conversion, branching structure, methylene linkages, and molecular weight distribution.

In Chapter 6, structure–mechanical property relationships in highly crosslinked phenolic resins were investigated by atomistic MD simulation using uniaxial tensile deformation for the structures with different conversions and numbers of hydrogen bonds. Stress–strain curves and changes in chemical structure during deformation suggested that the elasticity of the phenolic network is primarily derived from bonding energy potential involving the orientation of chemical bonds toward the deformation axis rather than bond stretching or hydrogen bonds that have been believed to assume an important role in elasticity. A spatial distribution analysis of the tensile stress and crosslink density indicated no stress concentration in the linear elastic region. These MD results provide information about how we can design highly elastic thermosetting resins, indicating that it is essential to improve crosslink conversion and crosslink density. For phenolic resins, as identified in Chapter 5, further increase in tensile modulus may be achieved by reducing the number of hydrogen bonds or by adjusting the molecular weight distribution for novolac resins prior to gelation.

In Chapter 7, the diffusion behavior of methanol confined in a crosslinked phenolic resin was investigated through QENS experiments and atomistic MD simulations. In the QENS experiment, a deuterated phenolic resin and methanol (both deuterated and non-deuterated) were used to selectively obtain the incoherent scattering functions of methanol. The q-dependence of the HWHM on methanol suggested that the methanol in a cured resin network diffused according to the jump-diffusion model with a diffusion coefficient of 1.6×10^{-6} cm^2/s, which was one order of magnitude less than the value in the bulk ($D = 2.3 \times 10^{-5}$ cm^2/s), thereby indicating confinement by a polymer network. The MD simulation showed that methanol molecules reside in the vicinity of phenolic hydroxyl groups, and the presence of diffusive and non-diffusive methanol molecules in highly crosslinked phenolic resins was identified using mean squared displacement analysis for individual methanol molecules. In addition, the MD trajectories of the diffusive methanol molecules within a limited space formed by the resin network showed behavior that is quite similar to jump-diffusion, as suggested by QENS analysis.

In conclusion, we have successfully demonstrated structural analysis of crosslink inhomogeneity in the curing process of phenolic resins by scattering analyzes and the effectiveness of MD simulations to construct and to characterize the crosslinked network of

phenolic resins. These studies have shown that both scattering analysis and MD simulations play important, complementary roles in understanding the structure and dynamics of crosslinked phenolic resins from an atomistic perspective. We would like to emphasize that the methodology presented in this dissertation is not limited to phenolic resins. It is also applicable to general thermosetting polymers. We believe that this study will present a foundation approach to solve many thermosetting resin problems.

List of Publications

1. <u>Yasuyuki Shudo</u>, Atsushi Izumi, Takeshi Takeuchi, Toshio Nakao, and M. Shibayama, "Dynamic light scattering study of the curing mechanisms of novolac-type phenolic resins", *Polym. J.*, 2015, **47**, 428–433.
   DOI: 10.1038/pj.2015.15 (**Chapter 3**)

2. Atsushi Izumi, <u>Yasuyuki Shudo</u>, Toshio Nakao, and Mitsuhiro Shibayama, "Crosslink inhomogeneity in phenolic resins at the initial stage of curing studied by ^{1}H-pulse NMR spectroscopy and complementary SAXS/WAXS and SANS/WANS with a solvent-swelling technique", *Polymer*, 2016, **103**, 152–162.
   DOI: 10.1016/j.polymer.2016.09.067 (**Chapter 4**)

3. <u>Yasuyuki Shudo</u>, Atsushi Izumi, Katsumi Hagita, Toshio Nakao, and Mitsuhiro Shibayama, "Large-scale molecular dynamics simulation of crosslinked phenolic resins using pseudo-reaction model", *Polymer*, 2016, **103**, 261–276.
   DOI: 10.1016/j.polymer.2016.09.069 (**Chapter 5**)

4. Atsushi Izumi, <u>Yasuyuki Shudo</u>, Katsumi Hagita, and Mitsuhiro Shibayama, "Molecular dynamics simulations of crosslinked phenolic resins using a united-atom model", *Macromol. Theory Simul.*, 2018, 1700103-1–8.
   DOI: 10.1002/mats.201700103 (**Chapter 5**)

5. <u>Yasuyuki Shudo</u>, Atsushi Izumi, Katsumi Hagita, Toshio Nakao, and Mitsuhiro Shibayama, "Structure-mechanical property relationships in crosslinked phenolic resin investigated by molecular dynamics simulation", *Polymer*, 2017, **116**, 506–514.
   DOI: 10.1016/j.polymer.2017.02.037 (**Chapter 6**)

6. <u>Yasuyuki Shudo</u>, Atsushi Izumi, Katsumi Hagita, Takeshi Yamada, Kaoru Shibata, and Mitsuhiro Shibayama, "Diffusion behavior of methanol molecules confined in crosslinked phenolic resins studied using neutron scattering and molecular dynamics simulation", *submitted*.
   (**Chapter 7**)

Acknowledgement